Transverse Laser Cooling of SrF

Aki Matsushima

Thesis submitted in partial fulfilment of the requirements
for the degree of Doctor of Philosophy.

Department of Physics

Imperial College London
October 2013

Declaration

I declare that this thesis is my own work. Where I have used the work of others the sources are appropriately referenced and acknowledged.

Abstract

This thesis discusses an experiment, which has demonstrated transverse laser cooling of a pulsed supersonic beam of strontium monofluoride (SrF) molecules. Producing ultracold molecules is important because they could advance many fields including many-body physics, quantum chemistry and precision measurements to explore fundamental forces in nature. Direct laser cooling of molecules is a new and promising way to produce molecules with temperatures in the sub-millikelvin range.

In the experiment, SrF molecules produced from a pulsed supersonic source were cooled in the transverse direction using light from just two lasers. The molecular beam brightness was increased by about 20%. I discuss the detailed experimental setup, laser system and data analysis. I also present several theoretical models, which give insight into the cooling experiment. Finally, I discuss improvements to this experiment, which should enable higher yields of ultracold molecules to be produced.

Acknowledgements

I would like to thank my supervisors Ben Sauer and Jony Hudson, and the other members of staff working on the experiment Mike Tarbutt and Ed Hinds, for their guidance. I feel very privileged to have had the opportunity to work with them and I really enjoyed it. I would also like to thank my post-docs and fellow PhD students on my experiment Anne Cournol, Thom Wall and Valentina Zhelyazkova for being wonderful to work with and learn from. Thank you too to the students of the YbF electron EDM experiment Joe Smallman and Jack Devlin for their help.

I am also grateful towards the rest of the research group for their help and company.

Thanks to Jon Dyne and Steve Maine for their technical work, and Sanja Maricic for her administrative support.

Thanks to my friends and family for their support, especially Lisa and my mum.

Contents

List of Figures

List of Tables

Chapter 1

Introduction

This thesis describes a new experiment for laser cooling SrF at the Centre for Cold Matter in Imperial College London.

I contributed to most of the construction of the apparatus, running the experiment and data analysis. I assembled the vacuum chamber (section 3.2) and the supersonic source (section 3.3) including the valve driver. I set up all of the laser systems (section 3.3 and 3.4) and electro-optic modulators (EOMs) (section 3.4.1) except for the feedback system to stabilize the HeNe reference laser (section 3.7). I designed and assembled the detection optics (section 3.6) and magnetic field coils (section 3.5). I set up and configured the computer hardware (section 3.9) to use with exisiting software. I used the rate equation model (section 4.1) and wrote the analytic model (section 4.2.1) and numerical model (section 4.2.2) to calculate suitable experimental parameters. I conducted all experiments and associated analysis (chapters 3 and 5), and made the improvements to the apparatus (section 5.10).

The technique of laser cooling molecules is currently attracting interest as a way to produce molecules in the microkelvin range. Many-body physics, quantum chemistry and precision measurements to explore fundamental forces in nature [1] would all stand to benefit. Many methods to produce cold molecules (between 1 mK to 1 K) are being developed including electric and magnetic decelerators, magnetic association, photoassociation and buffer gas cooling. However, laser cooling is one of the very few ways to access the ultracold regime ($<$1 mK).

This chapter outlines what ultracold molecules can offer and gives an overview of other methods of producing cold- and ultracold molecules. I will emphasize the

significance of the technique of laser cooling molecules as a way to bridge the gap between a few kelvin, which is currently easily accessible, to the sub-milikelvin range. It will be shown that ultracold molecules opens up the way to new physics, and that laser cooling is a method to produce these ultracold molecules with very few viable alternatives.

1.1 Applications of Cold and Ultracold Polar Molecules

1.1.1 Quantum Information Processing

Cold molecules are good candidates for qubits in quantum computing as they have have high sample purity, offer long interaction times and can be trapped by off-resonant AC fields. Furthermore, molecular electric dipole moments can be induced and manipulated using electric fields, and molecules have strong dipole-dipole interactions that give rise to faster processing speeds and that can be used to couple the internal states of molecules.

DeMille has proposed a cold molecule-based quantum computer using only known experimental techniques [2]. The architecture is essentially a 1D array of trapped cold polar KCs molecules in an optical trap of depth $100\,\mu$K. The array is subject to an external E-field that varies along the trap, as shown in figure 1.1.

Each molecule represents a qubit. The molecule's electric dipole moment can be aligned ($|0\rangle$) or anti-aligned ($|1\rangle$) with the external field, giving the two states of the qubit. The external E-field shifts the qubit energy levels by the Stark effect $-\vec{\mu_{\mathrm{E}}} \cdot \vec{E}$, where μ_{E} is the electric dipole moment of the molecule and $\vec{E}$ is the total electric field that it experiences. Each qubit has states that are shifted by a different amount, since the electric field strength is different for each site in the array. Each qubit can be addressed individually by electric resonance with microwaves of a frequency unique to the qubit. Arbitrary superpositions of $|0\rangle$ and $|1\rangle$ can be prepared in this way. A smaller Stark shift is induced in a qubit by the E-field due to the electric dipole moment of neighbouring qubits, which are of course polar molecules. For this to work, the molecules need to be cold enough so that their thermal energy is lower than the dipole-dipole interaction. The coupling between qubits distinguishes transitions between two-qubit states such as $|00\rangle \leftrightarrow |01\rangle$ and $|10\rangle \leftrightarrow |11\rangle$ as illustrated in figure 1.2. In this way, single-qubit and CNOT gates

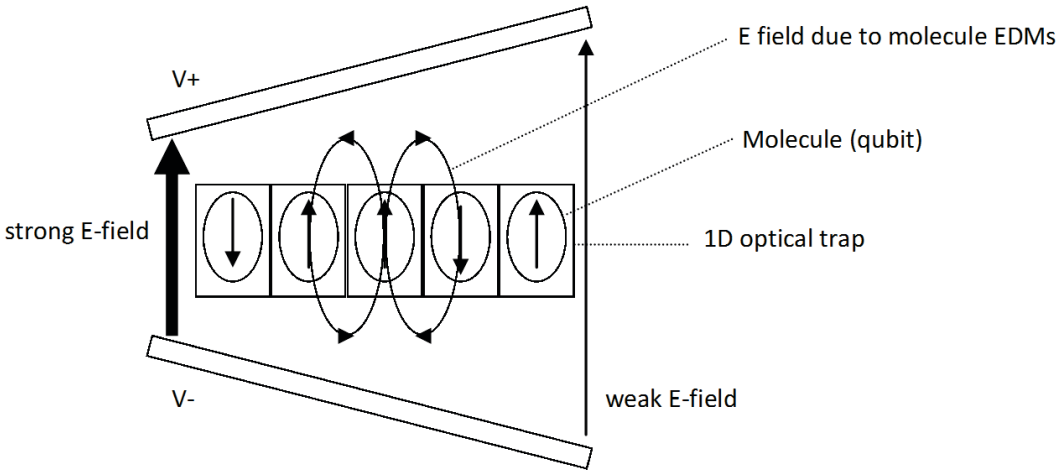

FIGURE 1.1: Schematic diagram of the suggested assembly for a molecular quantum information processor.

can be performed. Together, the two gates are are universal [3]. Readout can be performed destructively by multiphoton ionization and imaging the resulting ions and electrons.

Spontaneous emission lifetimes in this system are typically more than 10^2 s and the dominant source of decoherence is photon scattering from the trap laser. Inelastic scattering of photons from the optical trap can excite molecules to higher states. Therefore, the coherence time of the system is dictated by the Raman scattering rate $R \propto 1/\lambda^3$ [4]. Molecules must be cold so that weaker traps can be used. If laser-cooled ultracold molecules are used as qubits as proposed in example, decoherence times of $\sim$5 s will be possible.

This example shows the main advantages of using molecules in quantum computation. Molecules could provide a platform that is easily scalable compared to systems such as ions, as it is expected that molecules can be assembled at high number densities in regular phases. Furthermore, molecules are easy to manipulate through adjusting the external field, which is not an option that is available in ions and neutral atoms. However, deeper optical traps with higher intensity lead to increased decoherence, so cooling molecules to low temperatures is very important for the successful realization of a molecular quantum computer.

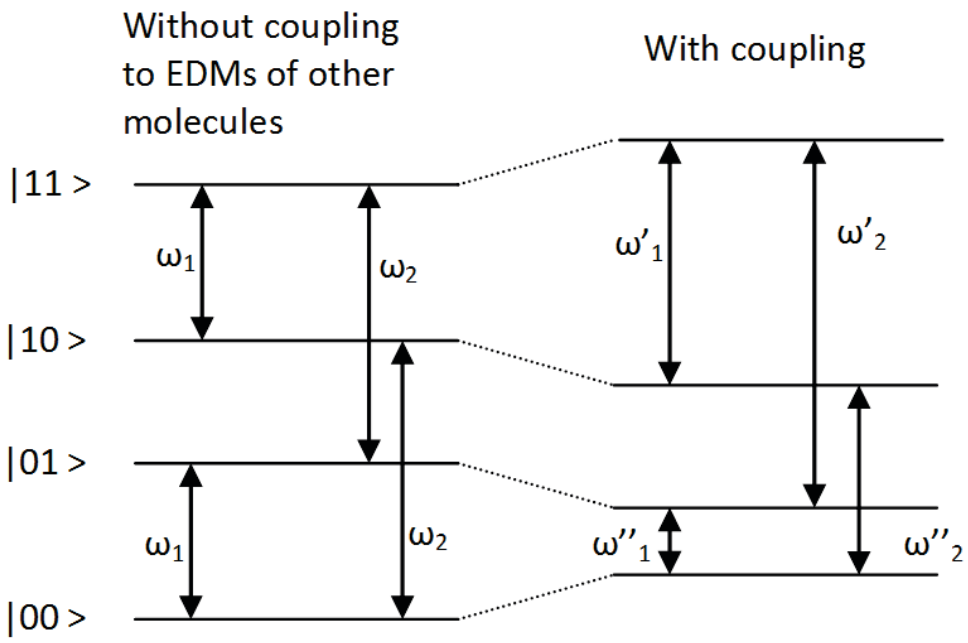

FIGURE 1.2: Energy levels of two-qubit states with and without the effect of the E-field due to other molecules. The Stark interaction shifts the states such that $\omega_1' \neq \omega_1''$ and $\omega_2' \neq \omega_2''$.

1.1.2 Measurement of the Electron Electric Dipole Moment

CPT symmetry is a combination of three symmetries - charge conjugation C (particle to antiparticle), parity P (reflection in space) and time reversal T. The CPT theorem states that all local, Lorentz-invariant quantum field theories are invariant under CPT. This means that if CP symmetry is violated, T symmetry is violated to the same extent. CP violation is necessary to explain why antimatter and matter are not present in equal amounts in the universe.

One way to measure T violation is to measure the electric dipole moment of a fundamental particle. Applying the time reversal operator to a particle with an electric dipole moment gives rise to a different particle with an altered relative configuration of electric dipole moment and spin. We consider the electron. If time reversal symmetry is good, the two configurations should be found equally and electrons should have two degrees of freedom–electric dipole moment orientation and spin. Since this is not true, either the electron has no electric dipole moment or time-reversal symmetry is violated.

The standard model and various extensions to the standard model predict different ranges of values of the electron's permanent electric dipole moment. The measurement of the electron's permanent electric dipole moment is significant in determining the nature of symmetry in our universe, which is closely related to why there is more matter than antimatter in the universe. Researchers have been attempting to make increasingly precise measurements of the electron's electric dipole moment to make the tests of the validity of the standard model and its extensions increasingly stringent. In particular, experiments to measure the electron's electric dipole moment using molecules have been conducted for over a decade [5], and using laser cooled molecules will greatly improve the precision of these measurements [6].

The electron electric dipole moment can be measured by measuring the interaction energy between the electron's electric dipole moment and an external electric field. Inside atoms and molecules, the interaction is enhanced by a factor η, called the enhancement factor, which depends on the atomic or molecular structure and polarization. Heavy, polar molecules provide the best environment for the measurement of the electron electric dipole moment as they have the largest enhancement factors.

Until 2011, the most precise limit of the electron electric dipole moment was measured in the Tl electric dipole moment experiment [7]. The final value given by the experiment was $|d_e| < 1.6 \times 10^{-27}$e.cm, and was measured using an atomic beam experiment. By describing the details of this experiment, I highlight the advantages of using molecules over atoms in the measurement of the electron electric dipole moment.

In this experiment, two beams of Tl passed upwards through a uniform B-field. The spins in the Tl atoms were polarized using a circularly polarized laser beam. As the Tl beams passed through the B-field, their spins precessed. Electric fields in opposing directions were also applied to each of the two beams. After the beams propagated through the electromagnetic fields, the orientation of polarization was measured using another laser beam. The precession frequency f is given by $hf = \mu_B B \pm d_e \eta E$, where B and E are the magnitudes of the electric and magnetic fields. For Tl, $\eta = -585$. The precession rate was different for the two beams because of the electron electric dipole moment.

A grave systematic error arose from the magnetic field due to the motion of the electron through the electric field $\mu \cdot \vec{v} \times \vec{E}$. The extra magnetic field interacted with the magnetic moment of the electron. The interaction is proportional to the electric

field and reverses when the field direction is reversed, just like the interaction due to the electron electric dipole moment. To get over this problem, two more beams of Tl in the opposite direction were added. The motional effects were cancelled out by comparing the upward and downward propagating beams. However, molecules can be immune to this effect.

Another problem was the presence of magnetic fields. It was impossible to reduce the levels of magnetic fields that were present to the levels that would not influence the measurement of the electron electric dipole moment. Therefore magnetic fields were measured and used to make corrections in the data.

We now see that there are two main advantages to using molecules over atoms in electron electric dipole measurement experiments. The first advantage is the large enhancement factors of molecules, which enhances the electric field seen by the electron by millions of times. They are thus proportionally less sensitive to external B-fields. The second advantage is that molecules can avoid the systematic error caused by the $\vec{v} \times \vec{E}$ effect. This is because molecules are cylindrically symmetric, which means they align to the electric field. This makes them very insensitive to B-fields that are perpendicular to E-fields. Thus they are insensitive to the motional magnetic field. This makes the molecular experiment simpler.

The most precise value of the electron electric dipole moment to date was measured at Imperial College London in the YbF electron electric dipole moment experiment and published in 2011 [8]. The obtained value of the electron electric dipole moment is $d_e = (-2.4 \pm 5.7_{\text{stat}} \pm 1.5_{\text{syst}}) \times 10^{-28} e.\text{cm}$, where e is the charge on the electron, which sets a new upper limit of $|d_e| < 10.5 \times 10^{-27} e.\text{cm}$. This result is consistent with zero. In this experiment [9], the electron electric dipole moment is measured using the splitting between two magnetic hyperfine levels of ground state YbF molecules due to the interaction between the electron electric dipole moment with an external electric field.

First, a beam of YbF is produced by supersonic expansion and laser ablation. These molecules are prepared in the state $|F, m_F\rangle = |0, 0\rangle$. Next, they are excited into a superposition state $(|1, +1\rangle + |1, -1\rangle)/\sqrt{2}$ by a radio-frequency (rf) π pulse. The beam then propagates through an electric field and a B-field. There is precession about the B-field and the two states acquire a relative phase such that the state becomes $(e^{i\phi}|1, +1\rangle + e^{-i\phi}|1, -1\rangle)/\sqrt{2}$. Having been subjected to the fields, the beams are recombined by a second rf π pulse and probed. The resulting state is a superposition of the states $|0, 0\rangle$, $|1, +1\rangle$ and $|1, -1\rangle$, where the amplitude of the $|0, 0\rangle$ state is $\cos\phi$. The phase acquired in interaction time T is given by

$\phi = 2(\mu_B B - \eta d_e E)T/\hbar$ and the fluorescence signal is proportional to $\cos^2(\phi/2)$. By changing the direction of the electric field, the electron electric dipole moment manifests itself through the variation in ϕ - the fringe spacing of the interference pattern.

As well as the YbF experiment, there are are electron electric dipole moment measurement experiments using ThO [10] and PbO [11], HfF^+ [12] and WC [13]. Using laser cooling to collimate a beam of YbF from a slow source then launching in a fountain may enable even more precise measurements than these experiments.

1.1.3 High Resolution Spectroscopy

Cooling molecules is useful in the areas of high resolution spectroscopy as it generally enables samples to be probed for longer periods of time, resulting in more precise spectra. To illustrate this, I specifically describe the benefits of using cold molecules in infrared spectroscopy, and in searches for changes in fundamental constants, which is an application of molecular spectroscopy.

Infrared spectroscopy can be used to determine which molecular species are present in a sample and their respective number densities. It plays a crucial role in many fields including astrophysics and atmospheric science. The Einstein A coefficient for molecular rovibrational levels must be known to analyse infrared spectra. The most direct way of finding the Einstein A coefficient is to measure the radiative lifetime of individual states. The difficulty in this approach is that molecules in a low density gas need to be available for long observation times (typically ms to seconds). This allows the monitoring of the population of a specific state over time without the effect of collisions.

The radiative lifetime of vibrationally excited OH radicals has been measured directly by confining the molecules in an electrostatic trap [14]. In this experiment, the molecules are slowed in a Stark decelerator before being loaded into the trap, and are detected by laser-induced fluorescence. Using trapped molecules gives radiative lifetime measurements with an unprecedented level of accuracy. The accuracy can be increased further by laser cooling molecules. Previously, the Einstein A coefficients had been measured indirectly from absorption measurements, which suffer from limited accuracy caused by the unstable nature of many of the chemical species of interest.

The study for the search of the variation in the fine-structure constant α has far-reaching consequences, as a variation in fundamental constants in space and time mean that Lorentz invariance and CPT symmetry is violated. The variation of fundamental constants is predicted by theories that have been developed in an attempt to unify gravity with the other fundamental forces. The largest variation of α may have occurred during the early universe, and a method of measuring this using OH megamasers has been recently attracting attention. A megamaser is a type of astrophysical maser which is a naturally occurring source of stimulated spectral line emission and is characterized by its large isotropic luminosity. In order to make precise α variation measurements from these megamasers, spectroscopy of relevant microwave transitions are performed in the laboratory using cold beams of OH radicals [15]. In this experiment, the molecules are cooled and slowed using a Stark decelerator before being probed using microwave spectroscopy. The spectroscopic resolution is determined by the interrogation time, and therefore is improved significantly by using cold molecules. Using cold molecules is predicted to yield a sensitivity of 1 ppm for $\Delta\alpha/\alpha$ over $\sim 10^{10}$ yr.

1.1.4 Study of Chemical Reactions in the Ultracold Regime

Cold molecules will enable new investigations into the control and study of chemical reactions at low temperatures [16]. A molecule can only be manipulated with external fields if its translational energy is lower than the energy due to its interaction with an electromagnetic field. In the study of chemical reactions, the ultracold regime is generally defined to be the temperature regime where the collision dynamics is dominated by single partial-wave scattering ($<\sim$1mK). Wigner's threshold law [17] holds in the ultracold regime. Wigner's threshold law states that the collision cross-section between particles of very low relative velocity is independent of temperature. The collision cross-section depends only on the energy and relative angular momentum of the colliding particles. This gives ultracold molecules unique reaction properties. Calculations show that chemical reaction rates can be large in the limit of absolute zero temperature.

There are many proposals and implementations of mechanisms to control molecular dynamics using external fields [18]. Zeeman and Stark effects can be used to make forbidden transitions happen or to suppress allowed transitions. For instance, a Zeeman transition can induce the dissociation of a loosely bound molecule when the energy of a bound state of one electronic level and an unbound state in another electronic level are brought close enough by a magnetic field [19]. External fields

can break the spherical symmetry of a system, such that states of different total angular momenta are coupled. Furthermore, external fields can increase the energy separation between the initial and final states of a reaction that is suppressed by a centrifugal barrier, thus increasing the reaction rate. Intermolecular interaction potentials may be modified due to external fields. This causes long-range potential minima due to avoided crossings, allowing the formation of long-range diatomic molecules. In a mechanism similar to Feshbach resonances, the presence of a resonance state near threshold can increase the zero temperature reaction rate of an abstraction reaction, which is a reaction that takes any atom away from another chemical species.

Possible areas of future research in cold chemistry include coherent control of chemical reactions, investigation of weak intermolecular interaction forces and testing the limits of classical molecular dynamics and thermodynamics.

1.1.5 Simulating Strongly-Interacting Many-Body Quantum Systems

Polar molecules have strong, long-range, anisotropic interactions which can be controlled. This makes them ideal for exploring quantum phase transitions and simulating strongly-interacting many-body quantum systems [20, 21]. In particular, cold- and ultracold molecules in optical lattices provide highly controllable systems for testing theories of quantum phase transitions and engineering relevant Hamiltonians for spin lattice models.

The discovery of Bose-Einstein condensation of dilute atomic gases revolutionized modern atomic, molecular and optical physics. In the same way, the molecular Bose-Einstein condensate (BEC) will open up a whole new area of research. The physics of strongly correlated quantum gases, which can be characterised by a BEC of particles that have dominant dipole-dipole interactions, is predicted to be unique. Using polar molecules with strong dipole-dipole interactions will enable the observation of quantum phase transitions that cannot be seen with atoms due to their weaker interactions. For instance, this could lead to the realization of supersolids [22].

We estimate the temperature to which molecules need to be cooled to form a dipolar BEC by estimating the size of the dipole-dipole coupling between a pair of polar molecules. For simplicity, we calculate the dipole-dipole interaction energy of one

pair of dipolar molecules in terms of temperature. We take the electric dipole moment of each molecule to be 1 D, and assume that they are trapped in a lattice, so that the separation is $\lambda/ = 250\,\text{nm}$. Then the temperature is given by

$$T = -\frac{2\mu_1\mu_2}{4\pi\epsilon_0 r^3} \times \frac{1}{k_\text{B}} = 1\,\mu\text{K}, \tag{1.1}$$

where ϵ_0 is the permittivity of free space and k_B is the Boltzmann constant.

A dipolar BEC has unique stability properties. A spatially homogeneous condensate with attractive interparticle forces in a harmonic trap is always unstable against the gas collapsing inwards. A dipolar BEC can be stable against collapse if the negative pressure caused by the interparticle attraction is balanced by the quantum pressure imposed by the trapping potential, which is absent in a uniform gas [23]. The quantum pressure is similar to the thermal pressure in a classical gas. This means that the stability properties depend on the cloud shape, and therefore the trap geometry. The trap geometry can be changed by tuning experimental parameters, such as the optical lattice wavelength, intensity or the angle between the dipole-dipole vector and the 2D lattice plane normal (in the case of a 2D optical lattice).

A dipolar BEC exhibits a variety of quantum phases, which can be controlled by tuning the interaction between the particles and controlling the phase transitions. Accessible phases include superfluid, supersolid, Mott insulator, checkerboard and collapse phases. In the Mott insulator phase, each lattice site has single occupancy. The checkerboard insulating phase has single occupancy on alternating sites. In the collapse phase, the system collapses due to attractive local interactions. The rich variety of accessible phases are bound to lead to many applications. For example, the method of quantum computation using trapped polar molecules described in section 1.1.1 suggests a loading mechanism that relies on the Mott insulator phase for unity filling of lattice sites.

The physics of strongly interacting quantum gases could also be investigated in atoms. However, polar molecules with large permanent electric dipole moments have stronger, long-range anisotropic dipole-dipole interactions compared to atoms [24]. Molecular dipole moments typically range from 0.1 to 1 D (Debye), whereas the magnetic dipole moment of an atom is typically equivalent to an electric dipole moment of the order of 10^{-2} D. Ultracold molecules are therefore the most suitable candidates to form dipolar BECs, and at the same time, the investigation of strongly correlated quantum gases is considered to be one of the most interesting applications of ultracold molecules.

1.2 Other Ways of Making Cold Molecules

Many groups are investigating different methods of making cold molecules [25]. Direct methods include buffer-gas cooling, Stark deceleration, deceleration by pulsed optical fields, deceleration via collisions in crossed molecular beams, supersonic expansion from a counter-rotating nozzle, and selection of the low-velocity tail of a Maxwell-Boltzmann distribution of molecules in an effusive beam. Indirect methods include photoassociation and magnetoassociation of ultracold atoms. This section introduces a few of the most successful techniques.

1.2.1 Feschbach Resonances

Techniques that use Feschbach resonances have sucessfully produced high phase-space density samples of cold molecules [26, 27].

A Feshbach resonance is the behaviour of scattering properties in atoms as a function of an applied field as the energy level of a bound molecular state crosses the free atom energy level asymptote. This resonance arises because the interatomic potential curve for two atoms is unique for different combinations of the atomic hyperfine states. For instance, the Cs F=3 : Cs F=2 interatomic potential is slightly higher in energy than the Cs F=2 : Cs F=2 potential. In an applied magnetic field, both the atomic levels and the molecular levels split and shift. The hyperfine states have different Zeeman shifts. By adjusting the magnetic field, a bound molecular state of one of the hyperfine levels can be made to coincide with the free atom energy level asymptote of another. At this instance, there is a resonance in the scattering length and molecules with the same energy as the free atoms can be formed. Feshbach resonances are useful in forming cold molecules from cold atoms when there is an avoided crossing at the value of magnetic field where the free state and the bound state pass over each other. By tuning the magnetic field slowly enough, the avoided crossing is followed adiabatically and pairs of atoms are converted into loosely-bound Feshbach molecules. The population might then be coherently transferred to a deeply bound state by stimulated Raman adiabatic passage (STIRAP).

Feshbach resonances allow the direct production of quantum degenerate molecules but the states tend to have short lifetimes because they are very weakly bound. Another drawback is that it can only be applied to species formed from atoms that can be laser cooled. Homonuclear diatomic molecules such as $^{133}Cs_2$ and $^{40}K_2$ have

been formed via Feshbach resonances. Feshbach resonances have been observed in heteronuclear dimers such as RbK.

1.2.2 Photoassociation

Ultracold polar molecules of translational temperatures of $\sim 100\mu K$ have been produced by photoassociation in conjunction with a laser-stimulated transfer process [28].

In photoassociation, ultracold molecules are formed by exciting free ultracold atoms to a bound molecular state in a higher electronic state. This is usually performed by adding an extra laser that is slightly red-detuned from the cooling transition to the magneto-optical trap containing the atoms. The resulting molecules are produced in low-lying rotational states due to the centrifugal barrier in ultracold collisions, but in highly excited vibrational states. Decay to a bound state is highly unlikely so decay leads to many free atomic states with a lot of kinetic energy. The molecules that are formed tend to be loosely bound. In a diatomic molecule, the probability of decay from a higher vibrational level to a lower vibrational level is proportional to the square of the overlap of the upper and lower vibrational wavefunctions. The square of the overlap is known as the Franck-Condon factor. The reason why photoassociated molecules tend to be loosely bound is because the wavefunction amplitude is large and slowly oscillating at the outer turning point of the internuclear potential, meaning that transitions to unbound states have higher associated Franck-Condon factors and therefore are more likely.

Homonuclear and heteronuclear diatomic molecules have been formed via photoassociation. Work in ultracold photoassociation has been reviewed extensively by Jones *et al.* [29]. A disadvantage of the method is that the production is limited to species formed from atoms that can be laser cooled. In addition, the production rate of molecules is slow and it is difficult to reach the ground vibrational state. Many methods, such as the use of STIRAP [30] and the idea of using chirped pulses of the photoassociation laser [31], are being investigated to overcome the problem of the low Franck-Condon factor and have yielded results [32].

1.2.3 Stark Deceleration and Electrostatic Trapping

Molecules experience a force in an electric field gradient due to their Stark shift. Stark decelerators take advantage of this effect to slow molecules, both in strong-

and weak-field seeking states [33]. In the weak-field case, the decelerator consists of an array of electrodes creating multiple potential wells. The molecules lose kinetic energy as it climbs a potential hill, leaving a well. As they approach the potential maximum, the field profile is inverted so the molecules are always going uphill. There is a tradeoff between the amount of kinetic energy removed and the phase-space acceptance of molecules. The group of molecules that are accepted get focussed longitudinally since molecules that are ahead lose more kinetic energy compared to those that are behind. There is also a transverse focussing effect away from the electrodes. A magnetic analogue of the Stark decelerator using Zeeman shifts has also been developed [34].

Sufficiently slow molecules can be loaded into an electrostatic trap [35], where the weak-field seeking molecules are trapped in a potential minimum. A molecular storage ring, providing confinement just in the transverse direction, has also been realised [36].

Slowing and trapping of high-field seeking states are of special interest as they do not decay inside traps. Polar molecules in low rotational states tend to become high-field seeking at relatively low fields. A local electric field maximum is forbidden by the Maxwell relations so a switched saddle-shaped field surface is used in AC trapping [37]. In this switched field, molecules undergo micromotion in step with the field switching. The variation in kinetic energy with distance from the saddle-point creates a net potential minimum in the trap centre.

1.2.4 Buffer Gas Cooling and Magnetic Trapping

In buffer gas cooling [38], molecules are brought into thermal contact with cryogenically cooled helium gas. Particles in the two gases collide elastically and reach a thermal equilibrium. A buffer gas-loaded magnetic trap [39] consists of a cryogenic cell located inside a superconducting magnet. The application of a magnetic field causes Zeeman splitting in the molecules into those in weak-field seeking and strong-field seeking states. The cell is thermally anchored to a dilution refrigerator. The magnets are two coils in anti-Helmholtz configuration such that weak-field seekers are trapped in the centre, while strong-field seekers are lost. The molecules can be monitored using laser-induced fluorescence. Any paramagnetic molecule can be cooled to about 100 to 300mK in buffer gas cooling. The molecules' final temperature is limited by the minimum temperature of the helium, corresponding to a number density providing sufficient collisions for rapid

rethermalization. There is a tradeoff between efficient thermalization and a slow beam.

Cooled molecular beams [40] can be made by buffer-gas cooling molecules in a cell with an orifice. A high flux of molecules exits the cell with translational and rotational temperatures near 1K.

1.3 Cooling Molecules to Temperatures below 10 mK

The methods of cooling molecules directly, or producing cold molecules through association, described in the preceding section, can yield molecules of temperatures down to around 10 mK but not any lower. In the same way that evaporative cooling needs to be employed to cool atoms down beyond the recoil limit to degeneracy, a further technique needs to be employed to cool molecules to degeneracy. Currently, the two candidates for this are evaporative cooling and sympathetic cooling.

Evaporative cooling in molecules has recently been demonstrated in OH molecules although it had previously been considered to be difficult [41]. In this experiment, hydroxyl radicals in a molecular beam are Stark decelerated then trapped in a high gradient magnetic quadrupole trap, where evaporation takes place. The principle of evaporative cooling in molecules is the same as for atoms, and is very simple. The temperature of the sample is decreased by selectively removing particles with relatively high energies. However, this had been difficult in molecules due to insufficient elastic collison to inelastic collision ratios. The molecules thermalize through elastic collisions so more elastic collisions mean a faster thermalization time, but inelastic collisions heat the molecules and cause trap loss. The OH experiment shows that the elastic collision rate is greater than the inelastic collision rate in OH. In this experiment, the molecular temperature is reduced by an order of magnitude from 51 mK to 5.1 mK.

Another potential method of cooling moelcules is sympathetic cooling [42, 43]. In this technique, trapped molecules are placed in thermal contact with ultracold atoms such that they thermalize. To allow sufficient thermalization time, both the molecules and atoms need to be trapped. However, trapping molecules is challenging as only molecules in weak-field seeking states can be trapped and the ground state is strong-field seeking. Therefore, inelastic collisions can eject

molecules from the trap. To realize sympathetic cooling, the elastic to inelastic cross section need to be large, or strong-field seeking states need to be trapped.

Chapter 2

The SrF Molecule

Laser cooling is a successful technique that has been applied to cool atoms to ultracold temperatures. In laser cooling, atoms are cooled by the transfer of energy from the atoms into the light field by absorption of photons with a momentum in one direction, followed by emission in a random direction. However, the effect of scattering one photon is very small, and it is crucial for the atom to continuously scatter photons from the cooling lasers. To achieve this, the atom must have a closed transition, where the species decays back to the initial state after excitation. Laser cooling of molecules is difficult compared to atoms as closed transitions are rare in molecules due to their vibrational and rotational degrees of freedom. This chapter presents a brief overview of the relevant molecular theory, the features of SrF that make it suitable for laser cooling, as well as some difficulties of cooling SrF, and some rough calculations to show the practical requirements for laser cooling SrF (including the number of photons that need to be scattered).

2.1 A Brief Introduction to the Structure of Diatomic Molecules

This section is an introduction to the structure of diatomic molecules, with an emphasis on the aspects required to explain this experiment. The main source of reference for this section is [44], which provides in-depth coverage of the subject.

2.1.1 Electronic,Vibrational and Rotational Structure

The basic idea of molecular structure, which involves the separation of electronic and nuclear motion in the molecular wavefunction into electronic, vibrational and rotational parts, originates from the work of Born and Oppenheimer [45]. They made the observation that the nuclear mass is much bigger than the electronic mass, but the electrostatic forces acting on the nucleus are the same as the electrostatic forces acting on the electrons. This means that the nuclei move slowly compared to the electrons. So, rather than solving the problem of the system where both the electrons and the nuclei are moving, they solved the problem with fixed nuclei. For a diatomic molecule, the procedure is to freeze the nuclei with a fixed separation R. Then the Schrödinger equation is solved numerically, with the internuclear separation as a parameter, in order to obtain the eigenvalues and eigenfunctions of the electronic part as a function of the internuclear separation. The energies as a function of the internuclear separation are called the potential energy curves. In the Schrödinger equation for the nuclear motion, the potential is exactly the potential energy curve given by solving the electronic part. This nuclear wave equation can be separated and solved much in the same way as in the case of the hydrogen atom, and the upshot is that the total energy of a diatomic molecule is given by the sum of its electronic, vibrational and rotational energies, and that the total wavefunction is a product of the electronic, vibrational and rotational eigenstates. In summary, the total energy of a molecule is given by

$$E = E_e(R_0) + E_v + E_r, \tag{2.1}$$

where E_n is the electronic energy eigenvalue at equilibrium internuclear separation R_0, E_v is the vibrational energy, given to a good approximation by the harmonic oscillator energy levels $E_v = (v{+}1/2)\hbar\omega$ ($\omega = \sqrt{k/m}$, $k = \frac{d^2E_e(R)}{dR^2}|_{R=R_0}$) particularly at lower vibrational levels, and finally, E_r is the rotational energy given by

$$E_r = BJ(J+1) \tag{2.2}$$

where $B = \hbar^2/I$ and I is the moment of inertia in the axis that is perpendicular to the internuclear axis. The total wavefunction of a molecule is the product of the electronic, vibrational and rotational eigenstates

$$\Psi_{e,v,J,M_J}(R,\, r_i) = \psi_e(R,\, r_i)R^{-1}f_v(R)Y_{J,M_J}(\Theta, \Phi) \tag{2.3}$$

where R is the internuclear separation, (r_i, Θ, Φ) is electron's location in polar coordinates, ψ_e is the electronic eigenfunction, f_v is the vibrational eigenfunction, which is the harmonic oscillator wavefunction to a good approximation at lower vibrational levels, and Y_{J,M_J} is the angular part, which is the relevant spherical harmonic function.

2.1.2 Angular Momenta

The Hund's coupling cases are approximations of angular momenta coupling in real diatomic molecules. In each case, specific terms in the molecular Hamiltonian involving couplings between angular momenta (ΔE^{SO} the spin-orbit interaction energy, ΔE^{el} the electrostatic coupling of the electronic orbital angular momentum $\vec{L}$ to the internuclear axis, or ΔE^{rot} the rotational coupling of $\vec{L}$ and the electronic spin angular momentum $\vec{S}$ to the total angular momentum $\vec{J}$) are assumed to dominate over the other terms. There are five cases, labelled by the letters (a) to (e), but most molecules, including those relevant to this experiment are best described by (a) or (b).

We use the following notation to describe the angular momenta of the diatomic molecules;

$\vec{L}$ The electronic orbital angular momentum

$\vec{S}$ The electronic spin angular momentum

$\vec{J_a} = \vec{L} + \vec{S}$ The total electronic angular momentum

$\vec{J}$ The total angular momentum of the system excluding hyperfine interactions.

$\vec{N} = \vec{J} - \vec{S}$ The total angular momentum minus the electron spin

$\vec{R} = \vec{N} - \vec{L}$ The rotational angular momentum of the nuclei

In Hund's Case (a), the electrostatic coupling of $\vec{L}$ and $\vec{S}$ to the internuclear axis is strong, the spin-orbit interaction energy is intermediate, and the coupling between the rotational and the electronic motion is weak. $\vec{L}$ and $\vec{S}$ have well-defined projections onto the internuclear axis. given by Λ and Σ respectively. $\Omega = \Lambda + \Sigma$ and is a projection onto the internuclear axis. The basis states, labelled by the good quantum numbers in this coupling case is $|\Lambda\rangle\,|S,\,\Sigma\rangle\,|J,\,\Omega,\,M_J\rangle$. The rotational energy levels are given by $E_{\mathrm{rot}} = BJ(J+1)$.

In Hund's Case (b), the spin-orbit interaction is weak compared to the effect of the rotation on the spin. In this case, $N = \Lambda + R$ and $\vec{J} = \vec{N} + \vec{S}$. The basis states are denoted $|\Lambda\rangle\,|(N,\, S)\, J,\, M_J\rangle$, and the rotational energy levels are given by $E_{\rm rot} = BN(N+1)$.

The rotational levels are split further by the interaction of the nuclear spin with the other angular momenta of the molecule. If the two nuclei are given by $\vec{I}_1$ and $\vec{I}_2$, the total nuclear spin vector is $\vec{I} = \vec{I}_1 + \vec{I}_2$, and the total angular momentum vector is $\vec{F} = \vec{J} + \vec{I}$.

2.1.3 Labelling of Molecular States

The electronic states of the molecule are labelled in the form

$$(\text{unique letter})^{2S+1}\Lambda_{\Omega}^{+/-}, \tag{2.4}$$

where the letter indicates the electronic energy level following the convention where X is the ground electronic level, A is the first excited electronic level, B is the second excited electronic level and so on. Λ is the projection of the orbital angular momentum onto the internuclear axis (which can be Σ, Π, Δ, ... as in atoms) and Ω is the projection of the total angular momentum onto the internuclear axis. For Hund's case (b), Ω is not defined. The reflection symmetry along an arbitrary plane containing the internuclear axis is indicated as a superscript.

2.1.4 Transition Dipole Matrix Element

As is well-known with atoms, the intensity of an electric dipole transition is proportional to the square of the matrix element of the dipole operator between the initial and final states:

$$d_{12} = \langle \Psi_1 |\, \vec{d} \cdot \vec{\epsilon}\, | \Psi_2 \rangle\,. \tag{2.5}$$

For a molecule, the dipole operator is

$$\vec{d} = e \sum_N Z_N \vec{R}_N - e \sum_i \vec{r}_i, \tag{2.6}$$

where e is the electronic charge, Z is the nuclear charge, and $\vec{R}$ and $\vec{r}$ are the positions in the lab frame of the nuclei and electrons respectively. We take some steps in order to simpify the expression of the transition dipole matrix elements for molecules. Firstly, we transform the coordinates into the rank 1 spherical tensor system of V_{-1}, V_0 and V_{+1}, which are related to the Cartesian coordinatesV_x, V_y and V_z in the following way;

$$V_0 = V_z\,; \quad V_\pm = \mp\frac{V_x \pm iV_y}{\sqrt{2}}. \tag{2.7}$$

Then we rotate the coordinate system so that the rotated z-axis lies along the internuclear axis. Then we can relate the dipole operator in the lab frame corresponding to linear polarization d_0 to the dipole operator components in the rotated frame μ_k in the following way;

$$d_0 = \sum_{k=-1}^{1} D_{0k}(\Theta,\,\Phi)\mu_k. \tag{2.8}$$

Following this, we obtain the transition dipole matrix element in a form where the angular part and the rest of the expression are separate.

$$d_{12} = M_{\rm rot}\int f^*_{v'}(R)\,\mu^n_e(R)\,f_v(R)\,dR\,; \tag{2.9}$$

$$M_{\rm rot} = \int Y'_{J'M'}\,D_{00}\,Y_{JM}\sin\theta\,d\Theta\,d\Phi; \quad \mu^n_e(R) = \int \psi^*_n(R,\vec{r}_i)\,\mu_z\,\psi_n(R,\vec{r}_i)\,d\vec{r}_i \tag{2.10}$$

The vibrational wavefunctions are only large close to the equilibrium internuclear separation R_0, so we can Taylor expand $\mu^n_e(R)$. Then to the lowest order, we have the result;

$$d_{12} = M_{\rm rot}\,\mu^{n',n}(R_0)\int f^*_{v'}(R)\,f_v(R)\,dR. \tag{2.11}$$

Therefore, the amplitude of transitions between electronic levels that change vibrational level is proportional to the factor

$$\left(\int f^*_{v'}(R)\,f_v(R)\,dR\right)^2, \tag{2.12}$$

and this is known as the Franck-Condon factor.

From the transition dipole matrix element given in equation 2.9, we can derive some selection rules which will simply be stated here. The total angular momentum quantum number must vary as $\Delta J = 0, \pm 1$ but not from 0 to 0, $\Delta M = 0, \pm 1$, and the parity must change. There are no rotational transitions that do not change electronic level in homonuclear diatomic molecules, where the dipole moment is zero.

Transitions from $J \to J-1$, from $J \to J$ and from $J \to J+1$, where the first J is the lower energy state, are denoted by $P(J)$, $Q(J)$ and $R(J)$ respectively.

2.2 Electronic and Vibrational Levels

We choose to laser cool SrF molecules on the $P(1)$ transition $X^2\Sigma^+(v''=0, N''=1, J''=1/2 \text{ and } J''=3/2) \leftrightarrow A^2\Pi_{1/2}(v'=0, J'=1/2)$ as the main cooling transition, and this choice is justified in the rest of this chapter.

The $P(1)$ transition, which we have chosen, is between the ground electronic state $X^2\Sigma^+$ and the first excited electronic state $A^2\Pi_{1/2}$. The lifetime of the $A^2\Pi_{1/2}$ excited state is short at $\tau = 24\,\text{ns}$ [46], which ensures a fast scattering rate. Furthermore, there are no other intervening electronic or rotational levels that the molecules can decay to. This is discussed further in section 2.3. However, there are no strict selection rules that govern the decay of an excited electronic state into other vibrational levels. Each additional vibrational level that the molecules leak into needs a repump laser, so it is preferable to have significant decays to fewer vibrational levels.

The probability amplitude of the allowed electric dipole transitions between two molecular wavefunctions that change the vibrational state is proportional to the Franck-Condon factor, which is the square of the overlap integral between the initial and final vibrational wavefunctions. We can estimate the Franck-Condon factors by approximating small variations around the equilibrium position $R_0 = \sqrt{\hbar/4\pi c\mu B_e}$ to be in the internuclear potentials as the harmonic oscillator potentials $U = \frac{\mu\omega^2}{2}(R-R_0)^2$, where μ is the reduced mass and ω is the harmonic vibrational frequency. This gives the energy levels $\hbar\omega\left(v+\frac{1}{2}\right) = \omega_e\left(v+\frac{1}{2}\right)$. We use the vibrational constant $\omega_e = 502.0\,\text{cm}^{-1}$ and equilibrium internuclear separation $R_0 = 3.921\,a_0$ for the X state, and $\omega_e = 509.5\,\text{cm}^{-1}$ and $R_0 = 3.898\,a_0$ for the A state,

	$X(v''=0)$	$X(v''=1)$	$X(v''=2)$
$A(v'=0)$	0.98	1.8×10^{-2}	6.0×10^{-5}

TABLE 2.1: Franck-Condon factors calculated using the approximation that the internuclear potentials are harmonic oscillators.

Initial state	Final state	Frequency (GHz)
$\|X^2\Sigma,\ v''=0,\ N''=1\rangle$	$\|A^2\Pi,\ v'=0,\ J'=1/2+\rangle$	451,958
$\|X^2\Sigma,\ v''=0,\ N''=1\rangle$	$\|A^2\Pi,\ v'=1,\ J'=1/2+\rangle$	437,041
$\|X^2\Sigma,\ v''=1,\ N''=1\rangle$	$\|A^2\Pi,\ v'=1,\ J'=1/2+\rangle$	452,181
$\|X^2\Sigma,\ v''=0,\ N''=0\rangle$	$\|A^2\Pi,\ v'=0,\ J'=1/2-\rangle$	451,974

TABLE 2.2: Measured frequencies of relevant transitions in SrF.

where a_0 is the Bohr radius, as found in [44] and [47]. The resulting relevant Franck-Condon factors are shown in table 2.1. SrF has a highly diagonal Franck-Condon matrix so $\Delta v = 0$ transitions are preferred.

We can also understand conceptually why the Franck-Condon matrix is highly diagonal. The SrF bond is an ionic bond created by one electron being transferred from the strontium to the fluorine. Since fluorine is the most electronegative element, the remaining valence electron is highly localized on the strontium. This is also the electron that gets excited in the optical spectrum, and has little influence on the bond. This means that the ground electronic state and first electronic excited state have very similar internuclear potentials, resulting in a highly diagonal Franck-Condon matrix.

Another advantage of SrF as a target species for laser cooling is that all relevant transitions are at frequencies that are accessible by diode lasers. The list of relevant measured frequencies are shown in table 2.2.

2.3 Rotational and Hyperfine Levels

Our chosen cooling transition (the $P(1)$ transition) is from a $N'' = 1$ rotational state to an $N' = 0$ rotational state. Recall the angular momentum selection rules

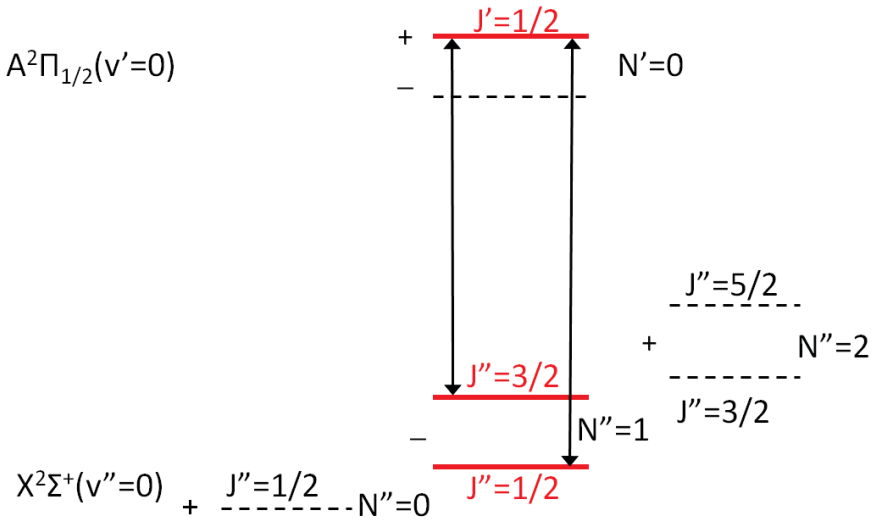

FIGURE 2.1: The allowed decay channels to the $v = 0$ level after driving the $P(1)$ transition. Other vibrational levels and the hyperfine splittings are not shown.

in rotational transitions in molecules, which are $\Delta N = 0, \pm 1$ but not $N' = 0$ to $N'' = 0$. In addition, allowed transitions involve a parity change. We can see that as a consequence, only decays to the original rotational state $N'' = 1$ is allowed. This is a clever trick proposed in [48], and in general, it works for transitions where $N' = N'' + 1$. The allowed decay channels after driving the $P(1)$ transition are summarized in figure 2.1.

We have now established that there is no concern for leaks into other rotational levels, as the there is a closed transition between the involved rotational levels for a given vibrational transition. However, in the $X^2\Sigma$ electronic ground state, the $N = 1$ rotational state with $\Lambda = 0$ is further split into two states. This arises from the spin-rotation interaction due to the unpaired electron spin of (S=1/2) forming the total angular momentum $\vec{J} = \vec{N} + \vec{S}$ with $N - S \leq J \leq N + S$. Then the resultant $\vec{J}$ is coupled with the the nuclear spin (I=1/2), the hyperfine interaction, forming the total angular momentum $\vec{F} = \vec{J} + \vec{I}$. This Σ^+ ground state is best described using Hund's case (b), as it is in a light molecule, where $\Delta E^{\text{el}} \gg E^{\text{rot}} \gg E^{\text{SO}}$, and E^{SO} is 0 for $\Lambda = 0$. The coupled momenta $\hat{J}$ basis is a good basis to describe the Hamiltonian. The effective Hamiltonian [49] is given by

$$H = H_0 + H_{\text{int}} \tag{2.13}$$

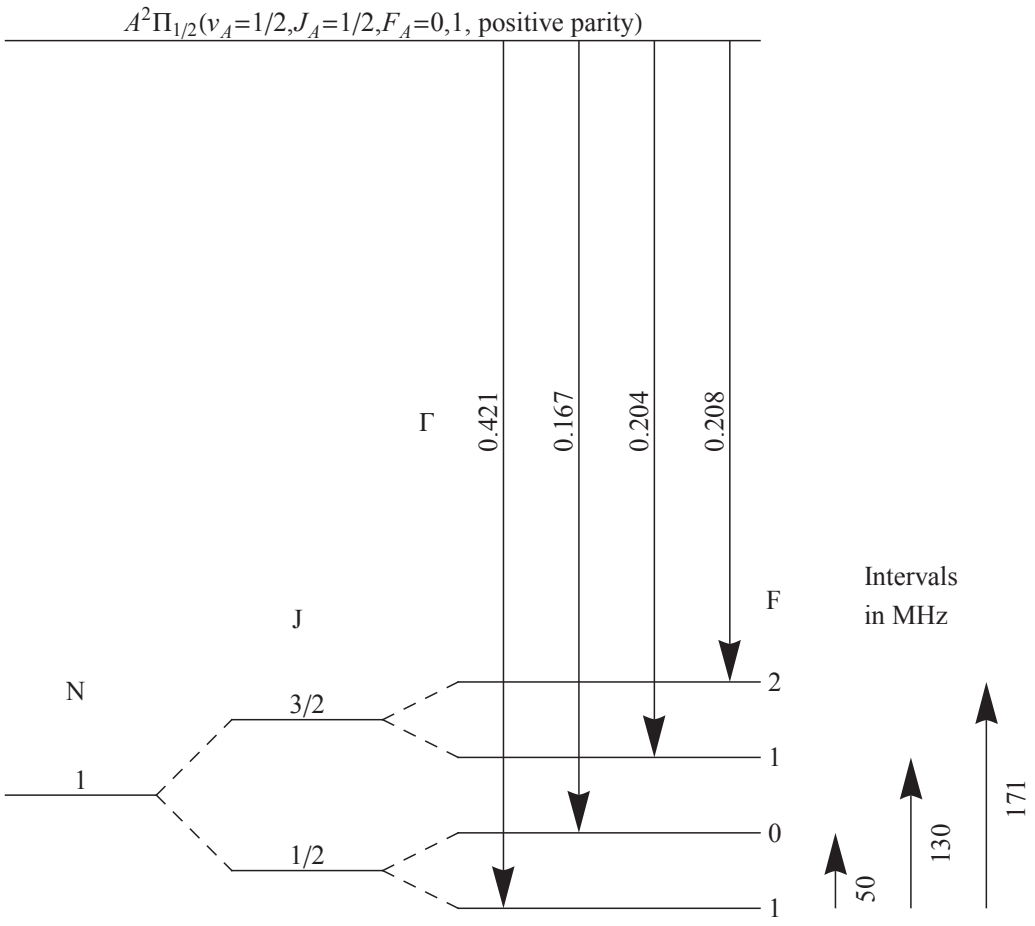

FIGURE 2.2: The calculated hyperfine splittings and branching ratios Γ in the $P(1)$ transition.

where

$$H_0 = B\mathbf{N}^2 + \gamma\mathbf{N}\cdot\mathbf{S}\,; \quad H_{\text{int}} = b\mathbf{I}\cdot\mathbf{S} + c(\mathbf{I}\cdot\hat{z})(\mathbf{S}\cdot\hat{z}) + C_I\mathbf{I}\cdot\mathbf{N}. \tag{2.14}$$

The hyperfine splittings and branching ratios can be calculated using standard methods in angular momentum algebra, using the constants $B = 7.510838\,\text{GHz}$, $b = 97.0834\,\text{MHz}$, $c = 30.268\,\text{MHz}$, $C_I = 0.0023\,\text{MHz}$, $\gamma = 74.79485\,\text{MHz}$ from [50]. The results are summarized in figure 2.2.

We can neglect the hyperfine splittings in the upper $A^2\Pi_{1/2}(v' = 0)$ level, as they are 100 times smaller than the splittings in the $X^2\Sigma^+(v'' = 0)$ level, which means that they are well within a typical laser linewidth of $\sim$ MHz.

Once molecules are excited from any hyperfine state in the $X(N'' = 1)$ level to the $A(N' = 0)$ level, they can decay back to any of the four hyperfine states in the

initial level with a probability given by the branching ratios. Therefore, all four hyperfine levels must be pumped at the same time.

An additional point to note is the decay from the excited $A(N' = 0)$ state to the $X(N'' = 3)$ state due to hyperfine mixing between the $X(N = 3, F = 2)$ and $(N = 1, F = 2)$ states. The branching ratio of this leak is small ($\leq 10^{-6}$ [51]), and can be neglected in this case.

2.3.1 Notation for Transitions in this Thesis

I will use a shorthand for the transitions that are used frequently in the rest of this thesis. Each of the P(1) hyperfine transitions $X^2\Sigma^+(v'', N'', J'', F'') \rightarrow A^2\Pi_{1/2}(v', J' = 1/2)$ will be denoted by $\mathrm{X}_{v'',N''}(J,F) - \mathrm{A}_{v',1/2}$. The four P(1) lines $X^2\Sigma^+(v'', N'' = 1, J'' = 1/2, F'' = 0 \text{ and } 1) \rightarrow A^2\Pi_{1/2}(v', J' = 1/2)$ and $X^2\Sigma^+(v'', N'' = 1, J'' = 3/2, F'' = 1 \text{ and } 2) \rightarrow A^2\Pi_{1/2}(v', J' = 1/2)$ will together be denoted by $\mathrm{X}_{v'',1} - \mathrm{A}_{0,1/2}\,\mathrm{P}(1)$.

2.4 Dark States

An additional complication in our cooling scheme is the presence of dark Zeeman sublevels. Due to the Zeeman sublevel structure of quantum states, electric dipole transitions between quantum states where at least one of the states has an angular momentum $J \geq 1$ is likely to create dark states.

We define a dark state $|NC\rangle$ when $\langle NC| - e\vec{r} \cdot \vec{R}\,|f\rangle = 0$. Once a molecule decays into a dark state, it is lost from the quasi-closed cycling transitions.

Experimentally, we use a linear polarized laser that addresses pure $\Delta m = 0$ transitions, where m is the magnetic quantum number. The dark state can be easily understood due to obvious selection rules. For example, driving the $|F, m_F\rangle = |2, m_F\rangle \rightarrow |1, m_F\rangle$ transitions with a linearly polarized laser will induce two dark states $|2, 2\rangle$ and $|2, -2\rangle$.

Furthermore, less obvious dark states are present when driving, for example, the $|1, m_F\rangle \rightarrow |1, m_F\rangle$ transition with light that is sigma-polarized in both orientations, where the coherent superposition

$$|NC\rangle = \frac{|1, 1\rangle + |1, -1\rangle}{\sqrt{2}} \tag{2.15}$$

is a dark state.

SrF has a large ground state magnetic moment of μ_B, which means that the dark states can be directly remixed by applying a B-field. This technique is discussed in [52], using density matrix methods in atomic systems. The direction and magnitude of the B-field must be controlled in order to keep the molecules in the quasi-closed cooling cycle. To ensure that transitions are excited from a superposition of all Zeeman sublevels, the B-field must have some component in the direction of laser polarization as well as some component perpendicular to this. Regarding the magnitude of the B-field, there is a trade-off. A B-field that is too large will cause Zeeman-shifts that will force the transitions out of resonance, resulting in a slower cooling rate. A B-field that is too small will result in an induced precession that is slower than the Rabi frequency of the optical transition. Simulations using rate equations, which we discuss in further detail in section 4.1.2, show us that B-fields of magnitude 2 G is suitable.

2.5 Practical Requirements for Laser Cooling SrF

2.5.1 Longitudinal Slowing

Using the properties of SrF described in this chapter so far, we can see how effective laser cooling SrF is by estimating the distance over which a beam of molecules needs to be Doppler cooled to bring a significant fraction of the beam to a halt. We assume that the molecular beam comes from a supersonic source. The number of absorption events required to bring one molecule to a halt is given by

$$n = \frac{Mv\lambda}{h}, \tag{2.16}$$

where M is the molecular mass of SrF, v the velocity of the molecules leaving the source and λ the wavelength of the cooling laser. We take $m = 100$ amu, the typical value of $v = 600$m/s and $\lambda = 663$nm. These parameters lead to $n = 10,000$.

The probability that the molecule decays to a state outside the cooling cycle with repumping from $X(v = 1)$ is

$$p = 1 - f_{00} - f_{01} \tag{2.17}$$

where f_{00} and f_{01} are Franck-Condon factors. The fraction of molecules that remain in the cooling cycle after n scattering events is

$$P = (1-p)^n. \tag{2.18}$$

For $p = 4 \times 10^{-4}$, we obtain $P = 30\%$.

Finally, if the lifetime of the excited state is τ, the distance the beam travels before being stopped, assuming uniform deceleration and a two-level system, is

$$L = v\tau n. \tag{2.19}$$

We have optimistically assumed a two-level system with the maximum scattering rate of $1/2\tau$. Taking $\tau = 24\,\text{ns}$, gives $L = 14\,\text{cm}$. In this way, we have obtained the crude estimate that a 30% of a beam of SrF with repump from one vibrational level can be bought to a halt in 14 cm.

2.5.2 Transverse Beam Brightening

In transverse beam brightening, molecular beam travelling in the longitudinal direction, which spreads out in the transverse direction as it propagates, is collimated in the transverse direction using an optical molasses.

To gain a crude estimate of the practical requirements for beam brightening with a 1D transverse optical molasses setup, we use the familiar expression of the force on a two-level atomic system. We assume that the force on a molecule in an optical molasses is

$$F(v) = \frac{\hbar k}{2}\left(\frac{s\delta}{1+s+4\left(\frac{\delta+kv}{\Gamma}\right)^2}\right) - \frac{\hbar k}{2}\left(\frac{s\delta}{1+s+4\left(\frac{\delta-kv}{\Gamma}\right)^2}\right), \tag{2.20}$$

where $s = I/I_{\text{sat}}$, $\delta = \Gamma/2$, where $1/\Gamma$ is the lifetime, $k = 2\pi/\lambda$ is the transition wavenumber, and v is the transverse velocity of the molecule. Substituting $s = 1$, $\Gamma = 2\pi \times 7\,\text{MHz}$ and $v = 1\,\text{m/s}$ gives $|F| \simeq 10^{-21}\,\text{N}$. Now, the power acting on the molecule is

$$P = Fv \simeq 10^{-21}\,\text{J.s}. \tag{2.21}$$

If the transverse temperature of the molecular beam is approximately 1 K, then the transverse energy is 7×10^{-24} J. This gives an interaction time of

$$t_{\text{int}} = \frac{E}{P} \simeq 1\,\text{ms}. \tag{2.22}$$

This means that a molecular beam with transverse temperature of 1 K can be collimated in 1 ms, i.e., in the case of a supersonic molecular beam with an argon carrier propagating at 600 m/s in the longitudinal direction, an interaction length of 60 cm.

To reiterate, the figures calculated in this section are crude estimates. In particular, the scattering rate used is wrong by a factor of 7. This is because there are 28 hyperfine levels in the quasi-closed cooling cycle, not just two levels. This issue will be discussed further in section 3.7.2 and will be taken into account when more sophisticated models are introduced in chapter 4.

Chapter 3

Experiment

3.1 Overview

A schematic diagram of the experimental apparatus is shown in figure 3.1. Within the apparatus, pulses of SrF molecules are produced and emitted by the supersonic source using laser ablation. The molecules then pass through a cooling beam and a repump beam, which makes them undergo quasi-closed cycling transitions. As a result, the molecular beam is collimated by the cooling beam. Additionally, there is a B-field in the cooling region that destabilizes the dark states. After leaving the cooling region, the molecules pass through a detector, which measures

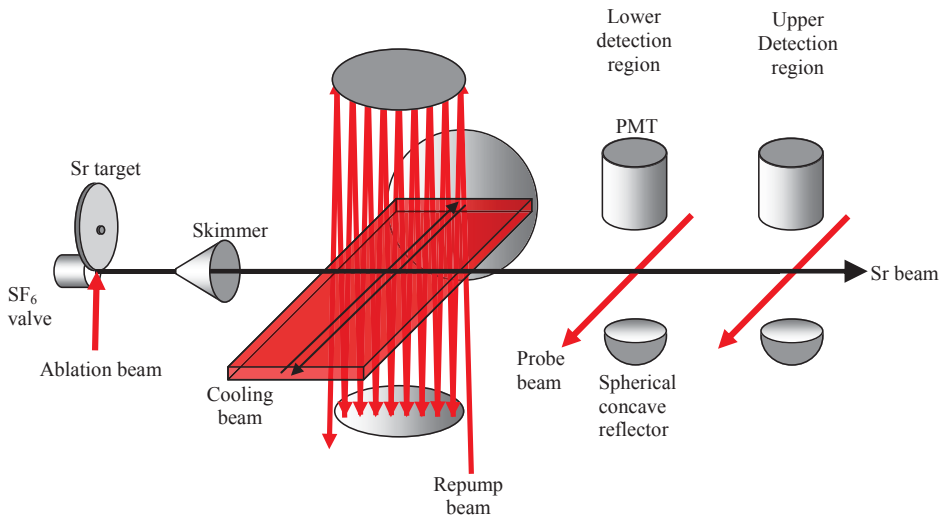

FIGURE 3.1: Overview of experiment

the number of photons emitted in the laser-induced fluorescence of the molecules, using a resonant probe laser. The molecules are either detected here or at a second detector, which has the same configuration as the first, but is further away from the source. When the molecular beam is focused, the number of molecules at the second detector increases relative to the number of molecules at the first detector, compared to when the cooling beam is off. Therefore, we measure the cooling effect by comparing the number of molecules detected in the two detection regions.

Each component of the experiment (the vacuum chamber, supersonic source, cooling and repump laser system, magnetic field coils, detection system, and the software and hardware that control the experiment) are described in more detail in the following sections.

3.2 Vacuum Chamber

Figure 3.2 shows the vacuum chamber where the experiments take place. The vacuum chamber consists of two parts: the source chamber and the main chamber, separated by a skimmer of diameter 2 mm. The interior is kept under vacuum by a roughing line and two turbomolecular pumps, one mounted on the source chamber and one mounted on the main chamber. The pump speeds of the upper turbo pump and the lower turbo pump are 360 liters/s and 1050 liters/s respectively. The values of pressure in each of these parts are monitored by Penning gauges, and both are usually between 1 and 3×10^{-7} Torr. The rough vacuum pressure is monitored by a Pirani gauge. We can run molecular beam experiments at any pressure below 10^{-6} Torr, for example when pumping down after breaking vacuum, without noticeable deterioration in molecular flux resulting from state-changing collisions. There is an inlet valve at the top of the chamber, which is connected to a bottle of Ar gas, slightly higher than 1 atm, for back filling. There are light baffles positioned in various parts of the chamber to minimise background scatter of laser light and room light. These are designed to block light without affecting the pumping speeds.

3.3 Supersonic Source

We use a pulsed supersonic source with a design that is widely used in our research group [53]. It is the source of choice for this experiment as it can produce a stable, high flux of SrF molecules in their ground state at low vibrational temperatures.

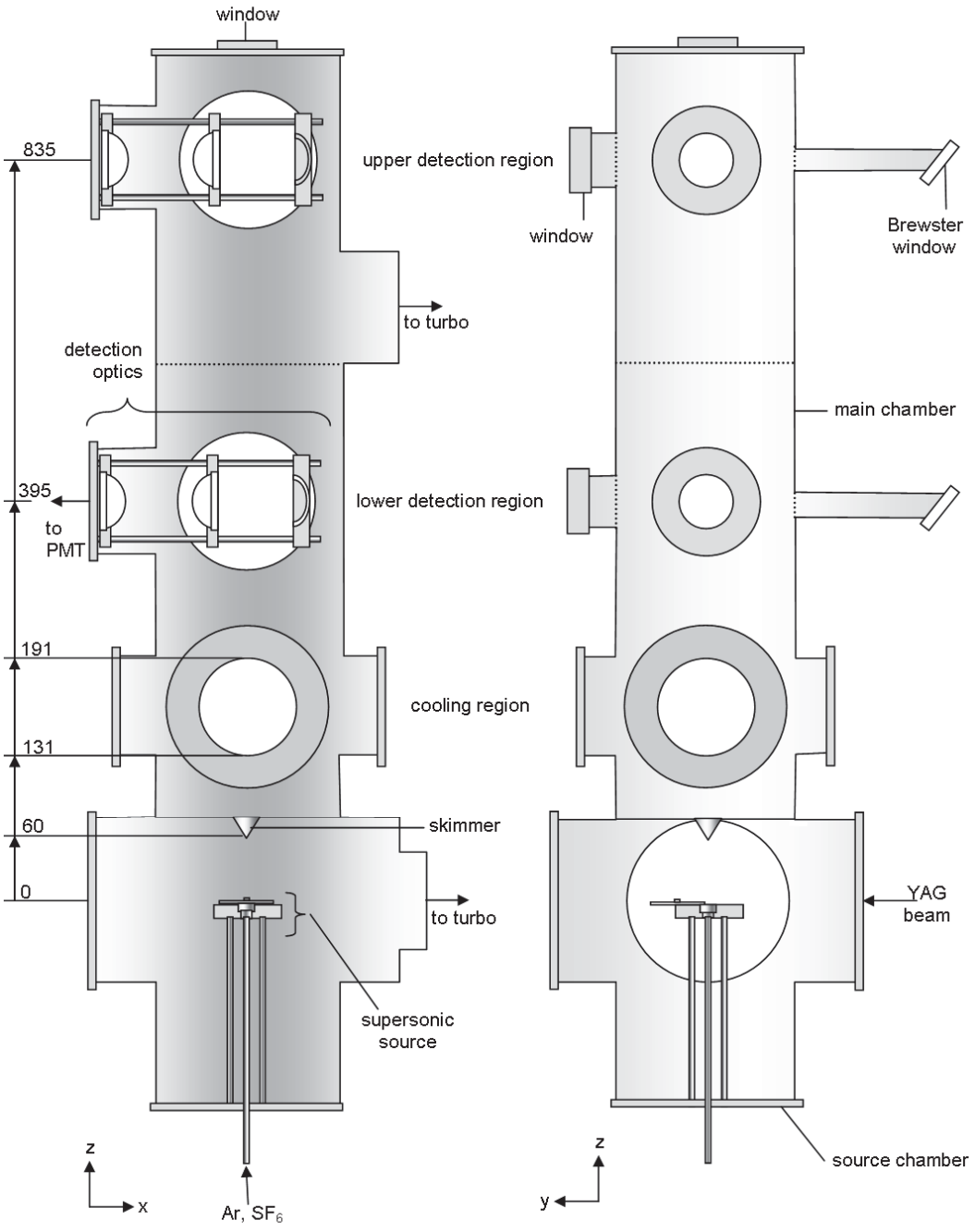

FIGURE 3.2: Schematic diagram of the vacuum chamber. The dimensions are in mm.

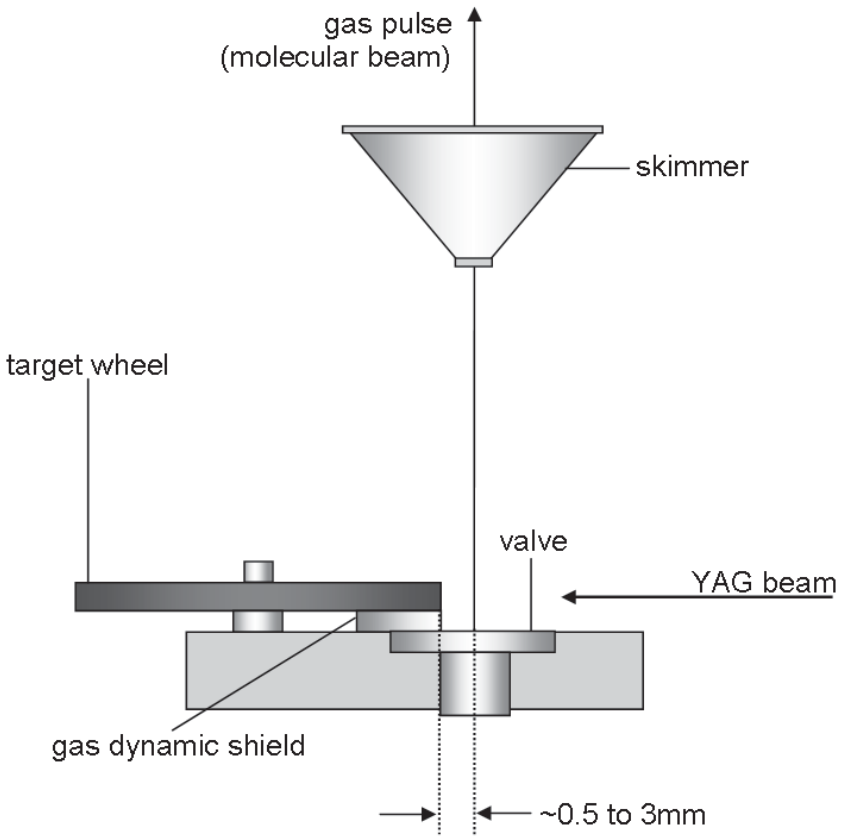

FIGURE 3.3: The main parts of the supersonic source

The molecular beam pulse leaving the skimmer is well-collimated, with a maximum transverse velocity of 10m/s. The skimmer is funnel shaped to divert the shock wave away from the path of the molecular beam. The narrow velocity spread of the molecular pulse makes it particularly suitable for transverse cooling. It has a narrow velocity spread in the forward direction too. This means that it is also convenient for longitudinal cooling.

The speed distribution of a supersonic beam with central longitudinal speed v_0 can be modelled by a Gaussian distribution [53]. In this distribution, the molecular flux in the longitudinal speed range v to $v + dv$ can be written as

$$f(v)\,dv \propto \exp\left[\frac{-M(v-v_0)^2}{2k_BT}\right]\,dv, \tag{3.1}$$

where M is the molecular mass, k_B is the Boltzmann constant and T is the longitudinal translational temperature.

The supersonic source produces pulses of SrF molecules in Ar carrier gas with a longitudinal translational temperature of 6 K propagating with a mean velocity of 610 m/s with a molecular flux of the order of 10^9 molecules per steradian per pulse.

The supersonic beam has no well-defined transverse temperature. This is because the transverse velocity is dominated by the longitudinal velocity in the geometry of the skimmer. The angle subtended by the skimmer is very small (1/60 radians) so it is filled evenly by molecules. Every angle up to the maximum angle allowed by the skimmer is equally probable. This gives rise to a velocity distribution that increases linearly with radial distance from the beam centre. This distribution is nothing like a Boltzmann distribution so we cannot assign a transverse temperature.

The constituent parts of the supersonic source are shown in figure 3.3. A mixture of SF_6 (2%) and Ar (98%) carrier gas at 4 atm is pulsed out as the solenoid valve (Parker VAC-750 PSIG) is opened with high voltage pulses, typically of duration 225 μs and amplitude 150 V at 10 Hz, from a homemade voltage driver. The gas expands isentropically as it enters the vacuum chamber and its enthalpy is converted into kinetic energy, so its translational and internal temperature decreases but mean velocity increases. While the source is running, the pressure inside the source chamber is $(2.0 \pm 0.5) \times 10^{-4}$ Torr. A pulsed 50 mJ Nd:YAG laser (Quantel Ultra) with pulse duration 10 ns at 10 Hz, ablates a solid Sr target while the gas pulse passes over it. The target is an aluminum wheel with 3 mm wide Sr strips glued onto the rim. The timings of the flashlamp to the Q-switch and the valve opening to the Q-switch are typically 730 μs and 630 μs respectively. During the supersonic expansion, the ablated Sr atoms react with the SF_6 (2%) gas to form SrF radicals, along with other products. The hot SrF radicals thermalize by collisions with the carrier gas, which reduces their rotational, translational and vibrational temperature, while increasing their mean velocity. Then, a 2 mm diameter skimmer selects the axial part of the beam at 60 mm away from the source.

We empirically optimize the SrF beam intensity during the experiments, and on longer timescales. The SrF beam intensity is very sensitive to the condition of the Sr target surface. A fresh, clean, metallic surface gives the strongest molecular signal. However, as a particular part of the target is subjected to many and/or powerful ablation shots from the YAG laser, it degrades and turns black. During experiments, we rotate the target using a rotary feedthrough and adjust the position of the YAG spot using the mirror to optimize the molecular beam flux. Between

several experiments, we scan each of the time interval between the flashlamp and the Q-switch, the time interval between the valve opening and the Q-switch and the duration YAG laser when the valve is open by computer control while detecting the molecular signal in order to find the respective optimal values. However, we found that if the time interval between the flashlamp and the Q-switch is less than 720 μs, the YAG power is too high and the target degrades rapidly. We can determine by visual inspection when the YAG power is too high. The point on the target that is hit by the YAG flashes bright, white at high powers. At moderate powers that preserve the target, but still yield a good SrF beam intensity, we can see a faint orange plume. Increasing the voltage of the pulse that opens the valve has the same effect as increasing the length of time that the valve is open up to a certain extent, but at high voltages the valve can bounce and opens again to create a second pulse immediately after the first.

The signal also suffers when the Sr is exposed to air. It corrodes and gets covered in a thin layer of deposit. This is not usually a problem unless the vacuum in the chamber is broken, and can be remedied by taking the target out of the chamber and scraping off the deposit with fine sandpaper if the exposure time to air is less than a few hours. If we know that the vacuum is going to be broken for around an hour or more, we remove the target from the chamber, cover the Sr surface in oil and wrap in foil. If severe corrosion takes place due to prolonged exposure to air and most of the Sr turns white, new Sr needs to be applied as the target can no longer be used.

The relative positions of the target wheel, valve and skimmer can be altered in extreme cases, when the apparatus configuration has been disturbed, and no other measures can be taken to yield a molecular signal. We found that it is important that the target is set back from the axis of the valve nozzle by at least 0.5mm otherwise the flow of gas is obstructed.

3.4 Cooling and Repump Laser System

The cooling and repump laser and the optical setup is designed to generate a cooling laser beam consisting of four frequency components and a repump laser beam consisting of another four frequency components, with each component having at least an intensity of I_{sat} for the hyperfine transitions that it addresses. The cooling and repump laser systems are shown in figure 3.4. Both cooling and repump laser frequencies originate from homemade extended cavity diode lasers (ECDLs) and

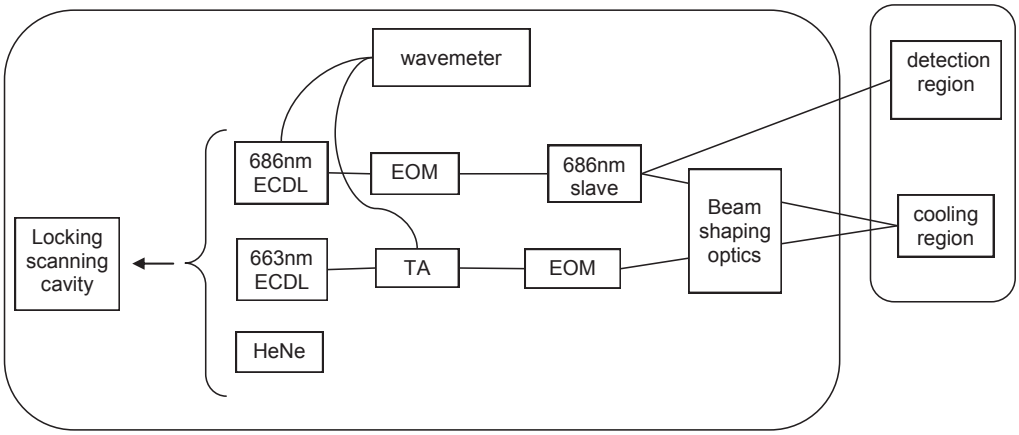

FIGURE 3.4: A flowchart showing the laser system in the experiment.

are modulated by homemade electo-optic modulators (EOMs). The cooling beam is amplified using at tapered amplifier, and the repump beam is amplified by injection locking to a slave diode laser with a higher power output than the ECDL. Both amplified beams are shaped to maximize the interaction length with the molecular beam.

Both the cooling and repump frequencies are generated by homemade ECDLs. Each ECDL has the design described in [54]. The grating is in a Littrow configuration. The diode has its AR coated window removed with a laser diode can opener. It is powered by a current controller from Thorlabs. To tune an ECDL, we tune the frequency coarsely at first by adjusting the grating tilt and cavity length using the kinematic grating mount. Then we adjust and stabilize the temperature of the diode by feeding back the voltage signal from a thermistor, through a thermoelectric controller, to a peltier plate that is placed in thermal contact underneath the diode mount. The sensitivity of laser frequency to current and temperature is around -3.5 kHz/mA and -32 MHz/^{o}C respectively. The nominal frequencies and powers, diode models, and the normal operating current and temperatures for each diode are indicated in table 3.1.

We monitor the frequencies of the lasers using the High Finesse WS6 compact wave meter (accuracy 600 MHz), which monitors all laser frequencies using a switch box.

Once tuned, the ECDL frequencies are locked to a temperature stabilized HeNe reference using a system that will be described in more detail in section 3.4.2. There is a 40 dB optical isolator at the output of the ECDL to reduce the optical feedback that causes the laser frequency to jitter.

	cooling laser	repump laser
diode model	Opnext HL6546MG	Opnext HL6738MG
nominal wavelength	660 nm	690 nm
nominal output power	120 mW	10 mW
normal operating current	145 mA	100 mA
normal operating temperature	20^{o}C	18^{o}C

TABLE 3.1: Relevant specifications and operating conditions of the ECDLs

The cooling ECDL beam is then amplified by a 300 mW output tapered amplifier (Toptica BoosTA). The amplified cooling laser beam from the tapered amplifier output is then modulated by an EOM to give four frequency components of roughly equal amplitudes.

The shape of the cooling laser beam at the output of the tapered amplifier is circular, with diameter 0.5 mm. This is shaped into a rectangle of 60 mm by 5 mm and we direct it onto the SrF beam such that the longer side of the beam is aligned with the direction of the SrF beam, and the shorter side is centered on the SrF beam. The cooling beam is retroreflected by a mirror with 99% reflectivity inside the chamber.

The output of the repump ECDL is modulated by an EOM to give four frequency components of roughly equal amplitudes before being injected into a slave laser. The EOM modulation scheme is described in more detail in section 3.4.1.

The repump ECDL power is amplified by injection locking [55]. The repump ECDL beam is used to seed a 50 mW Opnext HL6750MG slave diode laser with the window removed, cooled to -5^{o}C, by injecting 2 mW into the ejection port of an optical isolator at the slave laser output. The free-running wavelength of the nominal 686 nm diode turned out to be around 690 nm. The diode is cooled as the injection lock does not work unless the free-running wavelength of the laser matches the seed wavelength.

We shape the output beam of the slave laser into a rectangle of 5 mm by 2 mm and direct it to intersect the SrF beam approximately 24 times by aligning it at a slight angle onto a pair of mirrors facing each other, on either side of the SrF beam. One mirror is outside the vacuum chamber and the other is inside.

We compare the laser-induced fluorescence signals that are detected with and without the cooling beams to observe the effect of cooling. The cooling beam

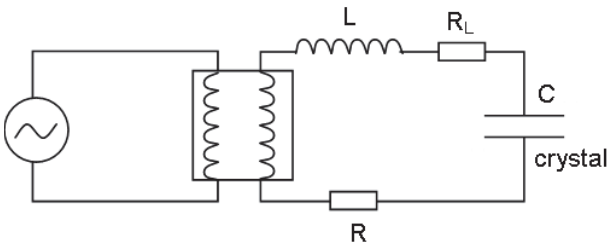

FIGURE 3.5: Schematic of the resonant EOM tank circuit.

can be blocked with a mechanical shutter, which is positioned after the tapered amplifier. The shutter operation is described in more detail in section 3.10. There is a photodiode positioned to detect the light on the other side of this shutter to generate a signal to determine whether this shutter is open or not. In all experiments where this shutter is used, it opens and closes at half of the frequency of another shutter, on one of the probe laser beams. The reason for this is explained in the description of the data acquisition sequence in section 3.10. Due to the limited number of output channels available, we choose to connect the input signal of the probe beam shutter to the cooling beam shutter via a Schmitt trigger, to eliminate voltage spikes followed by a flip-flop circuit, which halves the signal frequency. We monitor whether this shutter is open or not with the photodiode as the flip-flop circuit occasionally fails to switch.

3.4.1 Electro-optic Modulator

A resonant EOM circuit (figure 3.5) is used to generate sidebands on incoming laser light by phase modulation. The EOM offers enough modulation depth to almost completely deplete the carrier frequency, while roughly equal powers are distributed between the first- and second order sidebands. This is shown in figure 3.6. In this experiment, the EOM is driven by a 42.75 MHz amplified rf signal. The power of the rf signal input into the EOM is approximately 1 W.

In a resonant EOM circuit, an rf electric field is applied across the EOM crystal in a direction perpendicular to the propagation direction of the laser beam $\vec{k}$. The laser light experiences a change in refractive index with the application of the electric field and the light's phase changes. The crystal has capacitance, and is placed in series with an inductor to form an LC circuit that is resonant with the driving frequency. This way, less rf input voltage is required. A transformer at the input matches the impedance of the 50 Ω source to the LC circuit. Additional

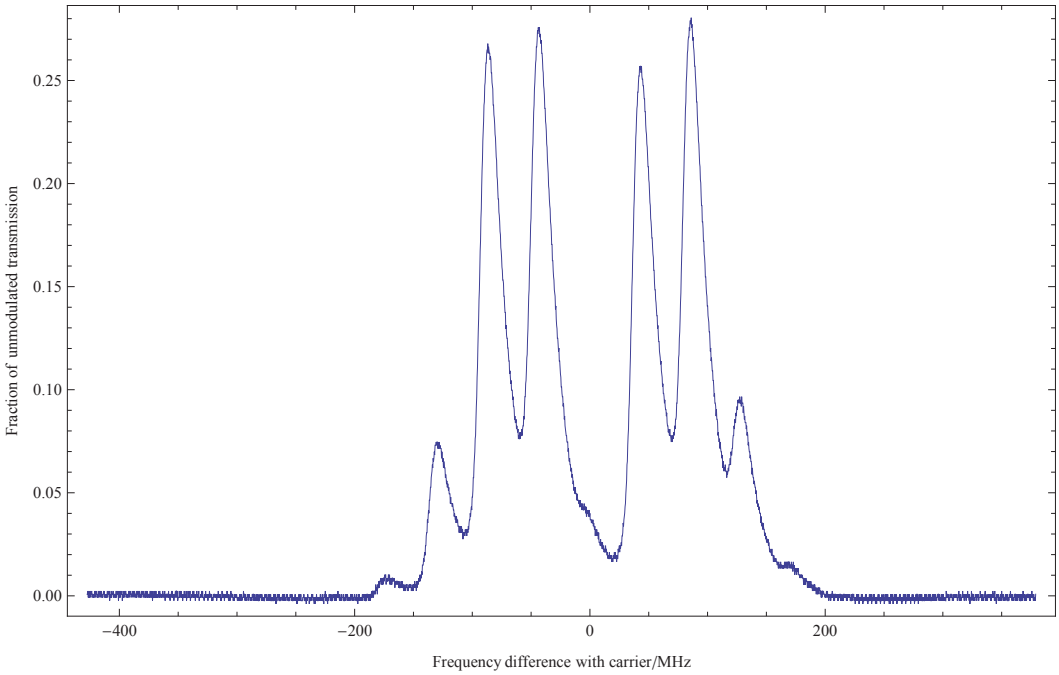

FIGURE 3.6: Transmission through scanning Fabry-Perot cavity for EOM modulated beam

resistors may be needed to match the impedance and reduce reflected power, as the impedance ratios of commercial transformers are fixed.

We use the Almaz optics 3.0× 3.0×40.0 mm $LiTaO_3$ crystal with the tank circuit shown in figure 3.5. The crystal has capacitance $C \approx 15\,\text{pF}$, so the appropriate inductance L for the LC circuit to give the required resonant frequency $f = \frac{1}{2\pi\sqrt{LC}}$ is $0.7\,\mu\text{H}$, given by 35 turns on a 1/8" teflon core that is about 2.5 cm long. We measure the impedance R_L at the desired frequency and choose a transformer with an impedance ratio 1:16 such that $16 \times R_L$ is as close as possible to $50\,\Omega$. We added extra resistors such that $16(R_L + R) = 50\,\Omega$ to match the impedance. Furthermore, we altered the length and pitch of the coil, by stretching the coil out, to fine tune the resonant frequency. We checked the impedance with a network analyzer. We found that the impedance of the EOM circuit as seen by the network analyzer changes with cable length due to reflections, however a small deviation from $50\,\Omega$ may be acceptable since the reflection coefficient is $(Z - Z_L)/(Z + Z_L)$, where Z_L is the tank circuit impedance.

3.4.2 Transfer Cavity Lock

The ECDL frequencies suffer from slow drifts of about 5 MHz per hour, but unlike the situation when driving atomic transitions, there are no absolute stable references that are available. Our solution to this problem is a lock system with two stages. In this system, some of the ECDL beam and light from a temperature-stabilized HeNe laser pass through a scanning Fabry-Perot cavity and the transmission is recorded. There is feedback to the ramp voltage driving the scanning cavity so that the transmission peak of the HeNe laser is always at the same position on the voltage ramp. This compensates for any changes in cavity length due to temperature drift. There is also feedback to the piezoelectric transducer that controls the grating angle in the ECDL and therefore the ECDL frequency. This keeps the separation between the HeNe peak and the ECDL peak constant, thus keeping the frequency separation constant. We call this system the transfer cavity lock (also referred to as TCL on occasion). The transfer cavity lock is used to reduce the frequency drift of the locked lasers to less than 5 MHz/day.

A simple calculation shows how important it is to lock the length of the cavity. We calculated the temperature dependence of the frequency of a laser that is locked to a stable reference laser using an invar cavity with no feedback on its length. In our setup, this would be represented by the situation where we are feeding back to the ECDL frequency but not the ramp offset. We use invar in this example as the Thorlabs scanning Fabry-Perot cavity we use is invar. The free spectral range of the cavity is

$$F = \frac{2c}{L}, \tag{3.2}$$

so the change in the free spectral range when the length changes is

$$\delta F = -\frac{2c}{L}\frac{\delta L}{L}. \tag{3.3}$$

Now, for the nth resonant mode, the frequency of a laser input into the cavity is given by

$$\nu_1 = n_1 F, \tag{3.4}$$

where n_1 is the refractive index for that wavelength. So the change in apparent frequency resulting from a change in cavity length is given by

$$\delta\nu_1 = \nu_1 \left(-\frac{\delta L}{L}\right). \tag{3.5}$$

The transfer cavity lock works by providing feedback to maintain a fixed frequency separation between a reference and slave laser. Therefore the relevant quantity is the change in the difference between two frequencies with the change in cavity length, given by

$$\delta\nu_1 - \delta\nu_2 = n_1\delta F = (\nu_1 - \nu_2)\left(-\frac{\delta L}{L}\right) = \nu_1\left(1 - \frac{\nu_2}{\nu_1}\right)\left(-\frac{\delta L}{L}\right). \tag{3.6}$$

For λ_1 =632 nm and λ_2 =663 nm, $1 - \nu_2/\nu_1 \simeq 0.05$. Therefore we have

$$\left|\frac{\delta\nu_1 - \delta\nu_2}{\nu_1}\right| = \left|0.05\left(\frac{\delta L}{L}\right)\right|. \tag{3.7}$$

Substituting $\nu_1 = 5 \times 10^{14}$ Hz, to give a frequency difference change of 5 MHz, we get $\delta L/L = 2 \times 10^{-7}$. The cavity is made of invar which has a coefficient of linear thermal expansion of $\alpha = 2 \times 10^{-6}$ /K. This means that a change in temperature of 0.1 K will shift the frequency of a locked laser by 5 MHz if the slave laser is locked to the reference laser but without the cavity being locked to the reference, using equation 3.7 .

In more detail, the setup of the transfer cavity lock system is as follows and is summarized in figure 3.7. The HeNe laser is temperature stabilized using an electronic circuit and a heater. In the gain curve of the HeNe laser, there are just two cavity modes of perpendicular polarizations, due to the relatively narrow neon bandwidth. These polarization components are separated using a polarizing beam cube and each component is detected on a photodiode. The difference signal is fed back to the heater in order to keep the difference between the intensities of each polarization component constant. The HeNe laser is very sensitive to optical feedback and has an isolator at its output. It is also sensitive to air current so is covered by a cardboard box.

The HeNe laser beam is coupled into a scanning Fabry-Perot cavity, which is scanned using a sawtooth voltage ramp from its control box. The transmission of the scanning Fabry-Perot is measured by a photodiode. This photodiode signal is amplified and passed on to the computer software via data acquisition hardware. The computer software fits a Lorentzian function to the Fabry-Perot transmission peak signal. The computer software feeds back a voltage (V_{offset}) to the offset of the sawtooth voltage ramp through a summing amplifier to ensure that the peak is always positioned at the same point ($V_{1\,\text{set}}$) on the ramp. This means that the length of the cavity at any given point on the ramp is the same, regardless of temperature.

Light from the diode lasers that we wish to lock are also coupled into the same scanning Fabry-Perot cavity. A total of three slave lasers, as well as the master laser, are made to pass through the same scanning cavity by using beam-cubes and dichroic mirrors. The transmission of each beam is selected using a beam cube and detected by its own photodiode then digitised and processed. The software can adjust the slave laser frequencies through sending voltage signals to the piezoelectric transducers in their grating mounts through summing amplifiers. The software keeps the separation between the locked laser peak and the HeNe reference laser peak ($\Delta V_{1\,\mathrm{set}}$) constant by feeding back to the piezo voltage that controls the locked laser frequency.

The error signal when a slave laser is locked for one minute is shown in figure 3.8. The mean error signal is 0.0 MHz and the standard deviation is 1.1 MHz.

3.5 Magnetic Field Coils

In order to destabilize dark states, we mount a pair of Helmholtz coils on the outside of the vacuum chamber, which generate a uniform B-field throughout the region where the cooling laser beam intersects the SrF beam. A 300 μT field is generated by a pair of coils mounted outside the chamber, with the two coils separated by 25 cm. The diameter of each coil is 10 cm and consists of 22 turns of 2.8 mm diameter magnet wire.

3.6 Detection by Laser-Induced Fluorescence

We detect the SrF beam pulse in two regions: at the lower detection region, 395 mm away from the source, and at the upper detection region, 835 mm away from the source. At each probe region a probe laser that is resonant with one of the $X_{v'',1} - A_{0,1/2}\,P(1)$ lines intersects the SrF beam pulse in the transverse direction. The probe laser is a Toptica DL100 Pro tunable diode laser at 663 nm. The SrF molecules are excited, decay rapidly and the resulting fluorescence is imaged onto a PMT photocathode using collection optics. This signal is then amplified and processed on the computer.

After passing through the skimmer, the SrF beam pulse spreads out in the radial direction as it propagates upwards through the vacuum chamber. Just before each

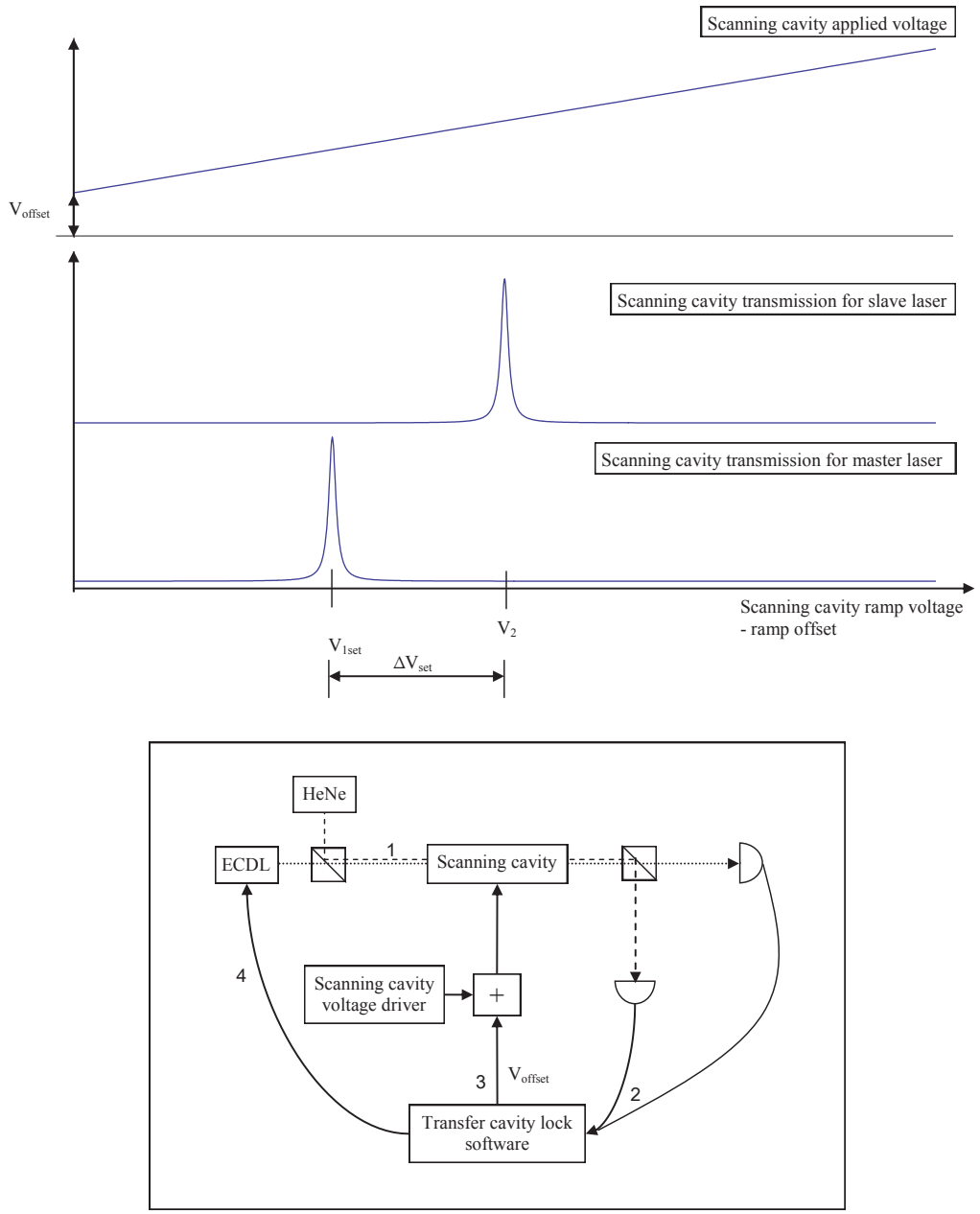

FIGURE 3.7: The input signals to the transfer cavity lock with an overview of the system when one ECDL is locked. 1. The light from the ECDL and reference HeNe laser pass through a scanning cavity at perpendicular polarizations, and the transmission of each is detected by a photodiode. 2. The transmission signal is input to the computer and the computer software fits Lorentzian functions to measure where the peaks lie on the ramp. 3. The transfer cavity lock software outputs an offest voltage on the scanning cavity voltage driver to shift the position of the reference scanning cavity transmission peak to match the setpoint $V_{1\,\mathrm{set}}$. 4. The software then outputs a voltage to change the piezo driver of the ECDL to shift its frequency so that the separation between the scanning cavity transmission peaks of the reference laser and the slave laser are maintained at a fixed separation ΔV_{set}.

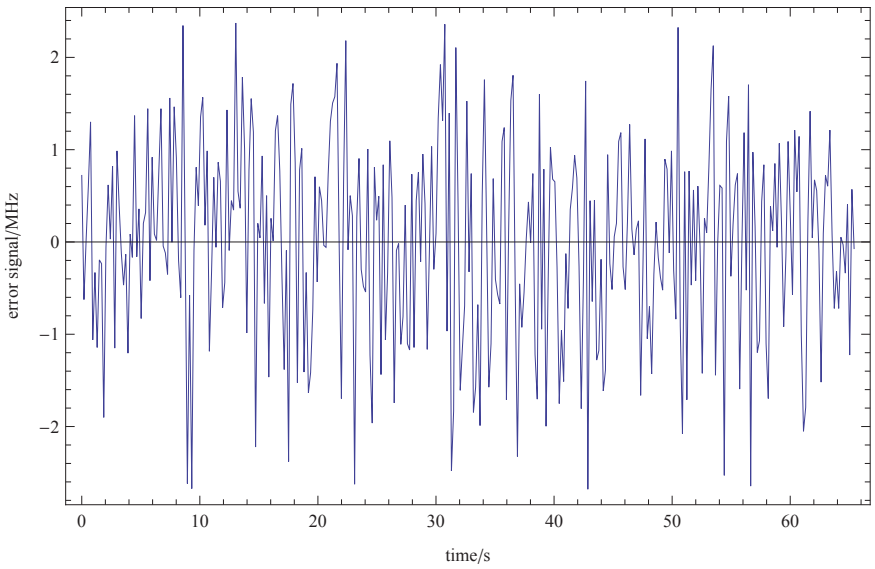

FIGURE 3.8: Error signal between reference laser and locked laser in the transfer cavity lock.

detection region, we physically restrict the size of the molecular beam using an aperture, and shape the probe beam to ensure that all molecules lie within the extent of the probe beam. The aperture is defined by an aluminium sheet with a hole, which is restricted in size using razor blades that are attached to the sheet around the edges of the hole. This sheet is fixed to the framework of the detection optics. The apertures in the lower- and upper detection regions are a 3 mm by 4 mm slit (3 mm in the cooling beam direction) and a 3.5 mm by 11 mm slit (3.5 mm in the cooling beam direction) respectively.

The probe beam is not modulated. It is monochromatic and is resonant with a single SrF hyperfine transition which is usually one of the four $X_{v'',1} - \mathrm{A}_{0,1/2}\,\mathrm{P}(1)$ hyperfine transitions. Photons are emitted by spontaneous emission as the SrF molecules excited by the probe laser decay from the upper state with a lifetime of 24 ns. The number of photons scattered by each molecule depending on the transition and the probe intensity, but as long as these parameters are kept constant, the number of laser-induced fluorescence photons detected from each SrF beam pulse is proportional to the number of molecules in the initial state of the transition.

The probe beam enters the chamber through an AR coated window and exits through a window oriented at the Brewster angle. This window minimizes the reflection of the probe beam back into the chamber. We aim to minimize scatter of the probe beam and any other source of increased background photon counts, which add noise to our detected laser-induced fluorescence signal. There are several

baffles in the passage of the probe beam. Aligning the probe beam well, so that it passes through the center of the input and output windows, also helps to reduce scatter due to clipping of the beam on the baffles.

The photons emitted by the molecules during laser-induced fluorescence are collected by a lens and a spherical concave reflector, placed facing each other such that the detection point lies at the focus of the two (figure 3.10). The aspheric condenser lens is non-AR coated crown glass and has a diameter of 60 mm and focal length of f_L =39 mm, with a transmission of 91% per pass. The spherical concave reflector has diameter 51mm and focal length f_R =17.5 mm. The total solid angle covered by the detection optics is $(0.28 \pm 0.04) \times 4\pi$ steradians. We chose the components to cover a large solid angle but, at the same time, to be positioned far enough from the detection point to avoid collecting scattered light. The collimated beam emerging from the first lens is refocussed using an identical lens onto a PMT (Hamamatsu R5929) with a field stop in the focal plane. The field stop is a piece of card with an aperture, which is mounted on the PMT. It blocks any photons scattered by molecules with transverse velocities that are higher than those we wish to observe, thus preventing excess Doppler broadening. The quantum efficiency of the PMT is 10% at 663 nm.

The PMT's photocurrent is converted to a voltage by an amplifier, and the voltage is then recorded by the computer every 10 μs as the SrF beam pulse travels through the detection region. This data is used to construct a time-of-flight profile of the SrF beam pulse as shown in figure 3.9. The integrated time-of-flight profile with the background signal subtracted is proportional to the number of molecules in the pulse as each molecule scatters the same number of photons for given probe beam intensity. The total detection efficiency is calculated to be $2.3 \pm 0.3\%$ from the theoretical solid angle coverage, measured transmission of the lenses and the nominal PMT efficiency.

When detecting in the upper detection region, we block the probe beam entering the lower probe region with a computer-controlled mechanical shutter in order to prevent the SrF molecules from being pumped out of the lower hyperfine level in the transition that the probe laser is resonant with.

The repump beam, after being modulated by the EOM but before seeding the injection locked slave laser, can also be directed into the upper detection region using a flip mirror. This enables detection on the $X(v = 1)$ to $A(v = 1)$ transitions.

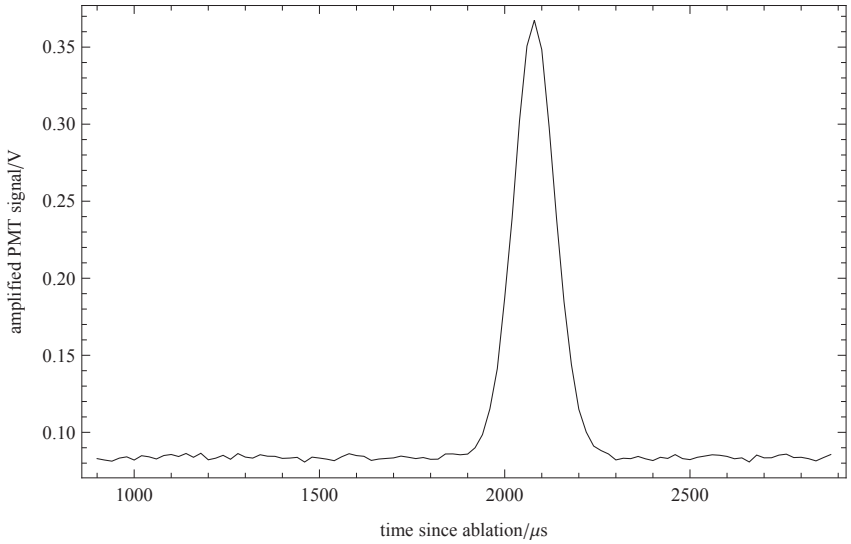

FIGURE 3.9: Time-of-flight profile in the upper detection region

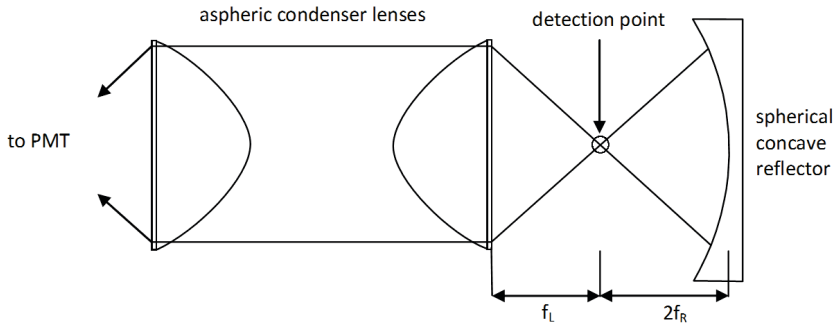

FIGURE 3.10: The layout of the detection optics.

3.7 Spectroscopy and Locking the Laser Frequency

Now I describe the procedure to lock the lasers at the correct frequencies for the laser cooling experiment.

Firstly, we locate the $X_{0,1} - A_{0,1/2}\,P(1)$ transition frequencies. In the main experiment, the probe laser is locked to one of each of these transitions at a time and the cooling laser is locked at a frequency of arbitrary detuning relative to these transition frequencies.

To record the spectrum of the transition that we probe on, first we roughly tune the probe frequency using the wave meter to the nearest $\sim 500\,\mathrm{MHz}$. Then, we lock the frequency to the HeNe reference laser using the transfer cavity lock. We

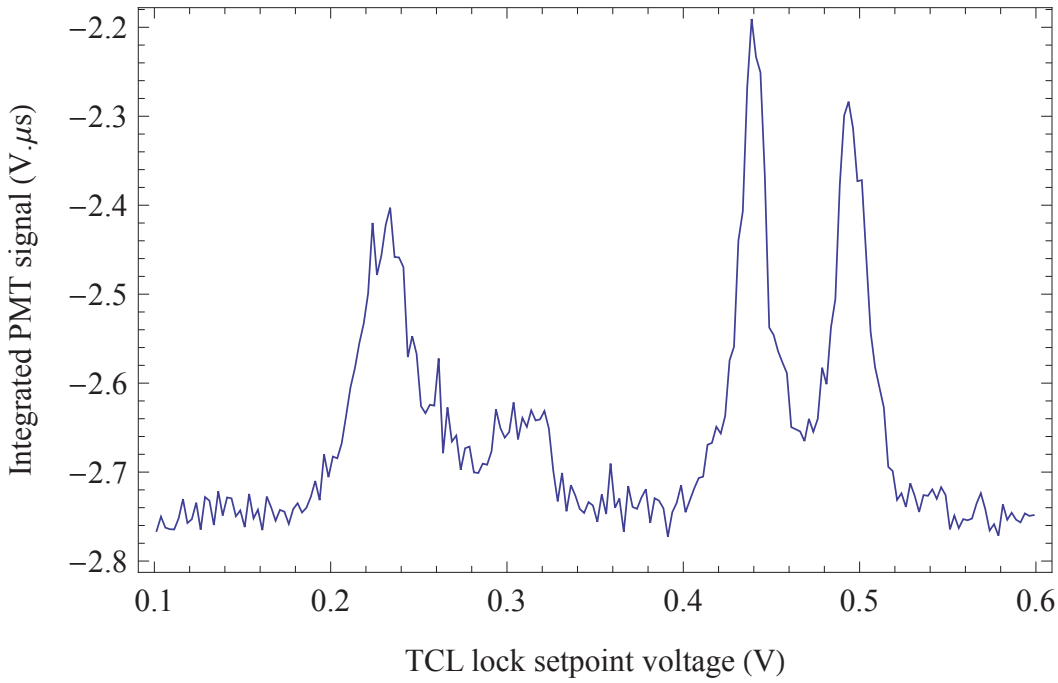

FIGURE 3.11: A laser-induced fluorescence spectrum of the four hyperfine transitions in $X^2\Sigma, v = 0, N = 1 (J, F) = (3/2, 2), (3/2, 1), (1/2, 0)$ and $(1/2, 1)$ to $A^2\Pi, v' = 0, J' = 1/2$ shown from right to left. The spectrum was taken in the lower detection region and consists of 500 data points with 5 shots per data point.

then scan the probe frequency in increments of ~ 1 MHz while we record the laser-induced fluorescence signal from pulses of SrF. Figure 3.11 shows an example of a spectrum. The x-axis shows the set point of the probe laser frequency in terms of the separation between the HeNe peak and the probe laser peak in the scanning cavity transmission vs driving voltage spectrum.

To tune the cooling laser to an arbitrary detuning relative to these transition frequencies, we calculate a voltage to frequency conversion factor f using the relationship

$$f = \frac{171}{V_{(3/2,2)} - V_{(1/2,1)}} \quad [\text{MHz/V}], \tag{3.8}$$

where $V_{(J,F)}$ is the probe laser lock setpoint voltage and the probe laser frequency is resonant with the $X_{0,1} - A_{0,1/2}\, P(1)$ transitions. Note that f depends on the initial cavity length at which the scanning cavity is locked to the HeNe peak using the transfer cavity lock. From section 2.3, we know that the frequency separation between $X^2\Sigma, v = 0, N = 1 (J, F) = (3/2, 2)$ and $(1/2, 1)$ is 171 MHz. We assume that the frequency is linear with this driving voltage in this small interval. Then

we can directly use the voltage values corresponding to the peak values to tune the probe laser frequency to be resonant with the transitions.

The cooling laser is first locked to the HeNe reference in the same way that we lock the probe with the transfer cavity lock. Then we measure the lock voltages of the lowest and highest frequency hyperfine transitions. Then we find the final setpoint voltage:

$$V_{\text{set}} = \frac{1}{2}(V_{(3/2,2)} - V_{(1/2,1)}) + V_{(1/2,1)}. \tag{3.9}$$

Next, we apply the sidebands to the amplified cooling beam so that every hyperfine transition is addressed or is very close to being addressed. Then, we can move the cooling laser lock setpoint to a detuning of ν MHz to the red of the transitions,by changing the lock voltage setpoint to

$$V_{\text{set,det}} = \frac{1}{2}(V_{(3/2,2)} - V_{(1/2,1)}) + V_{(1/2,1)} - f\nu. \tag{3.10}$$

3.7.1 Pumping and Repumping Molecules between the $X^2\Sigma(v = 0)$ Levels and the $X^2\Sigma(v = 1)$ Levels

The next preliminary test is to pump all of the molecules out of the $X^2\Sigma, v = 0$, $N = 1$, $(J, F) = (3/2, 2)$ and $(1/2, 1)$ levels. This is an illuminating experiment that tells us how fast the population is pumped out, and enables us to confirm the photon scattering rate of the transitions from these states to $A^2\Pi$, $v = 0$, $J = 1/2$.

Figure 3.12 shows how the pump laser frequencies overlap with the cooling transition frequencies. The blue line shows the sum of four Lorentzians from a fit to the spectrum of the $\mathrm{X}_{0,1} - \mathrm{A}_{0,1/2}\,\mathrm{P}(1)$ transitions. The red line shows the sum of four Lorentzians of equal heights in the positions given by the EOM modulation frequency, when the detuning of the cooling laser is zero. The amplitudes of the Lorentzians are normalised such that the sum of the amplitudes of each set of Lorentzians is one. It can be seen that the hyperfine transitions with the lowest and highest frequencies are addressed exactly, however there is are offsets in the frequencies of the cooling laser and the transitions for the others.

Once pumped out of the $v = 0$ levels, we can then measure the $X^2\Sigma$, $v = 1$, $N = 1$, $(J, F) = (3/2, 2)$ and $(1/2, 1)$ to $A^2\Pi$, $v = 0$, $J = 1/2$ transition frequencies in terms of the transfer cavity lock setpoint voltage. The final test is to probe the molecules after they have entered the quasi-closed cooling cycle by shining all eight frequencies onto them before probing, and ensuring the population is distributed

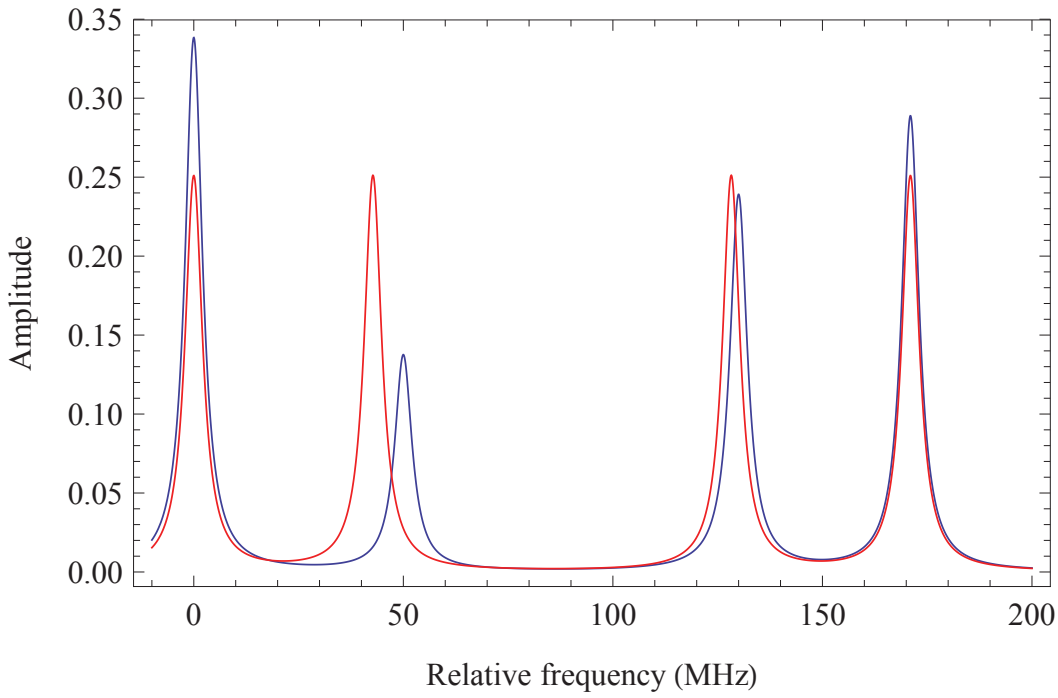

FIGURE 3.12: A plot to show the pump laser frequencies relative to the cooling transition frequencies. The blue line shows the sum of four Lorentzians from a fit to the spectrum of the $X_{0,1} - A_{0,1/2}\,P(1)$ transitions. The red line shows the sum of four Lorentzians of equal heights in the positions given by the EOM modulation frequency, when the detuning of the cooling laser is zero.

among the $X(v = 0)$ and $X(v = 1)$ levels. The proportions of molecules in the $X(v = 0)$ and $X(v = 1)$ levels when we detect them depends on the overlap of the pump and repump beams at the end of the interaction region. We get roughly half of the population in each vibrational level when the pump and repump beams are well overlapped at the end of the interaction region.

3.7.2 Rejection of the $\Gamma/2$ Photon Scattering Rate

In this experiment, the molecules propagate through a transverse beam that is resonant with the $X_{0,1} - A_{0,1/2}\,P(1)$ transitions before they are probed. In the same way as section 3.7, we scan the probe frequency in increments of ~ 1 MHz while we record the laser-induced fluorescence signal from pulses of SrF. If the molecules were a two-level system, the scattering rate is given by $\Gamma/2$, where Γ is the natural lifetime of the upper state. Since the Franck-Condon factor of the $X(v'' = 0)$ to $A(v' = 0)$ transition is 0.982, we expect all of the molecules to be pumped out of the ground hyperfine levels when the interaction length of the cooling laser beam

with the molecules is 1.8 mm, when the intensity of each component of the cooling laser beam is greater than I_{sat} for the respective transitions.

However, even when we subject the molecules to a cooling beam where the intensity of each component is greater than 20 I_{sat} for the respective transitions, not all of the molecules are pumped out even with an interaction length of 10 mm. This indicates that the maximum expected photon scattering rate is not $\frac{1}{2}\Gamma$, as naively expected. We can understand why by noting that the molecule spends an equal amount of time in the 24 X sublevels and the four A sublevels. Spontaneous emission occurs after the molecules spend one lifetime in one of the upper levels, so using this 28-level model, we calculate the correct maximum expected photon scattering rate to be $\frac{1}{2} \times \frac{4}{(4+24)}\Gamma$ [56].

3.7.3 Spectroscopy of the $X(v = 1) - A(v = 0)$ Transition

In order to find the corrrect repump frequency, we use the 686 nm homemade ECDL to probe the molecules on the $X_{1,1} - A_{0,1/2}\,P(1)$ transitions, rather than the 660 nm Toptica DL Pro. Again, we lock the probe laser using the transfer cavity lock and scan the probe frequency in increments of ~ 1 MHz while we record the laser-induced fluorescence signal from pulses of SrF. The molecules propagate through a transverse beam that is resonant with all of the $X_{0\,1} - A_{0\,1/2}\,P(1)$ transitions in a region where there is a magnetic field of magnitude 2 G at 45° to the polarization direction of the cooling laser, before they are probed. The resulting spectrum is shown in figure 3.13.

Now we locate the optimal frequency setpoint of the repump laser in the laser cooling experiment. We do this by repeating the same test of scanning over the $X_{1\,1} - A_{0\,1/2}\,P(1)$ transitions with the modulated repump laser with modulation frequency 42.75 MHz. The modulation by the EOM gives rise to four roughly equal frequency components in the probe laser, each at ± 42.75 MHz and ± 85.5 MHz relative to the carrier frequency. There is also some power in the orders other than the first and second, but these are the strongest, as shown in section 3.4.1. The resulting spectrum is shown in figure 3.14. It can be seen that the most photons are detected from the laser-induced fluorescence from the molecules when the transfer cavity lock setpoint voltage is around 0.1V.

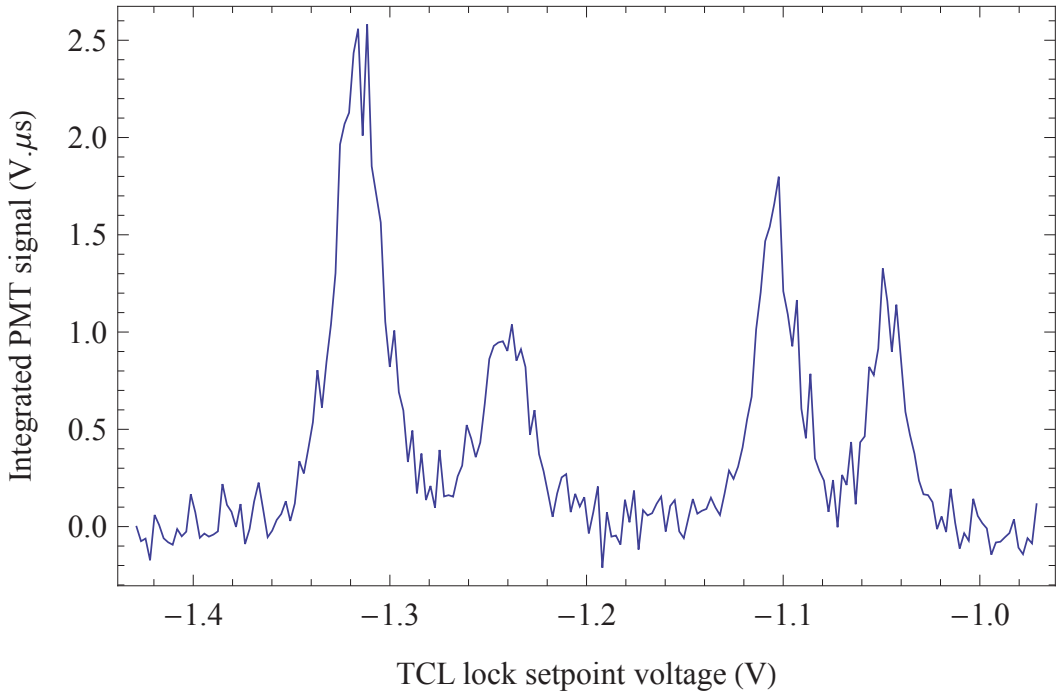

FIGURE 3.13: A laser-induced fluorescence spectrum of the four hyperfine $X_{0,1} - A_{0,1/2}\,P(1)$ transitions taken in the upper detection region. The spectrum consists of 200 data points with 5 shots per data point.

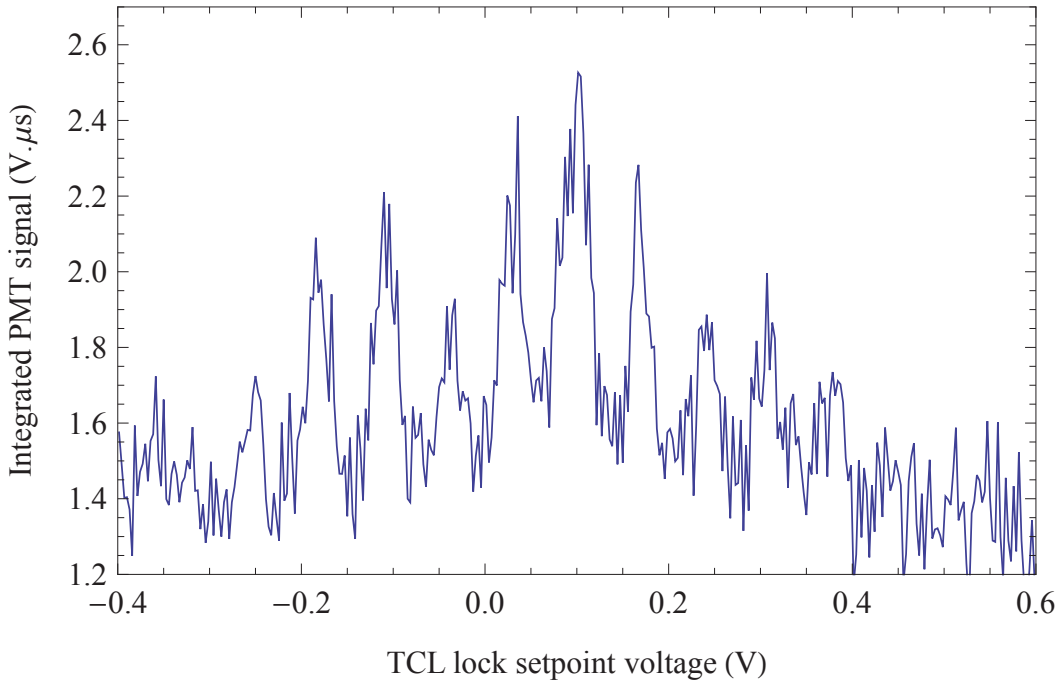

FIGURE 3.14: A laser-induced fluorescence spectrum of $X_{1\,1} - A_{0\,1/2}\,P(1)$ transitions, generated by using the frequency-modulated repump laser to probe. The laser is modulated using an EOM driven at 42.75 MHz, with most of the laser power in the first and second- order sidebands.

3.7.4 Cycling in the Quasi-Closed Cooling Cycle

The final preliminary test is to combine all eight cooling and repump frequencies to shine onto the molecules before detection. By pumping the molecules out of the $X^2\Sigma(v = 0,\, N = 1,\, (J, F) = (3/2, 2)$ and $(1/2, 1))$ levels using the modulated cooling laser, then returning some to the same levels adding the modulated repump laser confirms that the molecules have entered the quasi-closed cooling cycle and are continually scattering photons.

We scan the probe frequency in increments of $\sim 1\,\mathrm{MHz}$ while we record the laser-induced fluorescence signal from pulses of SrF. This is after the molecules pass through a region where they are subjected to a combined beam with all eight transition frequencies for $\mathrm{X}_{0,1} - \mathrm{A}_{0,1/2}\,\mathrm{P}(1)$ and $\mathrm{X}_{1,1} - \mathrm{A}_{0,\,1/2}\,\mathrm{P}(1)$. The resulting spectrum is shown in figure 3.15, together with a spectrum with no cooling for comparison. The spectrum of the cooled molecules is noisier than the spectrum of the uncooled molecules as there is more signal in the uncooled molecules. This is because we probe the molecules in the ground vibrational level only and during cooling, some of the molecules are pumped out of this level and ends up in excited vibrational levels when they are probed.

3.8 The Problem with Counting Molecules

The redistribution of the fraction of the total number of molecules amongst the hyperfine levels due to the cooling and repump beams poses a problem when counting the number of molecules. In conducting the beam brightening experiment, we need to know the change in the number of molecules passing through a fixed cross-sectional area with the cooling and repump beams, compared to without the cooling and repump beams. If we probe on a single hyperfine transition at a single detection region, we are not able to determine whether a change in the laser-induced fluorscence signal is due to the desired cooling effect, or the redistribution of the population of molecules among the hyperfine levels.

Our solution to this problem is to detect the beam at two positions - the lower detection region and the upper detection region. Then we find the ratio of the laser-induced fluoresence signals in the upper and lower detection regions. The change in this ratio does not depend on the redistribution of the molecules among the hyperfine levels. The signal in this experiment, which we will refer to as the

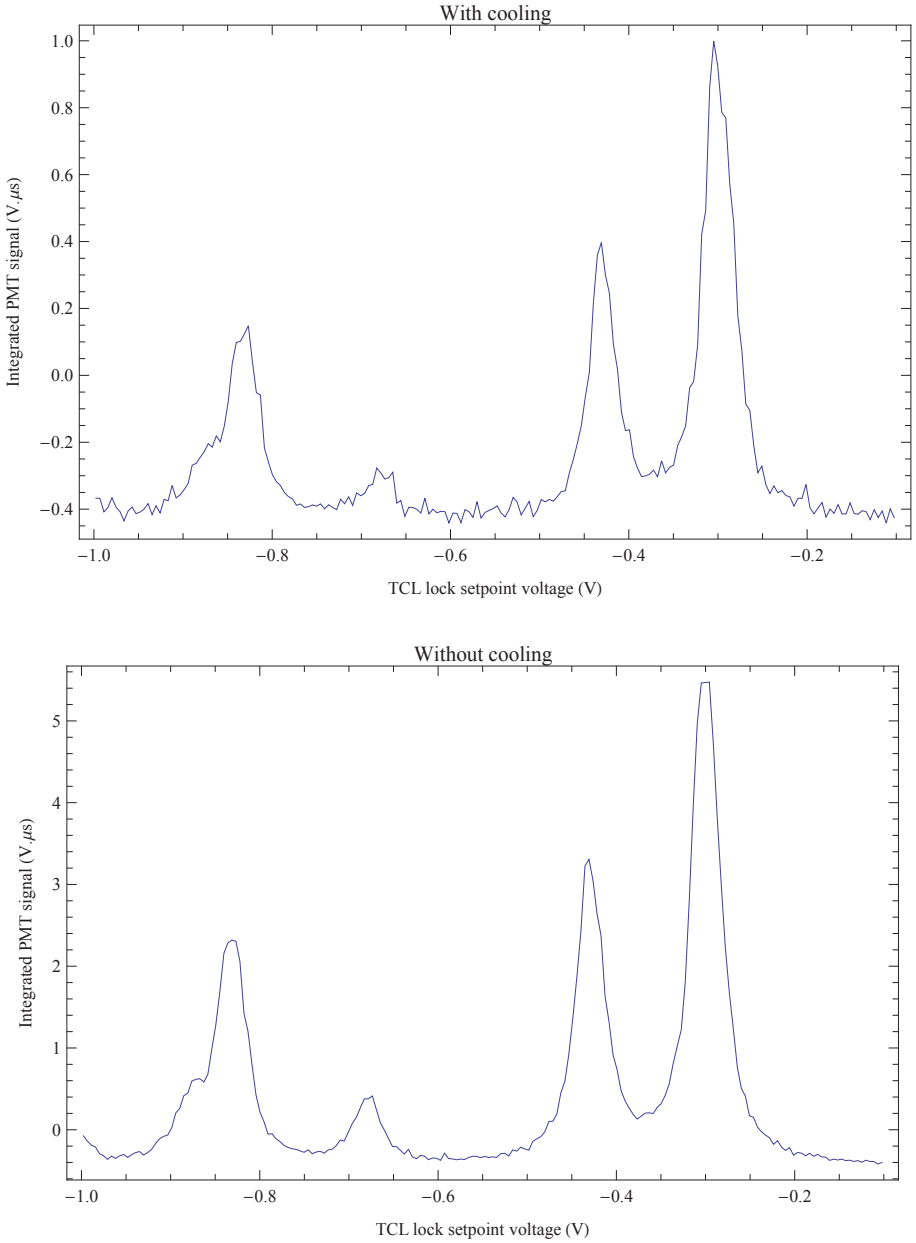

FIGURE 3.15: A laser-induced fluorescence spectrum of the four $X_{0,1} - A_{0,1/2}\,P(1)$ hyperfine transitions taken in the upper detection region after the molecules pass through a region where they are subjected to a combined beam with all eight transition frequencies for $X_{0,1} - A_{0,1/2}\,P(1)$ and $X_{1,1} - A_{0,1/2}\,P(1)$.

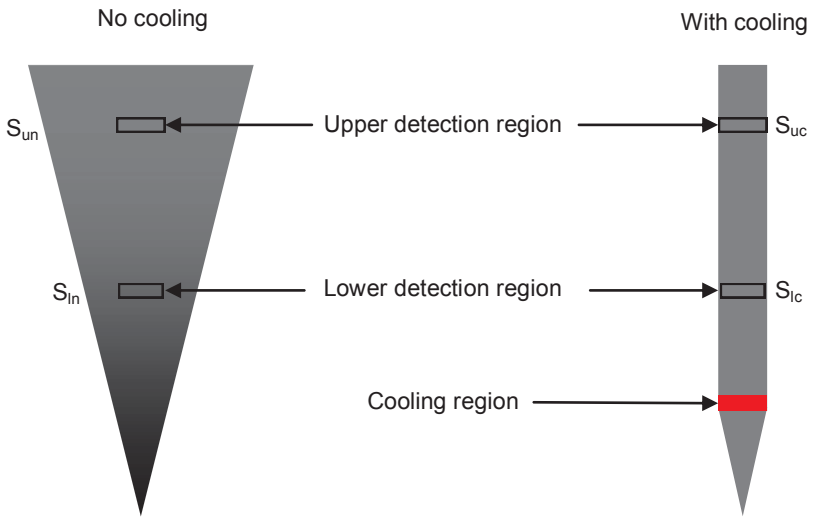

FIGURE 3.16: An illustration to show the problem with counting molecules due to the two contributions of collimation of the molecular beam due to cooling, and the redistribution of the population of molecules due to pumping by the cooling and repump beams. The two effects can be separated by detecting the molecular beam at two points.

"enhancement signal", is,

$$S_{\mathrm{enh}} = \frac{S_{\mathrm{un}}}{S_{\mathrm{ln}}} - \frac{S_{\mathrm{uc}}}{S_{\mathrm{lc}}}, \tag{3.11}$$

where S_{uc} and S_{un} are the integrated time-of-flight profile signals from the laser-induced fluorescence signal in the upper PMT with cooling and no cooling respectively. S_{lc} and S_{ln} are the integrated time-of-flight profile signals from the laser-induced fluorescence signal in the lower PMT with cooling and no cooling respectively.

Figure 3.16 shows how this works. Let us suppose that in this case, the fraction of the total population in the hyperfine state that we probe on decreases due to the pumping effects of the cooling and repump lasers, and that the cooling and repump lasers collimate the molecular beam. The detection regions are all of equal size in the transverse direction, and has the same width in the transverse direction as the collimated molecular beam.

If we detect solely in the upper detection region, although the laser cooling increases the fraction of the molecules in the whole molecular beam passing through the detection region, the total number of molecules is reduced by the hyperfine redistribution effect.

If we also detect at the lower detection region, and take the ratios $S_{\mathrm{uc}}/S_{\mathrm{lc}}$ and $S_{\mathrm{un}}/S_{\mathrm{ln}}$, we see that the cooling increases the ratio of signal in the upper detection region to the lower detection region. This is because $S_{\mathrm{uc}} = S_{\mathrm{lc}}$, as the beam is collimated, but $S_{\mathrm{un}} < S_{\mathrm{ln}}$. This shows that the molecular beam is being focused.

We model the system to find the expected value of the enhancement signal and the signal-to-noise ratio on this value.

3.8.1 Other Potential Methods of Counting Molecules

We have learned that devising a method to reliably count molecules is challenging since the relative populations in each hyperfine level after cooling varies with the detuning of the cooling laser, and when probing, each transition scatters a different number of photons.

Another potential method of detecting and counting the number of molecules is to clean up the molecules from all of the different states into one state, then probing on one state. We have considered adding a clean-up beam addressing three out of the four $\mathrm{X}_{0,1} - \mathrm{A}_{0,1/2}\,\mathrm{P}(1)$ transitions and all of the $\mathrm{X}_{1,1} - \mathrm{A}_{0,1/2}\,\mathrm{P}(1)$ transitions. This would cause all of the population from the X(v=0,1) states to accumulate in one of the $X(v = 0)$ states, which can then be probed, eliminating the aforementioned problems associated with counting the molecules. However, this is not feasible in our current setup as all four frequencies are generated using one EOM. Generating three out of the four frequencies will require another laser.

In another method that is used by DeMille [57], the molecules are collected in the $D(v = 0,\, N = 3,\, J = 5/2)$ state with unresolved hyperfine structure. In this scheme, after cooling but before detection, transverse laser beams address all eight of the $v = 0, 1$ states with resolved spin-rotation structure and hyperfine structure, so that they are pumped into the $A^2\Pi(v = 0,\, J = 1/2)$ level with unresolved hyperfine structure. Next, another transverse laser beam that is resonant with the transition from $A^2\Pi(v = 0,\, J = 1/2)$ to $D(v = 0,\, N = 3,\, J = 5/2)$. The resulting laser-induced fluorescence, predominantly at 360 nm, is filtered and measured by a PMT.

Software	Apparatus	Type
ScanMaster	YAG Q-Switch	Digital output
	YAG flashlamp	Digital output
	Valve	Digital output
	Lower probe laser beam shutter	Digital output
	Lower PMT	Analog input
	Upper PMT	Analog input
	Cooling laser photodiode	Analog input
Transfer Cavity Lock	Locked cooling laser piezo	Analog output
	Locked repump laser piezo	Analog output
	Locked probe laser piezo	Analog output
	Scanning cavity output for cooling laser	Analog input
	Scanning cavity output for repump laser	Analog input
	Scanning cavity output for probelaser	Analog input
	Scanning cavity output for HeNe laser	Analog input
	Scanning cavity driving ramp offset	Analog output

Table 3.2: Summary of DAQ channels for the experiment

3.9 Computer

Voltage signals are input to and output from computer software via the National Instruments PXI data acquisition modules PXI 6229 and PXI 6221. The controlling software are "ScanMaster," which controls the timings of the supersonic source and laser-induced fluorescence detection, and "Transfer Cavity Lock," which controls the transfer cavity lock. All of the PXI inputs and outputs are listed in table 3.2.

3.10 Data Acquisition Sequence

In our laser cooling experiments, the smallest building block of our data sets consists of four shots (SrF molecule pulses). We measure one time of flight profile in each shot: one in the lower detection region with the cooling light on, one in the upper detection region with cooling, one in the lower detection region without cooling, and another in the upper detection region without cooling. Therefore, each shot is

Shot	Useful time-of-flight profile	Probe shutter	Cooling shutter
1	Cooled, lower	Open	Open
2	Not cooled, upper	Closed	Closed
3	Not cooled, lower	Open	Closed
4	Cooled, upper	Closed	Open

TABLE 3.3: Characteristics of each shot in the 4-shot basic data sequence, and the useful time-of-flight data that is collected in each shot

characterized by whether the shutter that blocks the probe beam entering the lower probe region (probe shutter) is open or closed, and whether the shutter that blocks the cooling beam (cooling shutter) is open or closed. The characteristics of each shot is summarized in table 3.3. Recall that, as described in section 3.4, the purpose of the cooling shutter is to generate data sets with and without the cooling light to identify the effect of the cooling light. As described in section 3.6, the purpose of the probe shutter is to block the probe beam in the lower detection region to avoid pumping effects in the molecules when detecting in the upper detection region. Every other parameter is kept the same throughout this sequence. The sequence is then repeated between 100 to 500 times to improve the statistical accuracy of our measurements.

The TTL output signals of the computer are shown in figure 3.17. Before the sequence starts, the probe shutter and cooling shutters are both open. At the start of the sequence, the computer triggers the supersonic source valve, then the ablation YAG laser flashlamp, followed by the Q-switch, to generate the SrF beam pulse for the first shot. After the molecular beam has passed through both detection regions, the TTL line for the probe shutter switches to high, causing this shutter to close. As described in section 3.4, the positive edge of the probe shutter TTL causes the output of the flip-flop circuit, which is connected to the cooling shutter, to switch to high such that the cooling shutter closes. Now the configuration is ready for the second shot, and the valve, flashlamp and Q-switch are triggered again. After the SrF beam pulse passes through both detection regions in the second shot, the TTL line for the probe shutter switches to low, causing this shutter to open again. The third shot is taken in this configuration. Before the fourth shot, both the probe shutter and cooling shutter TTL lines switch, and both shutters close.

Figure 3.18 shows time-of-flight profiles acquired in a single 4-shot acquisition sequence. The shot number corresponds to the experimental configuration indicated in table 3.3. Time-of-flight profiles are recorded at both detection regions regardless

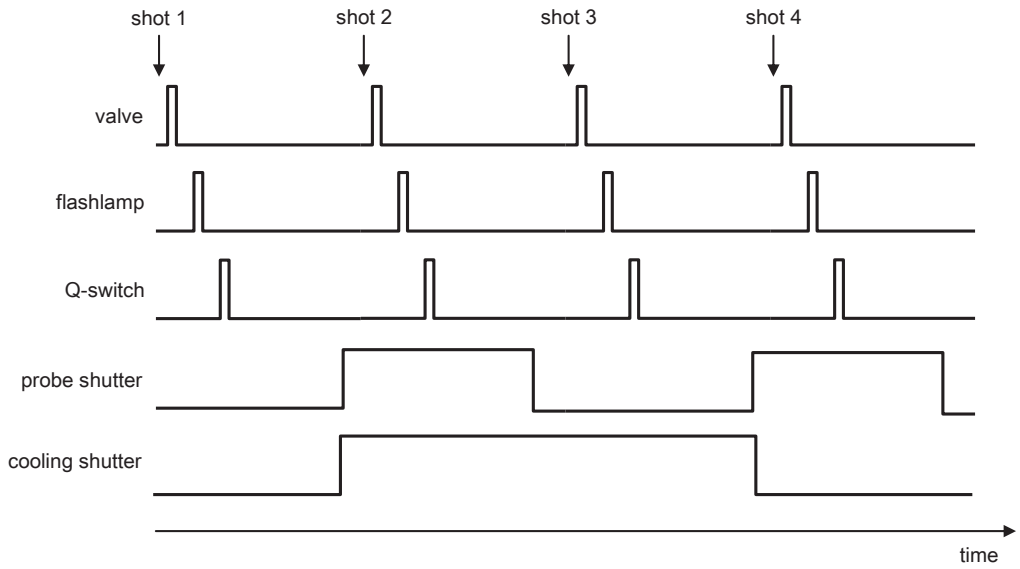

FIGURE 3.17: Schematic showing the TTL output signals in the 4 shot data acquisition sequence

of the configuration. The time-of-flight profiles from the lower detection region when the probe shutter is closed shows no signal as the probe light is blocked, and are discarded. The time-of-flight profiles form the upper detection region when the probe shutter is open shows low signal as the molecules are pumped out from the state that is probed by the lower probe beam, and are also discarded.

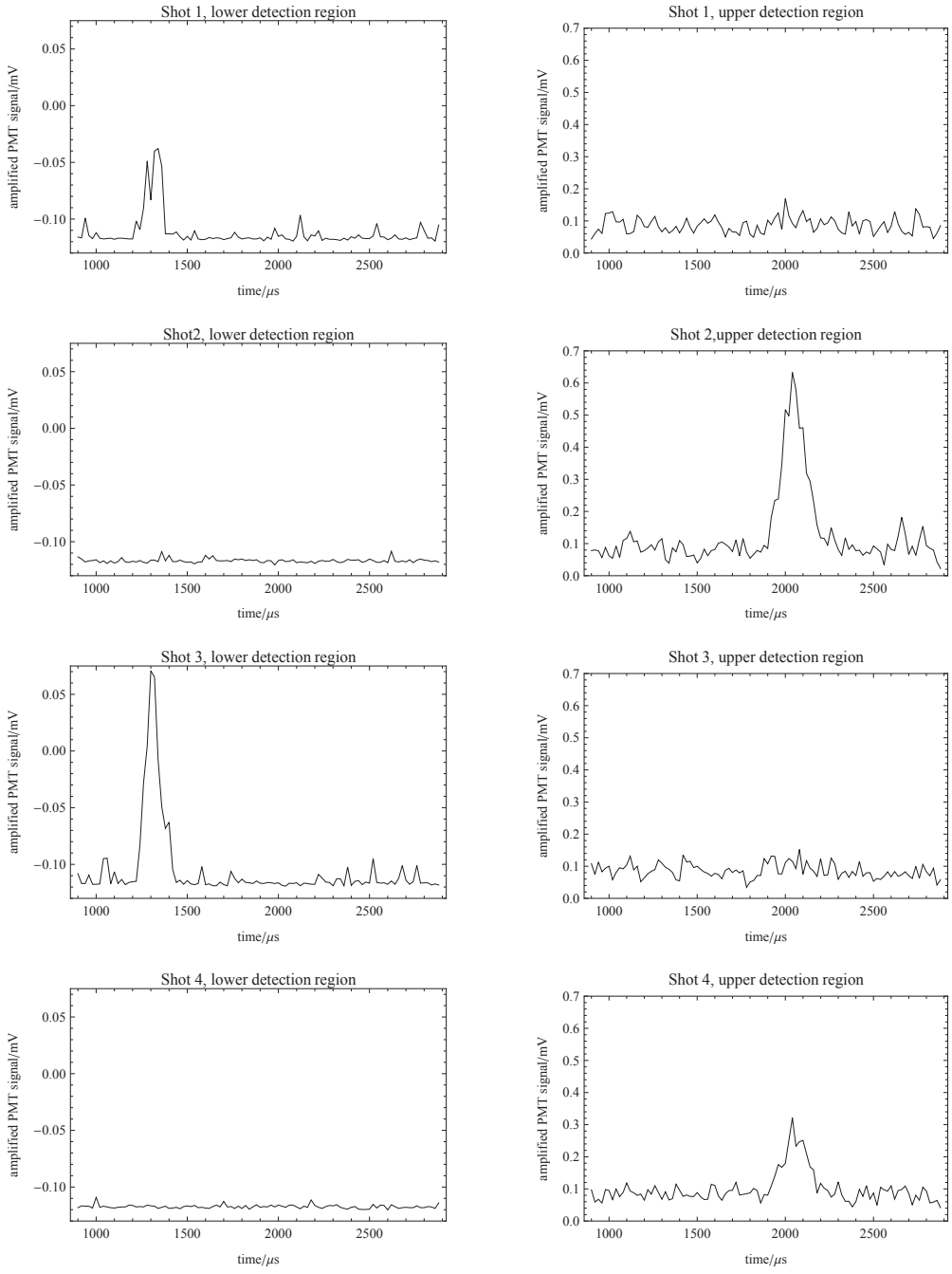

FIGURE 3.18: Time-of-flight profiles acquired in a single 4-shot acquisition sequence. The shot number corresponds to the experimental configuration indicated in table 3.3.

Chapter 4

Modelling

In this chapter, I present simple models of the transverse cooling experiment.

4.1 Modelling with Rate Equations

4.1.1 Setting up the Model

The rate equation model was written by Mike Tarbutt for modelling CaF. I modified the code and ran the simulations with the parameters for the laser cooling SrF experiment.

We solve transition rate equations to model the molecular population dynamics among the levels in our cooling scheme. The model includes the four upper levels and 24 lower levels. The upper levels are all of the M_F states of the $A^2\Pi_{1/2}(\nu = 1/2, J = 1/2, F = 0, 1)$ states. 12 of the lower states are the M_F states in the the ground vibrational level in the ground electronic level, $X^2\Sigma^+(v = 0, N = 0, J = 1/2, F = 0, 1)$ and $X^2\Sigma^+(v = 0, N = 0, J = 3/2, F = 1, 2)$. The other 12 of the lower states are the equivalent states in the first excited vibrational level in the ground electronic level. We assume the $A(v' = 0)$ to $X(v'' = 0)$ Franck-Condon factor to be 0.98, the $A(v' = 0)$ to $X(v'' = 1)$ Franck-Condon factor to be 0.02, and neglect the decays to other vibrational levels. We neglect coherent effects in all of our models as coherent effects take place on timescales that are much shorter than the cooling effects that we are concerned with.

We use the usual laser excitation rate given by the stimulated absorption and emission Einstein coefficients in the case of a monochromatic laser excitation, where

the spectral width is smaller than the spectral width of the Lorentzian transitions, to describe the rate of population change:

$$R(\delta) = \frac{\Gamma}{2}\left(\frac{1}{1+\frac{4}{\Gamma^2}\left(\delta+\frac{2\pi v}{\lambda}\right)^2}\right)\frac{I}{I_s}\times r, \tag{4.1}$$

where Γ is the spontaneous decay rate of the excited state, δ is the laser detuning, v is the velocity of a molecule, λ is the laser wavelength, I is the laser intensity, I_s is the saturation intensity of the transition and r is the branching ratio of the hyperfine transition.

Note that equation 4.1 includes the Doppler shift in the detuning term, and that the branching ratio is r is taken out explicitly, so that the saturation intensity is equal for all transitions. We assume that the laser frequency separations are much greater than the natural linewidth so that each laser only addresses one hyperfine transition, and that all lasers have a similar wavelength for the purpose of the Doppler shift calculation.

We then construct the rate equations accounting for stimulated absorption and emission, spontaneous decay, and the Zeeman sublevels coupling due to the magnetic field, applied with the purpose of remixing dark states. We include the effect of the evolution of the states due to an applied magnetic field, which is a coherent process, in a simple, approximate way. This is by redistributing the population in each magnetic sub-level amongst the other magnetic sub-levels at the Larmor angular precession rate for that state. This yields the following rate equations for each sub-level l in the ground electronic level, whose population change depnds on the populations of the over sublevels l', and each sub-level u in the upper level l. These represent the population change of each sublevel of the electronic ground state and the population change of the first excited electronic state (labelled u) ;

$$\frac{dN_l}{dt} = \sum_u R_{lu}(-N_l + N_u) + \sum_u \Gamma\, r_{lu} N_u + \sum_{l'} \omega_{l,l'}(N_{l'} - N_l) \tag{4.2}$$

$$\frac{dN_u}{dt} = -\Gamma\, N_u + \sum_l R_{lu}(N_l - N_u) \tag{4.3}$$

where N_l is the population in sub-level l, R_{lu} the excitation rate from equation 4.1, r_{lu} the branching ratio from state u to l, and $\omega_{l,l'}$ the Larmor precession rate between states l and l'.

We also ensure that we account for the Zeeman splittings resulting from the applied B-field in the detuning

$$\tilde{\delta} = \delta + g_L \mu_B B_t m_f \tag{4.4}$$

where g_L is the Lande g-factor. The rate equation for the velocity is simply the rate of change of momentum due to the scattered photons, divided by the molecule's mass m. We calculate this for a 1D optical molasses setup where there are two counterpropagating cooling beams of equal intensity, so the rate is $(R_{lu}[-] - R_{lu}[+])$ where $R_{lu}[-]$ and $R_{lu}[+]$ are the rates for each of the counterpropagating beams. Then the rate of change of velocity can be written as

$$\frac{dv}{dt} = \frac{h}{m\lambda} \sum_{l,u} (R_{lu}[-] - R_{lu}[+])(N_l - N_u) \tag{4.5}$$

We numerically solve equations 4.2, 4.3 and 4.5 for the 4 upper levels and the 24 lower levels.

4.1.2 Finding the Optimal B-Field For Cooling

We first use rate equations to find the B-field magnitude in which the molecules scatter photons at the fastest rate. To do this, we solve the rate equations numerically for the case where just the $X(v = 0)$, $N = 1$ levels are pumped on resonance for $10\,\mu$s of interaction time with the laser polarized in the $\hat{z}$ axis and count the number of photons scattered as a function of laser intensity for various B-field magnitudes. The results are shown in figure 4.1.

From the results of the simulation, we conclude that the optimal B-field magnitude is $\sim$2 G, with components in both the z and y directions. As we have discussed in section 2.4, an increase in B-field magnitude results in a faster precession rate for removing molecules from dark states, but also a larger Zeeman shift, which shifts the transition out of resonance and slows down the cycling. Examining the lower plot in figure 4.1, the effect of the increased precession rate is dominant at lower B-field magnitudes, up to $B_y = B_z \simeq 2\,\mathrm{G}$. When the B-field magnitude is increased further, the effect of the Zeeman shift dominates. We will therefore apply a B-field of $B_y = B_z$ in further laser cooling modelling and experimentation to maximize the number of scattered photons.

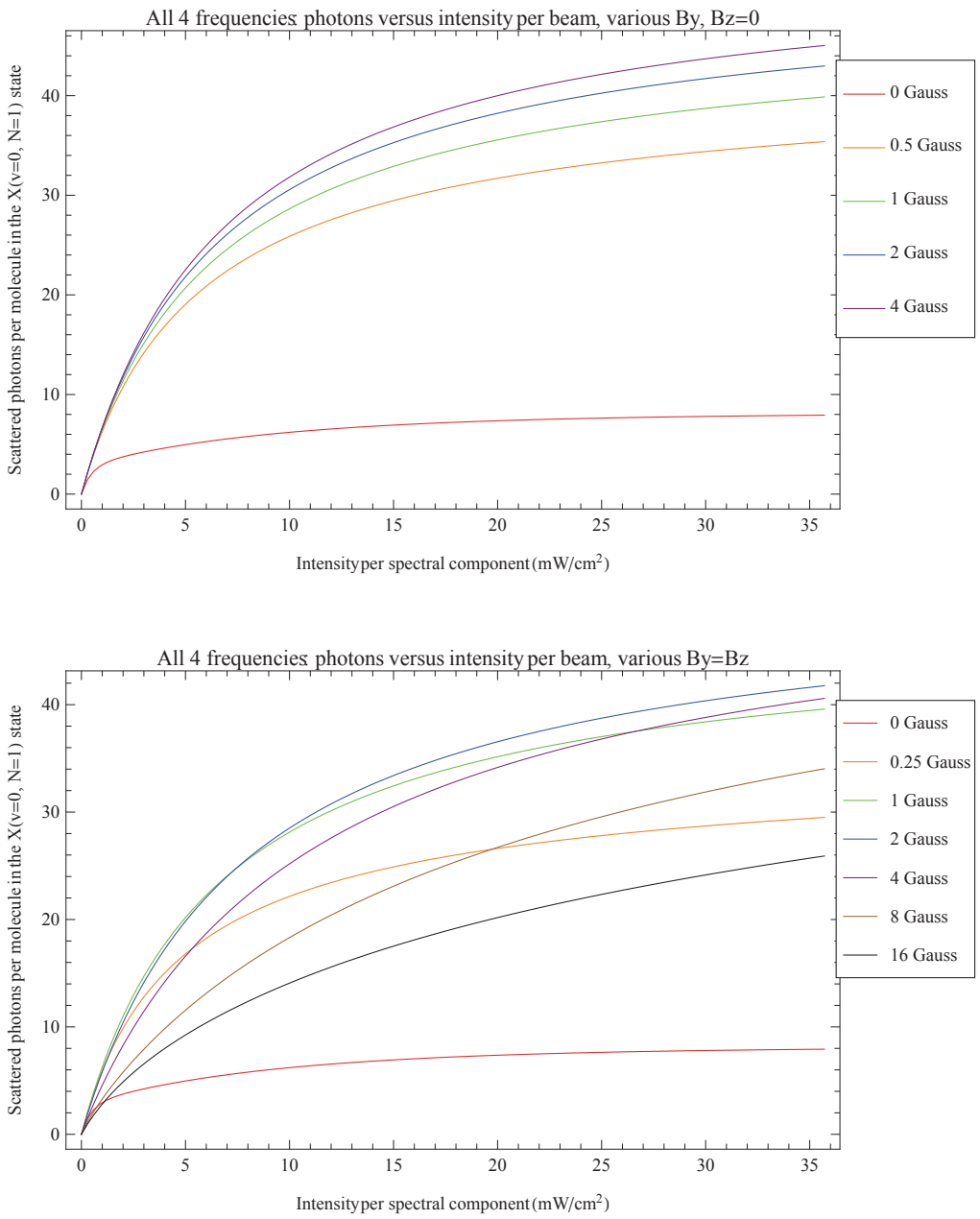

FIGURE 4.1: The number of photons scattered by the $X(v = 0, N = 1)$ states as a function of pumping laser intensity for various B-field magnitudes as predicted by the rate model. The interaction time is set as $10\,\mu$s and all of the $X(v = 0)$ states are driven on resonance. In the upper plot there is a B-field in the y direction but no component in the z direction, which is the direction of polarization of the pumping light. In the lower plot, $B_z = B_y$.

4.1.3 Population and Velocity Change Results from the Rate Model

We now model the laser cooling experiment where we drive the $X_{0,1} - A_{0,1/2}\,P(1)$ and $X_{1,1} - A_{0,1/2}\,P(1)$ transitions. We solve the rate equations (see appendix of [56]) for the case where all cooling and repump frequencies are at $5\,I_s$ of the ideal two level system and on resonance with a B-field of magnitude 2 G and direction $\hat{B} = (\hat{x} + \hat{y})/\sqrt{2}$ as defined in figure 3.2. We set the initial conditions to be that all of the population is distributed evenly amongst the 12 $X(v = 0)$ lower levels, and the other levels involved are empty. The initial velocity of the molecules is v=1 m/s in the transverse direction of the molecular beam, and in the propagation direction of the cooling light. We find the populations for each level and the final velocity up to 100 μs of interaction time. The results are shown in figure 4.2.

The results in figure 4.2 (a), (b) and (c) show that the populations are evenly distributed amongst all hyperfine levels in 10 μs. Without the $v = 1$ repump, all of the population would pile up in the $v = 1$ state in the 10 μs timescale.

This model does not include the leak to the $X(v > 1)$ levels, but considering our effective scattering rate of $\frac{1}{2} \times \frac{4}{28}\Gamma$ =3 MHz and $A(v = 0)$ to $X(v > 1)$ branching ratio of the order of 0.0001, the percentage of molecules that can end up in the $X(v > 1)$ levels is estimated to be only 2% after 60 μs of interaction with the main cooling and the $v = 1$ repump laser.

4.2 Effective Two Level System Model

We use the results from our rate models to define the parameters for the simple, two level model. We define a maximum effective scattering rate Γ_{eff} and an effective saturation intensity $I_{\text{s,eff}}$, where we find the values for these two from simulations involving all 28 levels. Once we have defined those parameters we use them in the usual expression for the scattering force, treating the system as an effective two-level system.

The expression for the effective scattering force is

$$F_{\text{eff}} = \hbar k \frac{\Gamma_{\text{eff}}}{2} \frac{s_{\text{eff}}}{1 + s_{\text{eff}} + 4\delta^{*2}/\Gamma} \tag{4.6}$$

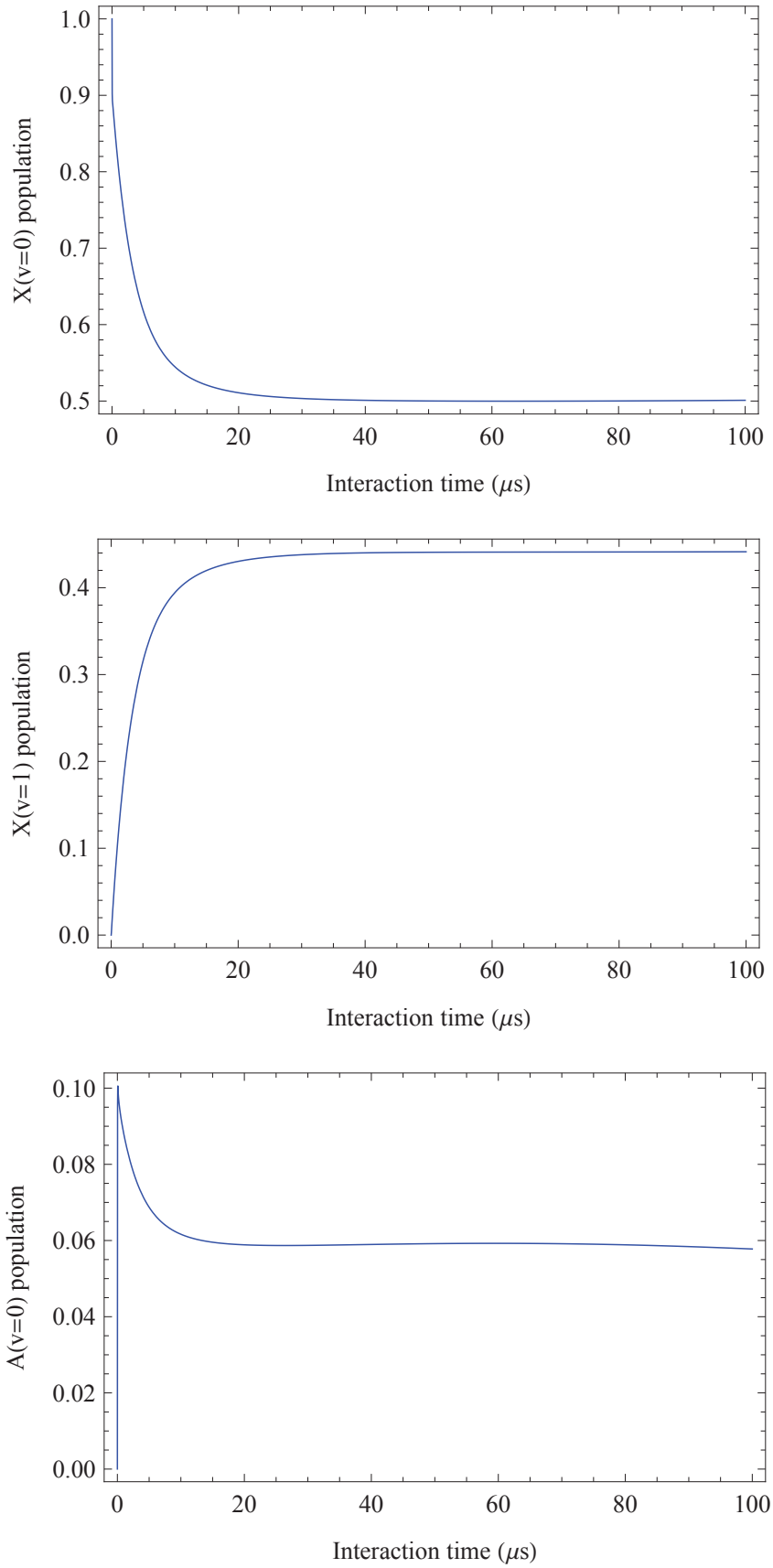

FIGURE 4.2: The population in the $X(v = 0)$, $X(v = 1)$ and $A(v = 0)$ states as a function of the interaction time All cooling and repump frequencies are at $5\,I_s$ for the ideal two level system on resonance, with a B-field of magnitude 2 G and direction $\hat{B} = (\hat{x} + \hat{y})/\sqrt{2}$ as defined in figure 3.2.

where the effective saturation parameter is $s_{\text{eff}} = I/I_{\text{s, eff}}$ and $\delta^* = \delta - 2\pi v/\lambda$ where δ_0 is the detuning and v is the molecule's transverse velocity. In a two level system, which takes into account the 28 levels. Γ is the decay rate from the excited level. Γ_{eff} is the effective decay rate. The value of Γ_{eff} should be $(1/2)\Gamma N_{\text{upper}}/N_{\text{total}}$ where N_{upper} is the number of sublevels in the upper state and N_{total} is the total number of sub-levels. The detuning is δ.

The saturation intensity for the two level system is

$$I_s = \frac{hc\pi\Gamma}{3\lambda^3} = 2.97 \text{ mWcm}^{-2} \tag{4.7}$$

where $\lambda = 663\,\text{nm}$. We solve the rate equations setting the laser intensity to be equal for all cooling and repump sideband frequencies. We find the number of photons scattered in 100μs per molecule in the $X(v = 0, N = 1)$ state with $B_x = B_y = 2\,\text{G}$, against the intensity. Then we fit the equation for the saturation intensity for a two-level system [58] to the data. The number of scattered photons is given by

$$N(s) = N_{\text{max}}\frac{s}{1+s} \tag{4.8}$$

where N is the number of scattered photons and N_{max} is the maximum number of scattered photons, which is reached as the curve plateaus. The data and the fit to the data are shown in figure 4.3. To find the effective saturation intensity $I_{\text{sat,eff}}$, we solve for s in

$$N(s) = \frac{N_{\text{max}}}{2}. \tag{4.9}$$

From the fit, we obtain the result that the effective saturation intensity is $6I_{\text{sat}} = I_{\text{sat,eff}}$ expressed in terms of I_{sat} for the two level system.

We can use the two-level model with the parameters found in this subsection as long as there are no significant leaks out of the quasi-closed cooling cycle. i.e. to the $X(v > 1)$ states.

4.2.1 The Analytic Model for Small Transverse Velocities and Radii

Figure 4.4 shows the acceleration of a SrF molecule due to the optical molasses in a 1D transverse cooling experiment where the intensity of the cooling and repump beams are 1.3 $I_{\text{sat,eff}}$, which is a realistic value for our experiment. The detuning of the cooling and repump laser frequencies from resonance in this case is 2.9 MHz.

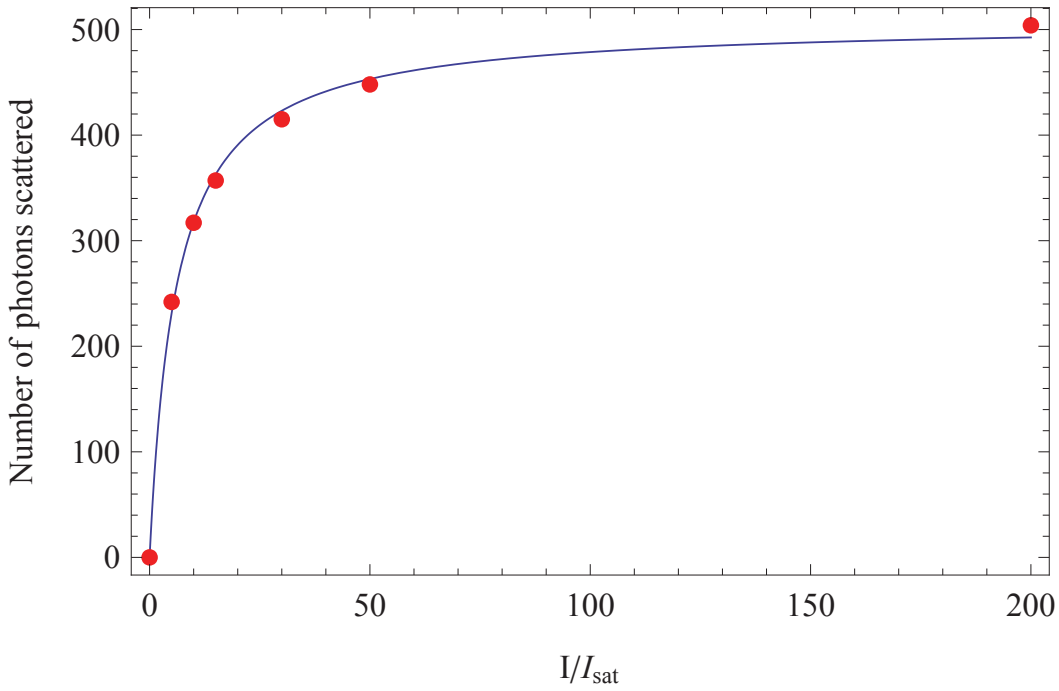

FIGURE 4.3: Variation in number of photons scattered per molecule against cooling and repump beam intensity, given by the rate equation model (points). The model is run with $B_x = B_y = 2\,\mathrm{G}$ for interaction time $100\,\mu\mathrm{s}$. The intensity is scaled by the transition saturation intensity. The curve is a fit to the data with equation $N(s) = N_{\max}\frac{s}{1+s}$.

The cooling force on the molecules varies approximately linearly with radial velocity when the radial velocity is close to zero. In this limit, the radial position and velocity of a molecule in a detection region can be found in simple analytic forms. Most notably, our signal calculated in this way is independent of the initial radial position.

For small transverse velocities, the transverse acceleration is proportional to transverse velocity

$$\dot{v}_r = -\alpha v_r. \tag{4.10}$$

where α is given by the gradient of the total transverse acceleration at the origin as follows:

$$\alpha = \left.\frac{da_{\mathrm{eff}\pm}}{dv}\right|_{v=0} = -\frac{8\,\hbar k\, s_{\mathrm{eff}}\,\Gamma_{\mathrm{eff}}\,\delta}{m\,\gamma^2\left(1+s_{\mathrm{eff}}+\frac{4\delta^2}{\Gamma^2}\right)\lambda}\,. \tag{4.11}$$

Thus,

$$v_r(t) = v_0 e^{-\alpha t}. \tag{4.12}$$

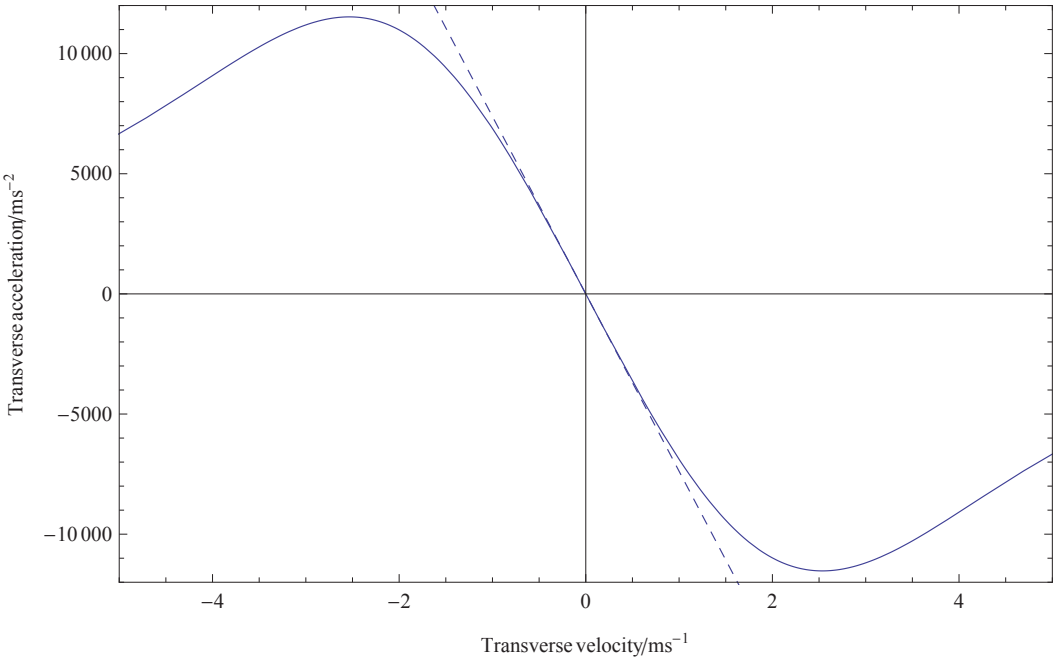

FIGURE 4.4: The acceleration of the molecules due to the optical molasses versus radial velocity (solid line). In this case, the cooling and repump beam intensity for each spectral component is $s = 1.3 s_{\text{eff}}$ and the detuning of each spectral component is $\delta = 2.9\,\text{MHz}$. The dashed line shows the approximate acceleration, which is valid at small transverse velocities, that is used in the analytic model.

Then, given initial conditions (r_0, v_0), it is easy to see the molecule's transverse position is

$$r(t) = r_0 + \frac{v_0}{\alpha}(1 - e^{-\alpha t}) \tag{4.13}$$

We consider a point source a distance l_0 from the skimmer, with forward velocity v_L. Our initial position and radial velocity are thus correlated.

$$(r_0, v_0) = (r_0, r_0 \frac{v_L}{l_0}) \tag{4.14}$$

We obtain α starting from the expression for the scattering force in the effective two-level model given by equation 4.6. The transverse acceleration for the effective two-level model for one cooling beam in the transverse direction is

$$a_{\text{eff}}(v) = \frac{\hbar k}{m} \frac{\Gamma_{\text{eff}}}{2} \frac{s_{\text{eff}}}{1 + s_{\text{eff}} + 4(\delta_0 - 2\pi v/\lambda)^2/\Gamma}, \tag{4.15}$$

where the total transverse acceleration for a molecule in two counterpropagating transverse cooling laser beams is

$$a_{\text{eff}\pm} = a_{\text{eff}}(+v) - a_{\text{eff}}(-v). \tag{4.16}$$

We would like to compare the final positions with and without cooling. Consider a three step model;

- Free flight from skimmer for time t_1
- Viscous cooling for time T
- Free flight for time t_2

With no cooling,

$$r = r_0 + v_0(t_1 + T + t_2) = r_0 \left\{ 1 + \frac{v_L}{l_0}(t_1 + T + t_2) \right\} \tag{4.17}$$

With cooling,

$$r_c = r_0 \left[1 + \frac{v_L}{l_0} \left\{ t_1 + \frac{1}{\alpha} + \left(t_2 - \frac{1}{\alpha} \right) e^{-\alpha T} \right\} \right] \tag{4.18}$$

Figure 4.5 is a plot of α, the gradient of the acceleration against velocity in the optical molasses, versus detuning with $s = 1.3\, s_{\text{eff}}$. The plot shows that α is largest at $-2.9\,\text{MHz}$ detuning, where $\alpha = 7380\, s^{-1}$. Therefore the molecules that lie within the range of validity of the linear approximation for the effective cooling force experience the strongest cooling forces at this detuning value.

Now we would like to use the model to estimate how much increase in the brightness of the molecular beam we can achieve by comparing the molecules that propagate freely with the molecules that pass through a transverse 2D optical molasses, which we will refer to as the "cooled molecules."

The brightness of a molecular beam is given by the number of molecules per steradian per unit area. Where the angle between the propagation direction of the molecular beam and the trajectory of the molecules with the largest transverse velocity is θ, and the corresponding solid angle is Ω (shown in figure 4.6) such that

$$\theta = \frac{v_r}{v_L} \quad \Omega = 4\pi \sin^2\left(\frac{\theta}{2}\right), \tag{4.19}$$

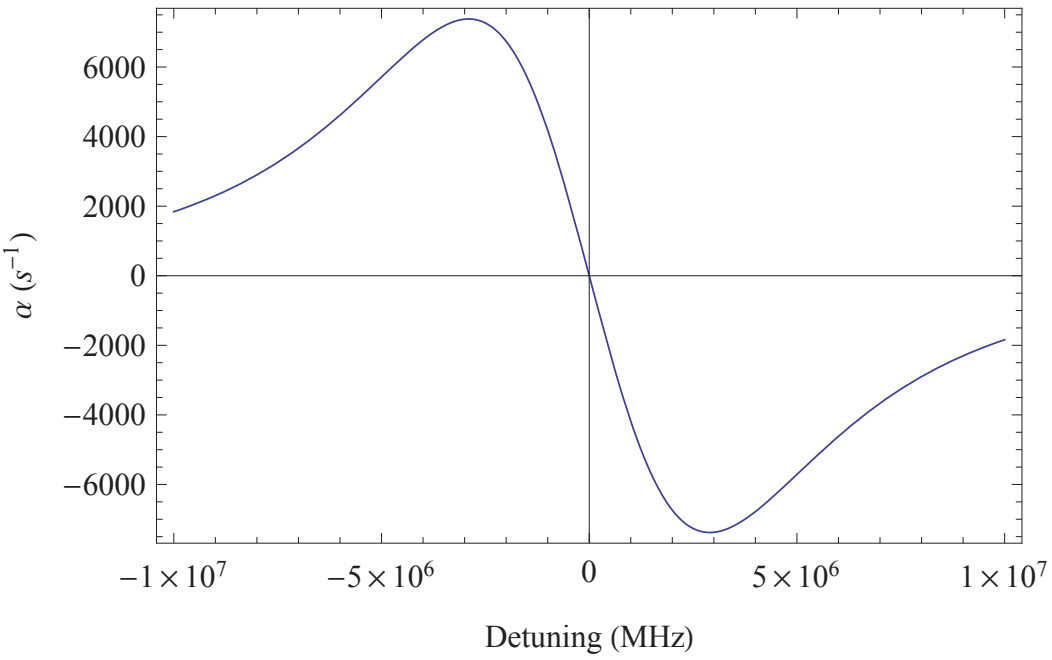

FIGURE 4.5: α, the gradient of the acceleration against velocity in the optical molasses, versus detuning with $s = 1.3 s_{\text{eff}}$.

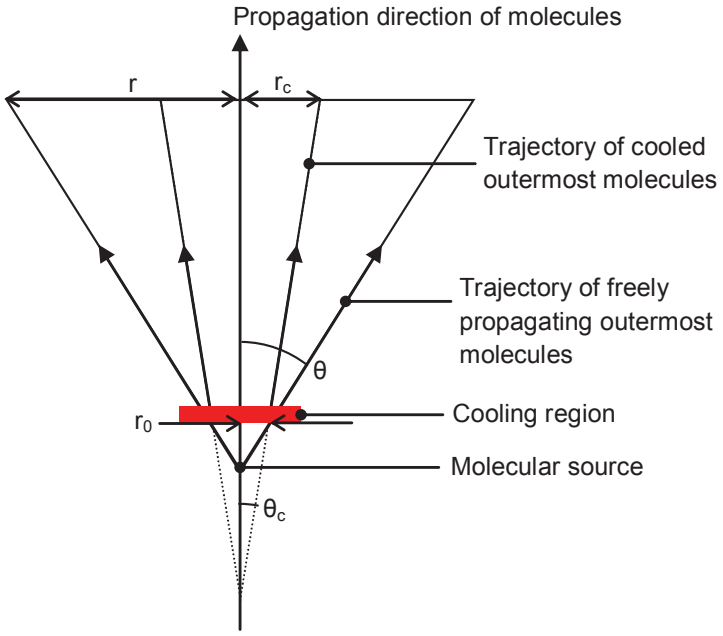

FIGURE 4.6: A schematic diagram to show the definitions of θ and θ_c in the calculation of brightness.

the brightness of a free molecular beam and a cooled molecular beam are

$$B = \frac{N}{\Omega\,\pi\,r^2} \quad \text{and} \quad B_c = \frac{N}{\Omega_c\,\pi\,r_c^2}. \tag{4.20}$$

respectively. Where we use the equation for brightness for systems where the position and velocity are not coupled. Although in this system the position and velocity of the molecules are coupled, this still gives us some measure of how effective the beam brightening is.

Therefore, we can write the brightness of the cooled beam over the brightness of the free beam as

$$\frac{B}{B_c} = \frac{v_r^2\,r_c^2}{v_0^2\,r^2} \tag{4.21}$$

We use the analytic expressions for the transverse positions and velocities of the molecules that propagate freely, and the molecules that pass through a transverse 2D optical molasses, given in equations 4.17, 4.18 and 4.12.

The transverse velocity of the cooled molecules over the freely propagating molecules is simply

$$\frac{v_r(t)}{v_0} = e^{-\alpha t} \tag{4.22}$$

so the speed is reduced to $1/e$ of the initial speed in $1/\alpha$=135 μs. In our experiment, we can have an interaction time of 100 μs. In this time the speed is reduced to 0.48 times the original speed.

Now r/r_c depends on the position we detect at as shown in figure 4.7. The molecules reach the upper detection region 112 μs after leaving the cooling region so the maximum value of r/r_c we can measure in our apparatus is 1.92. This, together with the value of $v_c/v = 0.48$ we obtained, gives a maximum fractional increase in brightness of $B_c/B = 16$.

4.2.2 The Numerical Model

The analytic model in the previous subsection, as simple and illuminating as it is, is only valid for 1 % of all of the molecules which pass through the skimmer. This is because the linear approximation is only valid for molecules with initial transverse speeds of up to 1 m/s, but the molecules from the source have transverse speeds of

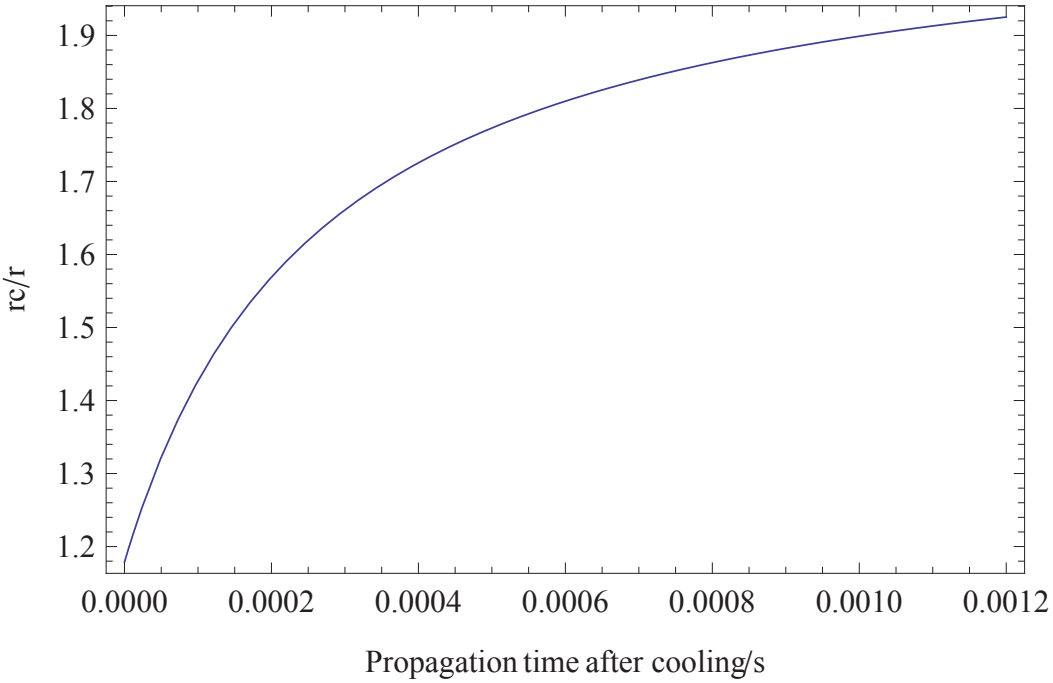

FIGURE 4.7: r/r_c against free propagation time of molecules after leaving the cooling region.

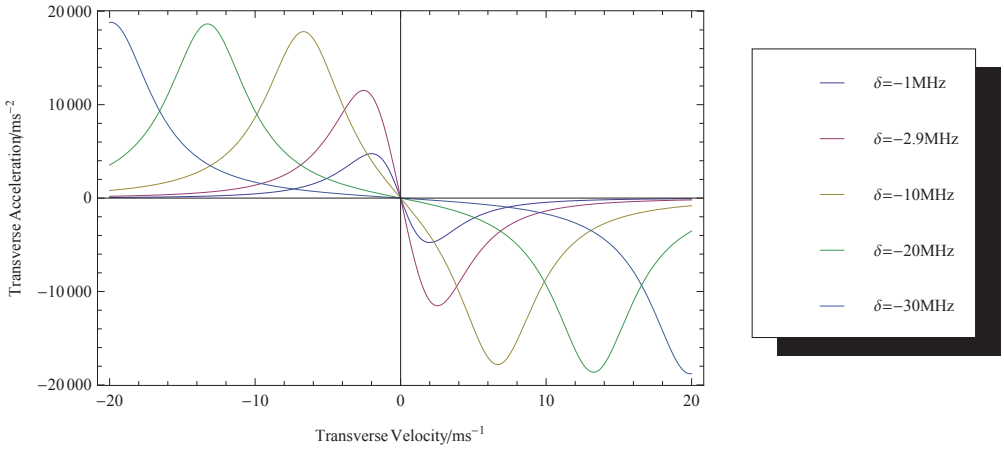

FIGURE 4.8: The acceleration experienced by molecules of different transverse velocities propagating through a 1D optical molasses for different cooling and repump laser detunings δ.

up to 10 m/s. Figure 4.8 shows the acceleration experienced by molecules of varying transverse velocities propagating through a 1D optical molasses for different cooling and repump laser detunings δ. We can see that at larger detunings than 2.9 MHz, the molecules with small transverse velocities <1 m/s accelerate less, but in fact molecules with larger transverse velocities can accelerate significantly more. From this, it is clear that we should model the molecules with transverse velocities >1 m/s too.

To model the propagation of all molecules, we use a numerical model to extend our simulation.

We perform the calculation in 1D. First, we numerically integrate the scattering force equation (4.6) to find the radial position $r(t)$ and the radial velocity $v_r(t)$ for a set of molecules with a range of initial radial velocities. The molecules are assumed to have an even angular distribution from a point source. We propagate all molecules with and without cooling. We count the number of molecules that lie within a particular radius at the upper and lower detection regions for each case, to find the enhancement signal. The variable parameters in this model are the detection radii.

To start off with, we would like to conduct the easiest experiment, which has parameters that maximises the enhancement signal, which is the signal we measure experimentally, rather than the brightness. We use the numerical model to determine the largest expected enhancement signal, the experimental parameters that give rise to this value, and the signal-to-noise ratio on the enhancement signal. The experimental parameters that we can choose at this stage are the radii of the molecular beam we detect at the lower and upper detection regions. The error in the enhancement signal is given by

$$\delta S_{\text{enh}} = \sqrt{\sum_{i=\text{un, ln, uc, lc}} \left(\frac{\partial S_{\text{enh}}}{\partial S_i} \delta S_i \right)^2}. \tag{4.23}$$

We assume that the noise is limited by the shot-noise in the photon detection by the PMTs. Such that

$$\delta S_i = \sqrt{S_i} \tag{4.24}$$

and equation 4.23, the error in the enhancement signal, becomes

$$\delta S_{\text{enh}} = \sqrt{\frac{S_{\text{un}}}{S_{\text{ln}}^2} + \frac{S_{\text{uc}}}{S_{\text{lc}}^2} + \frac{S_{\text{un}}^2}{S_{\text{ln}}^3} + \frac{S_{\text{uc}}^2}{S_{\text{dc}}^3}} \tag{4.25}$$

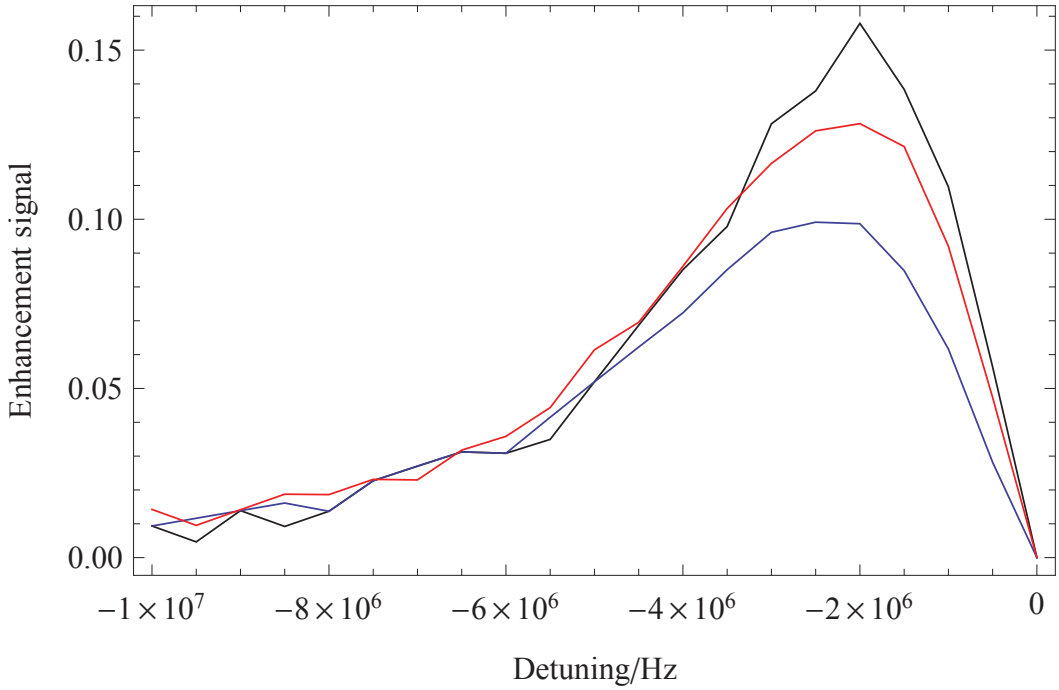

FIGURE 4.9: The enhancement signal for various values of detuning, as calculated by the numerical model, with the detection radius fixed at 1.5 mm in the lower detection region, and set at 1.0 mm (black line), 1.5 mm (red line) and 2.0 mm (blue line) in the upper detection region.

We measured the number of molecules in the ground state with the highest population to be 1,600. This was with a typical detection area of 14mm^2. Our detection efficiency is 2.3%. So the maximum number of photons we can detect with a single-frequency probe beam is 46 per shot. We use this value as a guide to obtain $S_{\text{un, ln, uc, lc}}$ in numbers of photons detected from our simulation and evaluate the signal-to-noise ratio.

First we fix the lower detection radius to be 1.5 mm. This corresponds to a molecular beam size of 6 mm in diameter at the upper detection region, which is a molecular beam size that we can detect there in the uniform part of the probe beam. The enhancement signal and signal-to-noise ratio of the enhancement signal are shown in figures 4.9 and 4.10 respectively.

The enhancement signal and associated signal-to-noise ratio increases as the radius of the lower detection region decreases. This tells us that we should set the detection radius of the upper detection region to be as small as possible. We determine this experimentally, by finding the minimum radius that we can detect while getting an adequate signal-to-noise ratio on the time-of-flight profiles in the duration of a typical experiment. We determine this value to be 1.75 mm.

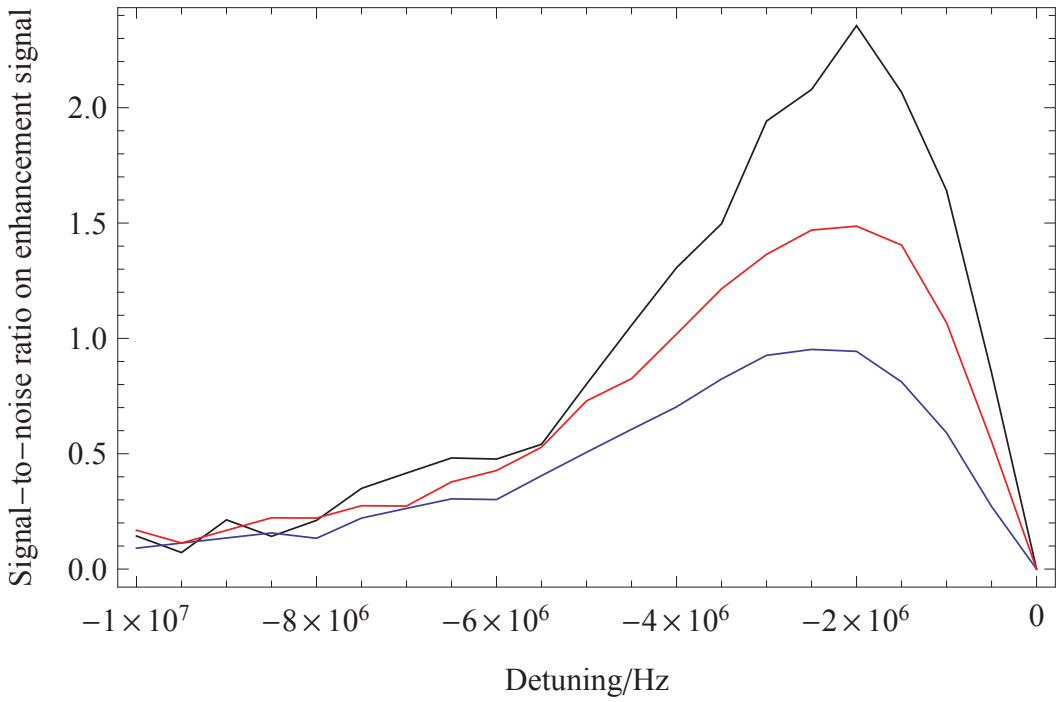

FIGURE 4.10: The signal-to-noise ratio of the enhancement signal for various values of detuning, as calculated by the numerical model, with the detection radus fixed at 1.5 mm in the lower detection region, and set at 1.0 mm (black line), 1.5 mm (red line) and 2.0 mm (blue line) in the upper detection region.

Now we carry out the numerical simulation to predict the enhancement signal vs detuning for our selected lower- and upper aperture radii of 1.5 mm and 1.75 mm respectively. The results are shown in 4.11

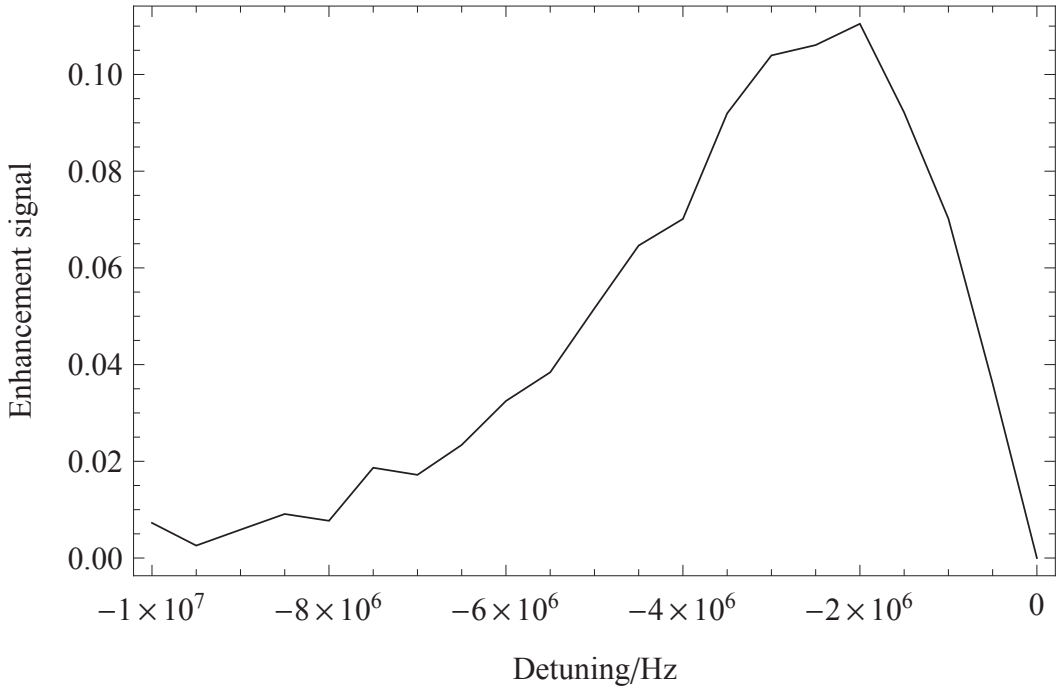

FIGURE 4.11: The enhancement signal for various values of detuning, as calculated by the numerical model, with the detection radius fixed at 1.5 mm in the lower detection region, and set at 1.75 mm in the upper detection region.

Chapter 5

1D Transverse Cooling Experiment

As described in section 3.1, in the 1D transverse cooling experiment, the molecules propagate through a 1D optical molasses in the transverse direction. Then the laser-induced fluorecence, resulting from their interaction with a probe beam, is detected at two points. The 1D optical molasses consists of two, large 60 mm by 5 mm counterpropagating cooling beams and a small repump beam, which is reflected to intersect the molecular beam multiple times. The probe laser is resonant with one of the $X(v = 0)$ to $A(v = 0)$ hyperfine transitions. There are two shutters–one that blocks the probe laser beam and switches after every shot, and another that blocks the cooling laser beam and switches every two shots.

5.1 Sorting and Processing Acquired Data

Each data set collected in the experiment is used to calculate one value for the enhancement signal with a standard error on the mean for a particular detuning value for the cooling laser beam. The smallest repeating unit of data consists of four time-of-flight profiles taken under different conditions: at the lower detection region with the cooling beam unblocked and blocked, and at the upper detection region with the cooling beam unblocked and blocked. Each of these time-of-flight profiles has associated voltage value data from the photodiode after the cooling laser shutter. The whole data set consists of around 300 of these repeating units.

To process the data, first, we integrate the time-of-flight profiles and subtract the background. To do this, we first we determine the time range that the time-of-flight profiles are recorded in. We determine these time intervals by inspecting the mean of all of the time-of-flight profiles taken in the lower detection region with the probe beam unblocked, and the mean of all of the time-of-flight profiles taken in the upper detection region with the lower probe beam blocked. The mean time-of-flight profiles are shown in figure 5.1. From these, we take the time-of-flight profile in the lower detection region to lie between $t_{\mathrm{min,l}} = 1200\,\mu$s to $t_{\mathrm{max,l}} = 1460\,\mu$s where $t = 0$ is defined by the Q-switch, and the the time-of-flight profile in the upper detection region to lie between $t_{\mathrm{min,u}} = 1900\,\mu$s to $t_{\mathrm{max,u}} = 2300\,\mu$s. Next, we calculate the mean background value by taking the mean of the amplified PMT signal voltage values in the range of $1600\,\mu$s to $1700\,\mu$s after the Q-switch, which lies comfortably outside the range from $t_{\mathrm{min,l/u}}$ and $t_{\mathrm{max,l/u}}$. We finally evaluate an integral of each of the 4×300 time-of-flight profiles by subtracting the mean background value from each of the amplified PMT voltage values composing the time-of-flight profile, and summing those that lie within $t_{\mathrm{min,l/u}}$ and $t_{\mathrm{max,l/u}}$.

Now we have 4×300 integrals corresponding to each time-of-flight profile in our data set. However, we are unsure as to which values correspond to the data taken with the cooling light blocked or unblocked. This is due to the unreliable timings of the shutter on the cooling laser beam switching. To sort these, for each data value, we sum the associated signal from the photodiode, which is placed after the shutter that blocks the cooling laser beam. Plotting the total photodiode signal against the data point number gives figure 5.2. We sort the whole data set into those that have associated total photodiode signal values that are larger than the mean of these total signal values (the cooled data), and those that do not (the uncooled data).

Given the sorted values of time-of-flight profile integrals, all that is left to do is to calculate the measured enhancement signal value and its standard error on the mean for the data set. Recall that the enhancement signal is given by

$$S_{\mathrm{enh}} = \frac{S_{\mathrm{un}}}{S_{\mathrm{ln}}} - \frac{S_{\mathrm{uc}}}{S_{\mathrm{lc}}}, \tag{5.1}$$

where S_{un} and S_{uc} is the integrated time-of-flight profile from the laser-induced fluorescence signal in the upper PMT with no cooling and with cooling respectively, and S_{ln} and S_{lc} are the same signals in the lower PMT. For the ith unit out of our $N = 300$ data units, we have one value for each signal, and we label these $S_{\mathrm{un,i}}$, etc. To calculate the enhancement signal, we use the equation

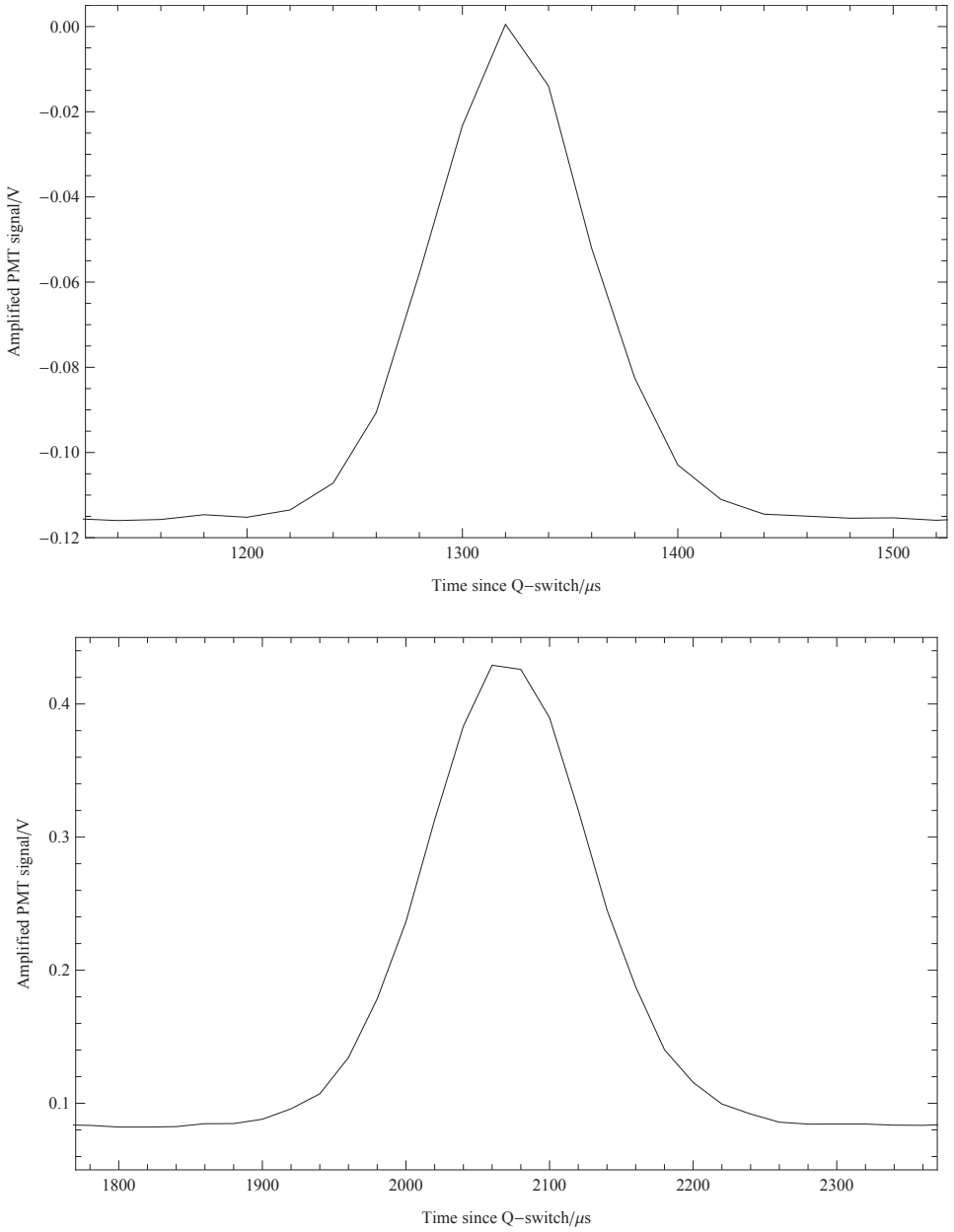

FIGURE 5.1: The mean of all of the time-of-flight profiles taken in the lower detection region with the probe beam unblocked (above), and the mean of all of the time-of-flight profiles taken in the upper detection region with the lower probe beam blocked (below) for one data set.

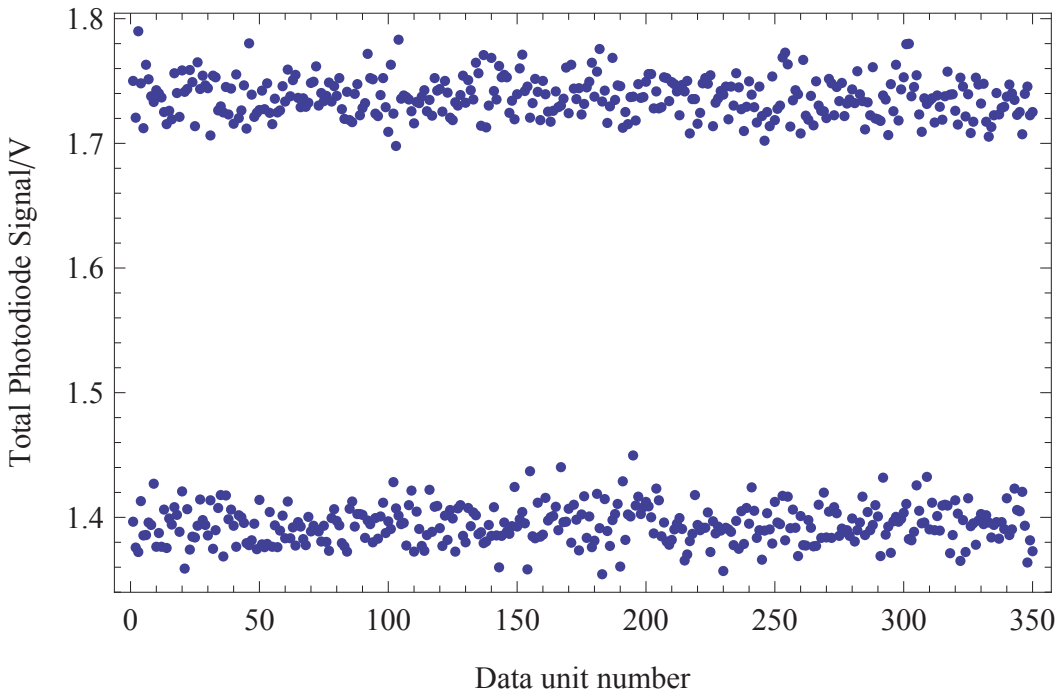

FIGURE 5.2: The sum of the signal from the photodiode placed after the shutter that blocks the cooling laser beam to verify its state. The horizontal axis is just the number that shows the sequence in which the points were taken.

$$S_{\text{enh}} = \frac{\overline{S}_{\text{un}}}{\overline{S}_{\text{ln}}} - \frac{\overline{S}_{\text{uc}}}{\overline{S}_{\text{lc}}}, \tag{5.2}$$

where

$$\overline{S}_{\text{X}} = \sum_{i}^{N} \frac{S_{\text{X},i}}{N}; \tag{5.3}$$

i.e. we take the mean values of the time-of-flight profile integrals for each of the four data types (lower/upper detection region, cooled/uncooled), then calculate the enhancement signal from the mean values. We do not calculate the enhancement signal for each data unit, then take the mean. i.e. we do not use

$$\hat{S}_{\text{enh}} = \frac{1}{N} \sum_{i}^{N} \left(\frac{S_{\text{un},i}}{S_{\text{ln},i}} - \frac{S_{\text{uc},i}}{S_{\text{lc},i}} \right). \tag{5.4}$$

This is an important distinction and its repercussions will be discussed in section 5.3.

The standard error on the mean (e_{enh}) associated with the enhancement signal (S_{enh}), which is calculated using equation 5.2, is given by combining errors in the

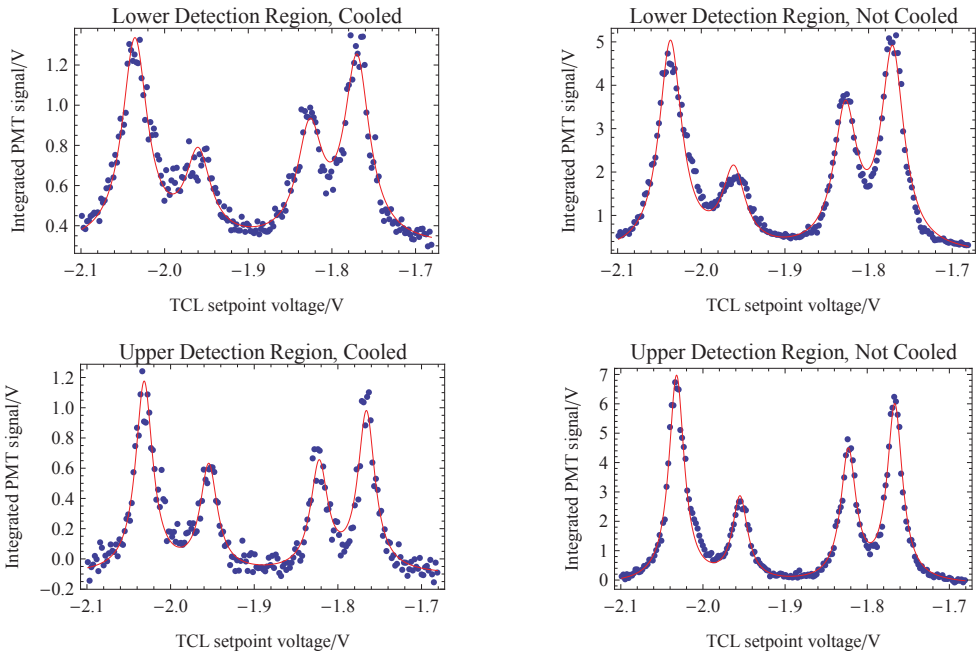

FIGURE 5.3: The laser-induced fluorescence spectra of the four hyperfine transitions $X_{0,1} - A_{0,1/2}\,P(1)$ taken with the cooling laser detuned from resonance by -5 MHz at the two detection regions for the cases with the cooling laser blocked and unblocked. Each spectrum consists of 200 data points with 5 shots per point. The blue points are the data points and the red lines show the fitted Lorentzian curves.

usual way, which leads to

$$e_{\mathrm{enh}} = \sqrt{\left(\frac{S_{\mathrm{un}}}{S_{\mathrm{ln}}}\right)^2 \left\{\left(\frac{\sigma_{\mathrm{un}}}{S_{\mathrm{un}}}\right)^2 + \left(\frac{\sigma_{\mathrm{ln}}}{S_{\mathrm{ln}}}\right)^2\right\} + \left(\frac{S_{\mathrm{uc}}}{S_{\mathrm{lc}}}\right)^2 \left\{\left(\frac{\sigma_{\mathrm{uc}}}{S_{\mathrm{uc}}}\right)^2 + \left(\frac{\sigma_{\mathrm{lc}}}{S_{\mathrm{lc}}}\right)^2\right\}}, \quad (5.5)$$

where

$$\sigma_X = \sqrt{\frac{\sum_i^N (S_{X,i} - \overline{S}_X)^2}{N-1}}. \quad (5.6)$$

5.2 Finding the Effect of Neighbouring Transitions by Fitting to Spectra

As discussed in section 3.8, by parking the probe laser on the resonance of one hyperfine transition and probing at two locations, we attempt to eliminate any misleading effects due to the redistribution of the population over different hyperfine levels after cooling. However, one concern with this method is the contribution of

laser-induced fluorescence from the transitions with frequencies close to the one that we are probing on. Therefore, we find the shift caused in our measurement of the enhancement signal by scanning the probe laser frequency and fitting Lorentzian functions to each resonance in the resulting spectra. The spectra are shown in figure 5.3.

We note that the spectrum taken in the lower detection region has broader spectral features than the spectrum taken in the upper detection region due to Doppler broadening. The molecules with the highest transverse velocity that we observe in the lower detection region have a higher transverse velocity than the molecules with the highest transverse velocity that we observe in the upper detection region as we observe more molecules in the lower detection region.

The function we fit to each spectrum is

$$L_X(V) = A + \sum_{k=1}^{4} \mathcal{L}(V)_{Xk}, \quad \mathcal{L}_{Xi}(V) = \frac{B_i D}{4(D^2/4 + (V - C_i)^2)} \tag{5.7}$$

where the subscript k refers to each of the four transition peaks in a spectrum and X refers to the data set (upper/lower detection region, cooled/not cooled). To find the fractional contribution to the amplitude of one peak, resulting from the non-resonant peaks, we calculate

$$\mathcal{W}_{X,m} = \sum_{\substack{k=1 \\ k \neq m}}^{4} \mathcal{L}_{X,k}(C_m)/\mathcal{L}_X(C_m), \tag{5.8}$$

The values of $\mathcal{W}_{X,m}$ are shown in table 5.1.

	m=1	2	3	4
X =uc	0.0174	0.0600	0.0832	0.0362
dc	0.0315	0.175	0.185	0.0659
un	0.0114	0.0689	0.0611	0.0318
dn	0.0239	0.167	0.131	0.0611

TABLE 5.1: The values of the fractional cotribution to one peak, from the other peaks, $\mathcal{W}_{X,m}$, corresponding to the spectra in figure 5.3 (The laser-induced fluorescence spectra of the four hyperfine transitions $X_{0,1} - A_{0,1/2}\,P(1)$ taken with the cooling laser detuned from resonance by -5 MHz at the two detection regions for the cases with the cooling laser blocked and unblocked). The peaks are labelled m =1,2,3 and 4 from left to right.

We find the change in the fractional contribution due to the wings of the individual Lorentzian functions when the cooling light is blocked and unblocked. We calculate

m=1	2	3	4
0.0121	0.0197	0.0297	0.00759

TABLE 5.2: The values of $\mathcal{W}_{\mathrm{enh},m}$, corresponding to the spectra in figure 5.3. The peaks are labelled m =1,2,3 and 4 from left to right.

fractional shift in amplitude in the spectra of the cooled molecules due to the hyperfine redistribution. These are given by

$$\Delta\mathcal{W}_{\mathrm{uc/lc},m} = |\mathcal{W}_{\mathrm{uc/lc},m} - \mathcal{W}_{\mathrm{un/ln},m}|. \tag{5.9}$$

Then, in order to find the systematic shift of the enhancement signal due to this effect, we combine these shifts in the usual way we combine errors. We define the fractional shift to be the shift due to the redistribution of populations due to the cooling and repump light, so by definition, there are no shifts on B_{un} and B_{dn}. Therefore, the systematic shift of the enhancement signal is

$$\mathcal{W}_{\mathrm{enh},m} = \frac{B_{\mathrm{uc},m}}{B_{\mathrm{lc},m}}\sqrt{(\mathcal{W}^2_{\mathrm{uc},m} + \mathcal{W}^2_{\mathrm{lc},m})}. \tag{5.10}$$

The results are shown in table 5.2.

From the numerical modelling in section 4.2.2, we see that the maximum enhancement signal we expect to see is ∼0.11. The shift $\mathcal{W}_{\mathrm{enh}}$ of the enhancement signal due to the contributions of the other peaks is less than 3% for all of the $\mathrm{X}_{0,1} - \mathrm{A}_{0,1/2}\,\mathrm{P}(1)$ transitions. Thus we have shown that the method of measuring the enhancement signal while parking the laser on a resonance does not suffer a significant error caused by the wings of nearby transitions. There is no need to scan the probe laser frequency to generate a spectrum, then fit to the transition lineshapes to eliminate the unwanted contributions. This speeds up the data collection immensely.

5.3 Errors when Taking the Ratio of Noisy Data Values

Here, we discuss the error that arises when taking the ratio of two values, when the signal-to-noise ratio of each value is close to one. First, the problem will be described generally, then we explore the specific effect that the problem has on our

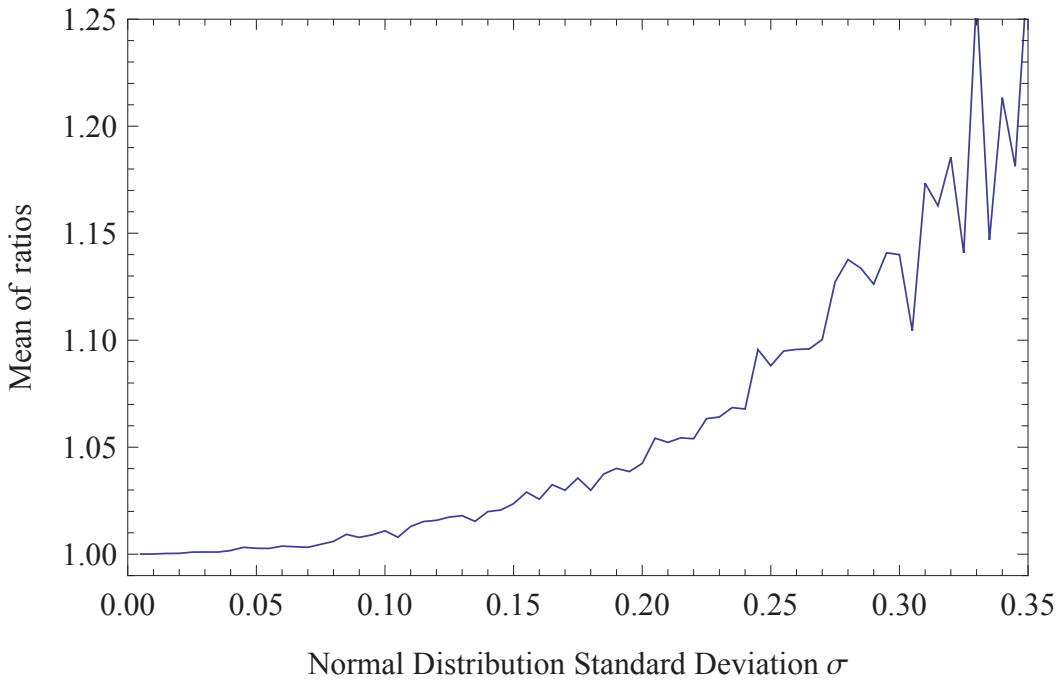

FIGURE 5.4: The mean of the ratios $R_i = A_i/B_i$ of pairs of values taken from two sets of 10,000 normally distributed random numbers A and B in a numerical simulation. The mean of the normal distribution is 1, and the standard deviation is σ.

experimental data by analyzing the data in a way that does introduce this error, and a way that avoids it.

We take two sets, A and B, of N normally distributed random numbers. The mean and standard deviation of the normal distribution that the numbers are taken from are 1 and σ respectively. We pair up values from each set and divide them such that we have the set of ratios $R_i = A_i/B_i$ where i runs from 1 to N. As σ increases, we can intuitively tell that the mean of the ratios $\bar{R}$ will be greater than the ratio of the means $\bar{A}/\bar{B}$. This is because the ratio $R_i = A_i/B_i$ approaches infinity as the denominator approaches zero.

To confirm this effect, we run a numerical simulation. For each value of standard deviation σ, we generate the data sets A and B with N =10,000 then calculate $\bar{R}$. The resulting values of $R(\sigma)$ are shown in figure 5.4. It can be seen that the value of the mean increases exponentially with the standard deviation of the distributions.

Now we introduce this error in real data. We process the data using a method where we take ratio of two values from a distribution with errors that are around 10% of the distribution mean. We simply record the laser-induced fluorescence spectrum of

the four hyperfine transitions states $X_{0,1} - A_{0,1/2}\,P(1)$ in the upper detection region and lower detection region, and repeat this 20 times. The detection takes place in the upper detection region and lower detection region on alternate shots, so that each pair of spectra are taken under similar conditions. Now we have 40 spectra–20 that have been taken in the lower detection region, and 20 that have been taken in the upper detection region.

In the first method, we fit a function, which is a sum of four Lorentzian functions with an offset (equation 5.7), to each spectrum. From these fits, we derive the amplitude $B_{m,p,\mathrm{u/l}}$ of each of the four Lorentzian functions, for all 40 spectra. We let m be the peak number, labelled from left to right in the spectrum, and p be the spectrum number, labelled in the order that they were taken. The final letter denotes the detection region. Next, we divide the amplitude of each peak from the spectrum taken in the upper detection region by the amplitude of each peak from the spectrum taken in the lower detection region. This gives us $R_{m,p} = B_{m,p,\mathrm{u}}/B_{m,p,\mathrm{l}}$, for $p = 1$ to 20. Finally, we compute the mean and standard error on the mean $\bar{R}_p$ of R for each p. These values are shown as the black points with error bars in figure 5.5.

In the second method, we average the 20 spectra taken in the upper detection region, and obtain one mean spectrum by averaging all 20 data points taken at the same probe laser frequency value. We do the same with the 20 spectra taken in the upper detection region. Then, we fit the sum of the four Lorentzian functions with an offset to each of these spectra to find the peak amplitudes $\bar{B}_{m,\mathrm{u,l}}$. Finally, we divide the amplitude of each peak from the mean spectrum taken in the upper detection region by the amplitude of each peak from the lower detection region, so we end up with $\bar{R}'_p = \bar{B}_{m,\mathrm{u}}/\bar{B}_{m\mathrm{l}}$. These values are shown as the red points in figure 5.5.

From the figure 5.5, we can see that the mean ratio values calculated using the first method are significantly higher than those calculated using the second method. This is a result of taking the ratio of noisy data.

5.4 Results: Dispersion Curves

To recap, we run the 1D cooling experiment using the experimental setup described in chapter 3. First we tune the lasers to the correct frequencies and lock them with the Transfer Cavity Lock software. Then, we locate the setpoint voltages of the

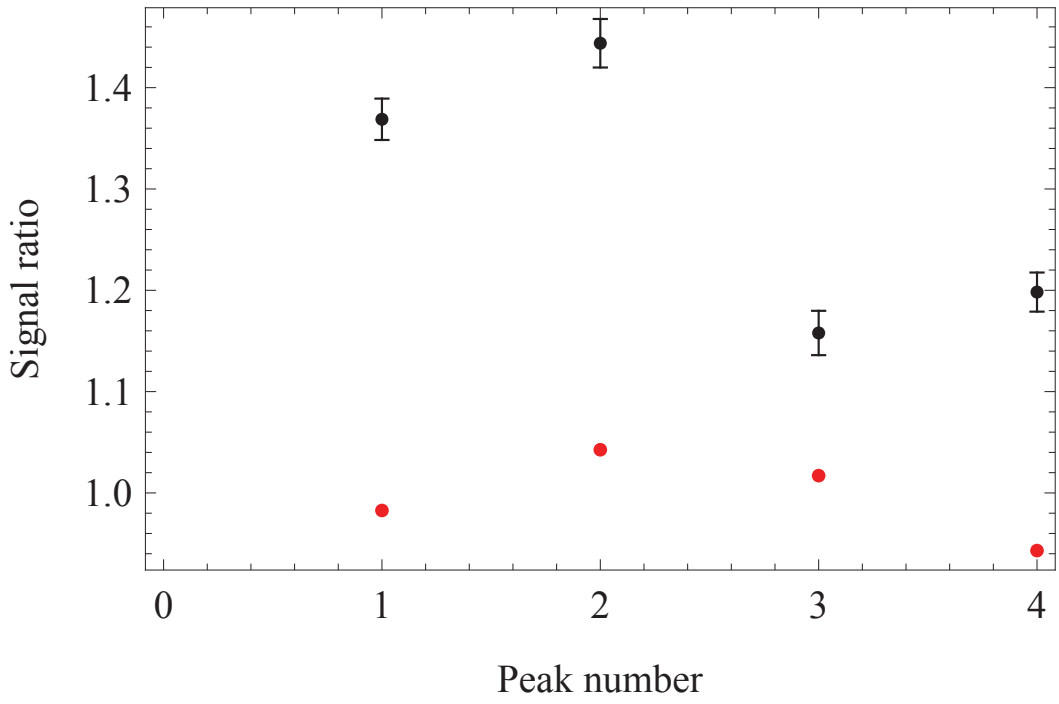

FIGURE 5.5: A sum of four Lorentzian functions with an offset were fitted to each of 20 spectra taken in the upper detection region and 20 spectra taken in the lower detection region of the $X_{0,1} - A_{0,1/2}\,P(1)$ transitions. The amplitudes of each of the four lorentzian functions were recorded for each spectrum with the peaks labelled 1 to 4 from left to right. The black points show the mean and standard error on the mean of the ratios of the amplitudes for the spectra taken in the upper detection region to the lower detection region. In this case, the ratio is taken before the ratios are averaged. The red points show the ratio when the amplitudes from the 20 spectra in the upper detection region, and the 20 spectra in the lower detection region are averaged first, then the ratio is calculated.

probe laser where they are resonant with the $X_{0,1} - A_{0,1/2}\,P(1)$ cooling transitions. We then set the carrier frequency of the modulated cooling laser to lie at the centre of the lowest and the highest out of the resonant frequencies we have found. Let us call this frequency $\nu_{0,v=0}$. In this way, all transition frequencies are addressed. Next, we send just this cooling light into the cooling region, and send the modulated repump light into the probe region. We scan the frequency over the range of the $X_{1,1} - A_{0,1/2}\,P(1)$ transitions. This gives us a spectrum of laser-induced-fluorescence intensity versus repump laser carrier frequency. We find the frequency at which the laser-induced-fluorescence intensity is highest, and park the repump laser carrier frequency there. To check that the pumping and repumping work, we lock the probe laser on one of the $X_{0,1} - A_{0,1/2}\,P(1)$ hyperfine transition frequencies, and monitor the laser-induced-fluorescence first with just the modulated cooling laser beam to ensure that the molecules are pumped out. Then we add the modulated repump

laser beam to ensure that the molecules are pumped back into the $X(v = 0)$ level.

For the main body of the experiment, we take units of four shots of data at a time, where each unit consists of a time-of-flight profile of the laser-induced fluorescence taken in the upper and lower detection regions with the cooling beam blocked and unblocked. First we record a data set consisting of 250 units, with the cooling laser parked at $\nu_{0,v=0}$ and the probe laser parked on the resonance of one of the hyperfine transitions. Then we analyze this data to give a value for the mean enhancement signal, and a standard error on the mean. We do this by subtracting the background signal from each time-of-flight profile, summing the points in the time-of-flight profile, finding the mean and standard deviations of the integrals of the time-of-flight profiles for each condition (upper/lower detection region, cooling light blocked/unblocked), then calculating the enhancement signal and its error using these means and standard deviations. We have now acquired a value for the enhancement signal and its error for a particular value of detuning for the cooling laser.

We repeat the procedure altering the cooling laser detuning each. We take data and calculate the enhancement signal and its error at 5 MHz intervals of the cooling laser detuning values. The entire procedure is repeated for each $\mathrm{X}_{0,1} - \mathrm{A}_{0,1/2}\,\mathrm{P}(1)$ transition.

The results of the 1D transverse cooling experiment, are shown in figures 5.6, 5.7, 5.8. These graphs show the enhancement signal versus detuning of the cooling laser beam carrier frequency with the probe laser parked on the $\mathrm{X}_{0,1}(3/2, 2) - \mathrm{A}_{0,1/2}$, $\mathrm{X}_{0,1}(3/2, 1) - \mathrm{A}_{0,1/2}$, and $\mathrm{X}_{0,1}(1/2, 1) - \mathrm{A}_{0,1/2}$ transitions respectively. Each of the graphs show a dispersion curve.

Figure 5.9 shows an enhancement signal versus detuning plot with a wider detuning range. There is a dispersion curve at the centre with a repeating pattern as the detuning is changed. The smaller peaks occur as the sidebands on the cooling laser move out of resonance with one hyperfine transition, and into resonance with the next one, if there is one.

5.5 Model of the 1D Transverse Cooling Experiment

We constructed an improved model of the 1D transverse cooling experiment based on to the numerical model described in section 4.2.2. Three major improvements

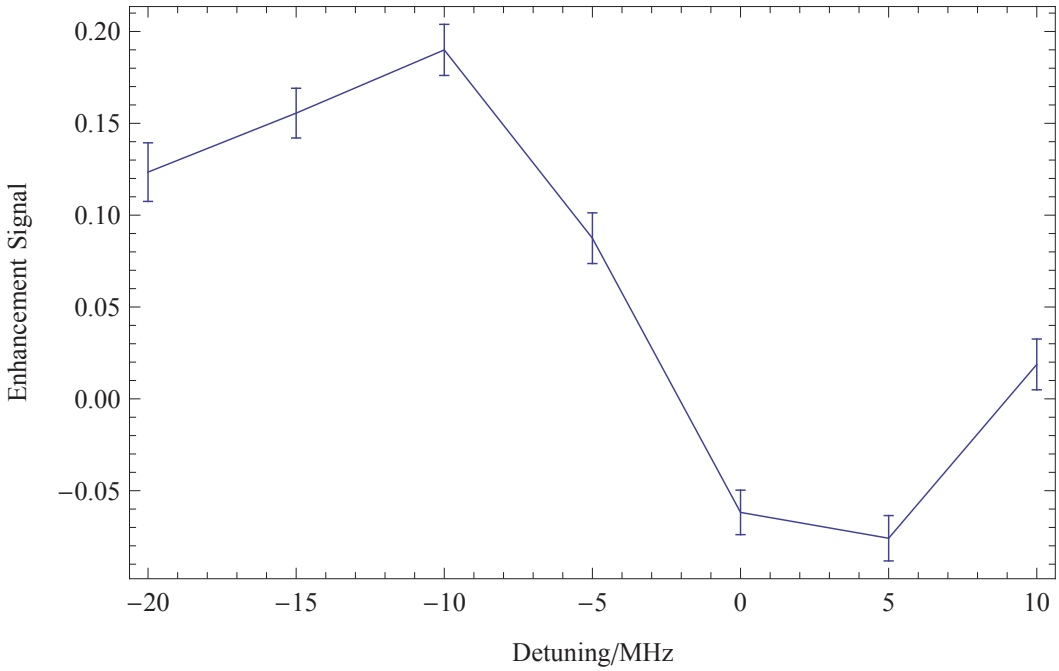

FIGURE 5.6: Enhancement signal versus detuning of the cooling laser beam carrier frequency, given by the 1D transverse cooling experiment, with the probe laser parked on the $X_{0,1}(3/2, 2) - A_{0,1/2}$ transition.

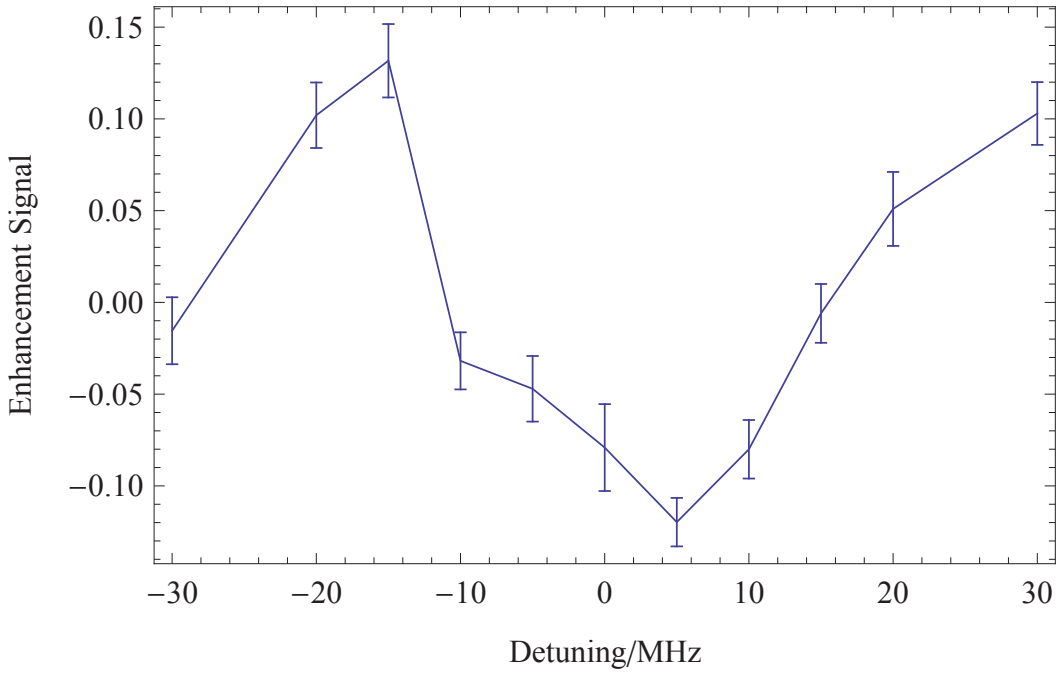

FIGURE 5.7: Enhancement signal versus detuning of the cooling laser beam carrier frequency, given by the 1D transverse cooling experiment, with the probe laser parked on the $X_{0,1}(3/2, 1) - A_{0,1/2}$ transition.

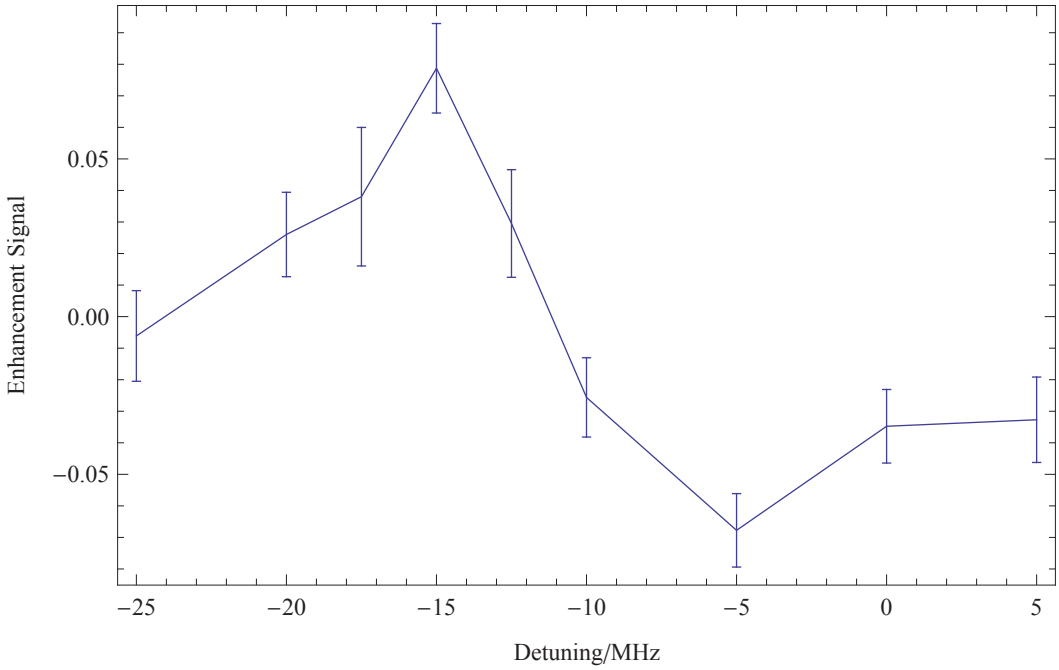

FIGURE 5.8: Enhancement signal versus detuning of the cooling laser beam carrier frequency, given by the 1D transverse cooling experiment, with the probe laser parked on the $X_{0,1}(1/2,1) - A_{0,1/2}$ transition.

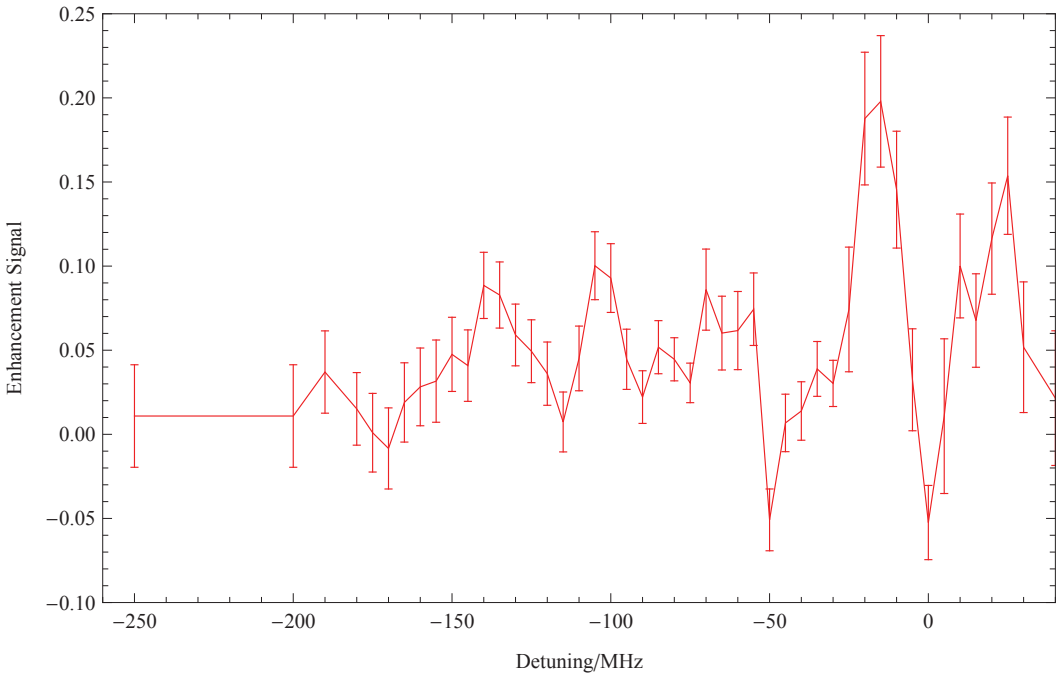

FIGURE 5.9: Enhancement signal versus detuning of the cooling laser beam carrier frequency, given by the 1D transverse cooling experiment, with the probe laser parked on the $X_{0,1}(3/2,1) - A_{0,1/2}$ transition.

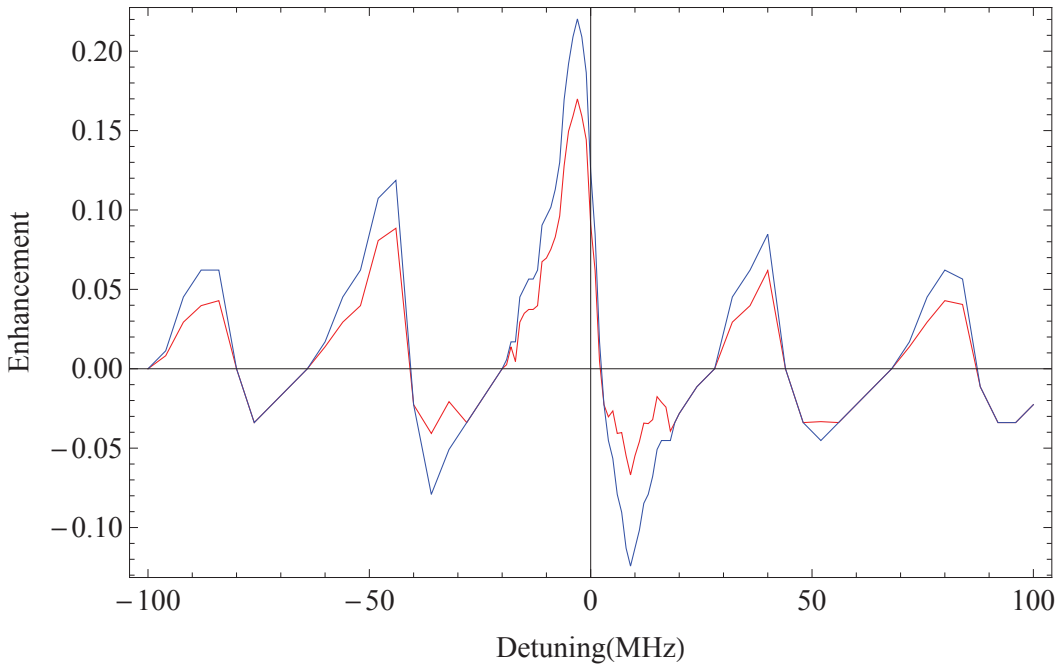

FIGURE 5.10: Enhancement signal (red) and fractional change in upper detection region signal (blue) versus detuning of the cooling laser beam carrier frequency, given by the improved model for the 1D transverse cooling experiment.

were made. The first was to include the effects of all frequency orders of the modulated cooling laser on a molecule in any given state. Previously, the model only included the effects of the laser frequency component that is closest to the transition frequency of the molecule. We now include all orders, even the carrier and third order sidebands which are small. The second improvement was to account for the unequal detunings between each laser frequency and the transition that it is supposed to address, arising from the fact that the sidebands on the cooling laser are evenly spaced, but the hyperfine transitions are not. The previous numerical model had assumed that all modulated laser frequency components were on resonance at the same time, and that the detunings were all equal. Finally, the new model simulates the trajectories of a set of molecules with random initial velocities within the source. Previously, the molecules were assumed to be distributed evenly over velocity and angle. The enhancement signal values for various laser detunings as predicted by the model is shown in figure 5.10.

The experimental results in section 5.4 broadly agree with the model, as they all show dispersion with the correct frequency scale. This implies that our 1D cooling experiment is successfully cooling the molecules and the supersonic SrF beam is becoming brightened. However, we must be careful. If there is a hyperfine pumping effect which varies both spatially and with detuning, it could mimc the beam

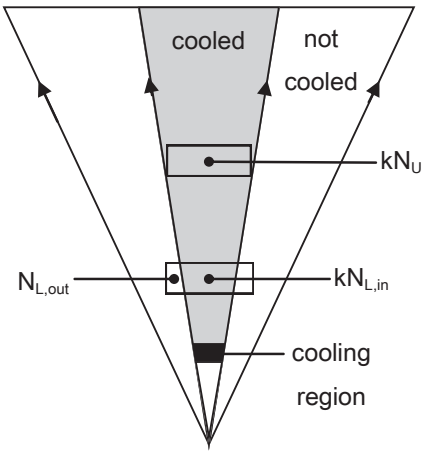

FIGURE 5.11: A diagram to show our model molecular beam where not all of the molecules interact with the cooling laser beam. In this configuration, the redistribution of molecules among different hyperfine state gives rise to a non-zero enhancement signal value, even if the interaction time is too short for there to be a non-zero enhancement signal value as a result of the beam brightening effect.

brightening effect we are trying to see. For example, suppose that the transverse extent of the cooling laser beam is slightly small, such that all of the molecules that are detected in the upper detection region interact with the cooling laser beam, but not all of the molecules that are detected in the lower detection region interact with the cooling beam. We also suppose that the longitudinal extent of the cooling light is so small that there is no significant cooling effect, and the enhancement signal is 0. Now let us say that the effect of the cooling light is to transfer the population between the hyperfine states, such that if N molecules in the state that we are probing pass through the cooling laser beam, kN molecules emerge. Now let $N_{\mathrm{L,in}}$ and $N_{\mathrm{L,out}}$ be the number of molecules in that will and will not interact the cooling laser beam when it is on. Then $N_{\mathrm{L}} = N_{\mathrm{L,in}} + N_{\mathrm{L,out}}$ is the total number of molecules we detect in the lower detection region without cooling. Furthermore, let N_{U} be the number of molecules we detect in the upper detection region without cooling. Then, the enhancement signal will be given by

$$\tilde{S}_{\mathrm{enh}} = \frac{kN_{\mathrm{U}}}{kN_{\mathrm{L,in}} + N_{\mathrm{L,out}}} - \frac{N_{\mathrm{U}}}{N_{\mathrm{L}}}. \tag{5.11}$$

We now take $N_{\mathrm{U}} = N_{L,in} = 1$ and $N_{L,out} = 0.1$, and plot $\tilde{S}_{\mathrm{enh}}$ against k. This is shown in figure 5.12.

This shows that if not all molecules interact with the cooling laser beam, the effect

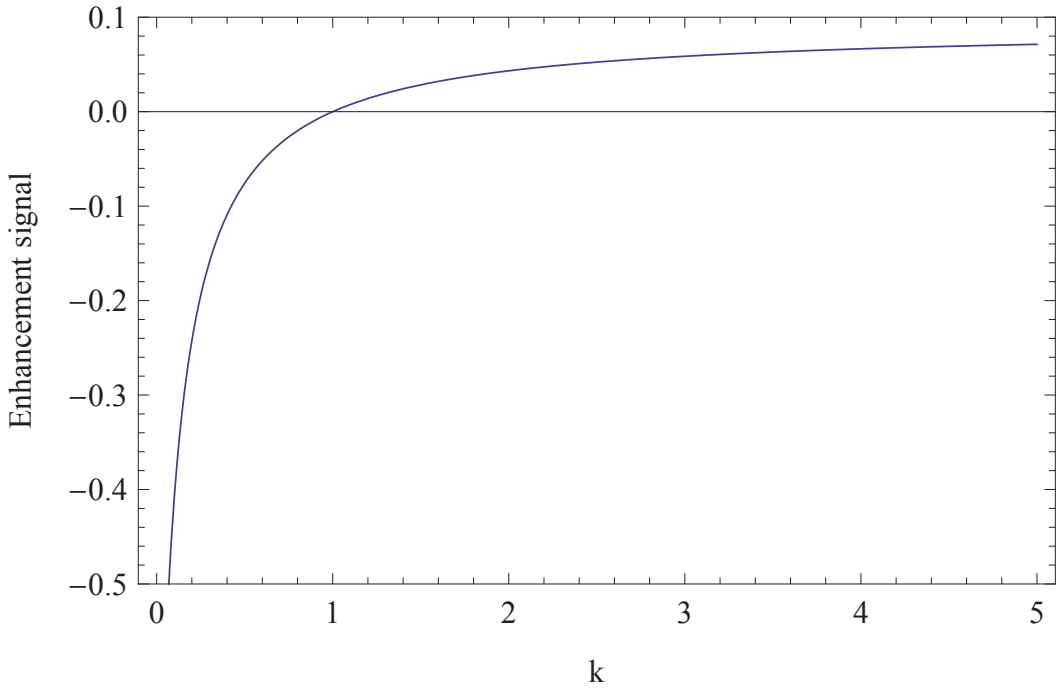

FIGURE 5.12: A plot of the optical pumping-induced signal $\tilde{S}_{\text{enh}}$ against k (equation 5.11) where $N_{\text{U}} = N_{\text{L,in}} = 1$ and $N_{\text{L,out}} = 0.1$

of population transfer between hyperfine levels will lead to a non-zero enhancement signal. If as a result of the interaction with the cooling laser beam the population piles up and increases in the state we are probing such that $k > 1$ which leads to a positive enhancement signal value when there is no cooling. If the population decreases as a result of the cooling interaction $k < 1$, and there will be a negative enhancement signal value when there is no cooling.

5.6 Results with Reduced Interaction Length

One way to ensure that a non-zero enhancement signal is due to the brightening of the molecular beam due to the 1D transverse optical molasses, rather than an effect due to the redistribution of population among the hyperfine levels, is to check that the enhancement signal gets smaller with reduced interaction length. This is because pumping effects take place quickly, as an we have seen in figure 4.2, and a non-zero enhancement factor arising from population redistibution will not change once the interaction time is increased above this value.

We performed the 1D transverse cooling experiment, as described in section 3.1 with an interaction length of 4.8 cm, to obtain the enhancement signal versus detuning

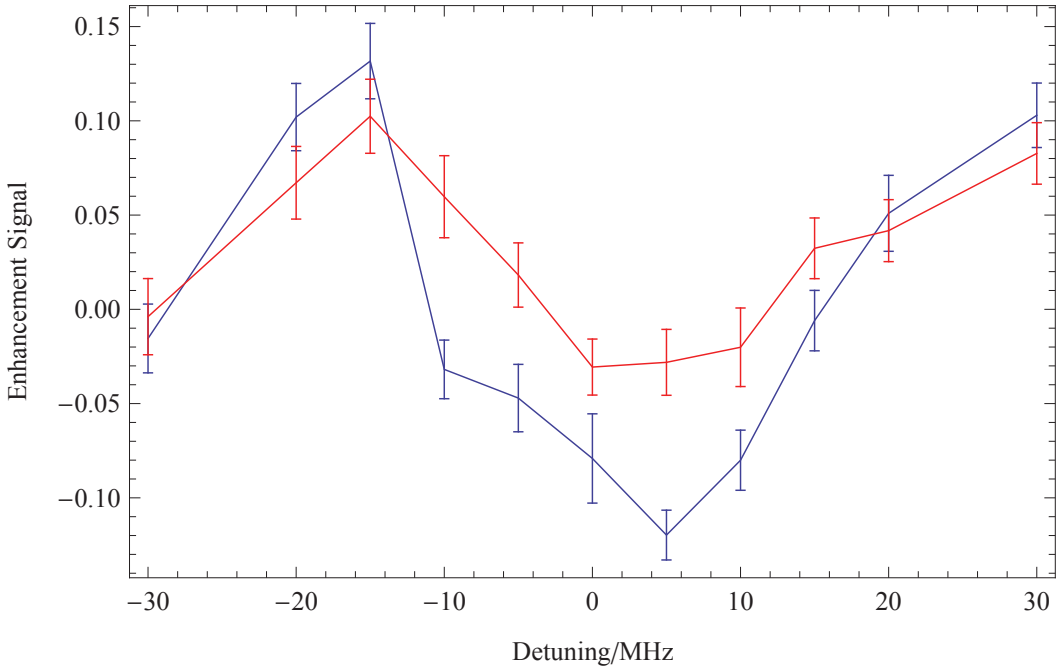

FIGURE 5.13: Enhancement signal versus detuning of the cooling laser beam carrier frequency, given by the 1D transverse cooling experiment, with the probe laser parked on the $X_{0,1}(3/2,1) - A_{0,1/2}$ transition. The blue line shows the results for the experiment with 4.8 cm interaction length, and the red line shows the results for the experiment with 2.4 cm interaction length.

of the cooling laser beam carrier frequency, with the probe laser locked to the $X_{0,1}(3/2,1) - A_{0,1/2}$ transition. Then we repeated the same experiment but with the interaction length reduced to 2.4 cm. The enhancement signals with their errors are shown in figure 5.13, where the blue line shows the results for the experiment with the full interaction length, and the red line shows the results for the experiment with half of the interaction length. We can see that the two sets of results give two dispersion curves with the maxima and minima located in the same detuning values. However, the dispersion curve corresponding to the experiment with the halved interaction length has a difference in the maximum and minimum enhancement signal value that is roughly half of that in the dispersion curve corresponding to the experiment with the full interaction length. In the full interaction dispersion curve, the difference between the maximum and minimum enhancement signal values is approximately 24%, wheras in the half interaction length dispersion curve, this is approximately 13%. This confirms that the enhancement signal is not an artefact that is generated due to pumping effects, and the dispersion curves do indeed result from the effect of the transverse 1D optical molasses brightening the molecular beam. However, there seems to be an offset on the dispersion curve for

the experiment with the halved interaction length, so that it appears to be shifted upwards relative to the full interaction length data, and the model.

5.7 Offset on Zero of the Enhancement Signal

There is an offset of about 5% on the dispersion curve corresponding to the experiment with the halved interaction length. We have seen this in the first set of results in section 5.4 in the enhancement signal versus detuning plot of the cooling laser beam carrier frequency, given by the 1D transverse cooling experiment, with the probe laser parked on the $X(v'' = 0,\, N'' = 1\, J'' = 3/2,\, F'' = 2)$ to $A(v' = 0,\, J' = 1/2)$ transition. The maximum enhancement signal in this plot is 17% and the minimum is -7%, again giving an offset of about 5% in the enhancement signal.

When conducting the experiments, we have found that this offset on the enhancement signal is sensitive to the alignment of the cooling beam relative to the SrF beam. The width of the laser beam in the cooling region is comparable to the width of the molecular beam. Therefore, one possible cause for the offset could be a misalignment of the cooling laser beam.

We run a simulation using our numerical model described in section 4.2.2 to illustrate what such an effect would have on the enhancement signal. The radii of the lower detection region and the upper detection region are 1.5 mm and 1.75 mm respectively. We assume that the molecules that lie within a radius of 1 mm about the propagation axis of the molecules at the lower detection region are cooled, but the molecules that lie outside this radius are not cooled. All molecules that are detected in the upper detection region are cooled. This means that the enhancement signal is given by

$$S_{\text{enh}} = \frac{N_{\text{uc}}}{N_{\text{lc,in}} + pN_{\text{ln,out}}} - \frac{N_{\text{un}}}{N_{\text{ln}}} \tag{5.12}$$

where N_{uc} is the number of cooled molecules that are detected in the upper detection region, $N_{\text{lc,in}}$ is the number of cooled molecules that are detected in the lower detection region, $N_{\text{ln,out}}$ are the number of molecules that never interact with the cooling laser beam and are detected in the lower detection region, and N_{un} and N_{ln} are the numbers of molecules detected in the upper and lower detection regions respectively, when the cooling laser beam is blocked. The factor p accounts for the hyperfine population redistribution effect, and we set this as 1.5, which models a situation where molecules are pumped out of the probed state when they are

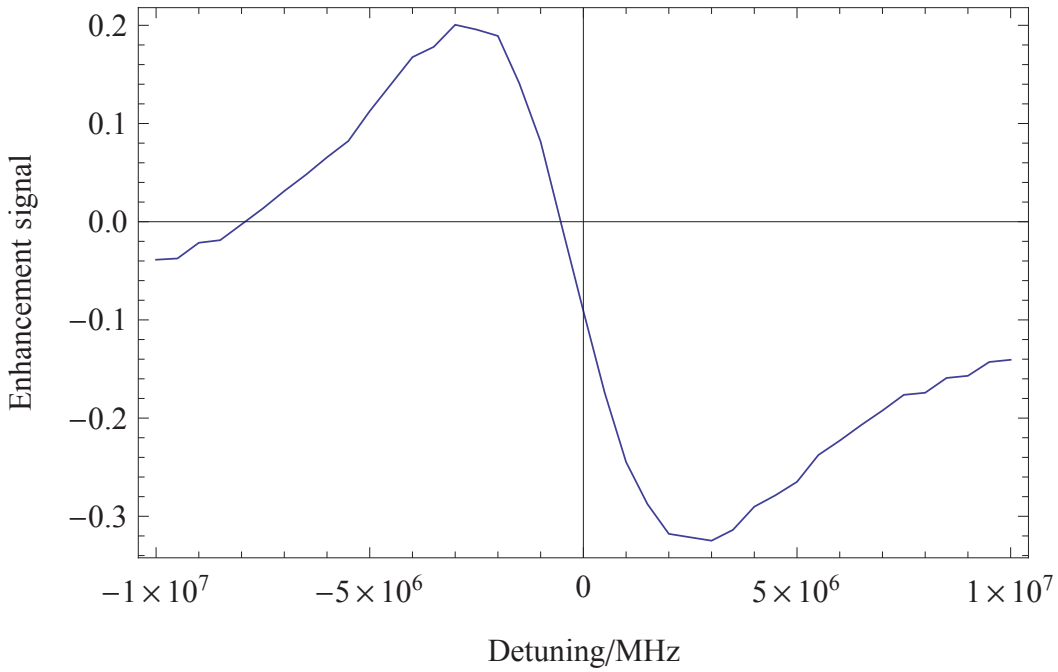

FIGURE 5.14: Enhancement signal versus detuning of the cooling laser beam carrier frequency, given by the numerical simulation of the 1D transverse cooling experiment, where molecules that lie within a radius of 1.0 mm about the propagation axis of the molecules at the lower detection region are cooled, but the molecules that lie outside this radius are not cooled. The cooling laser beam also redistributes the population among the hyperfine states. The radii of the lower detection region and the upper detection region are 1.5 mm and 1.75 mm respectively.

cooled. We run the numerical simulation using equation 5.12, and its results are shown in figure 5.14.

We can see in the simulation results that the enhancement signal has an offset, and the absolute of the maximum value is smaller than absolute of the minimum. Therefore the offsets on zero that we have seen in our data sets could be explained by this combined effect of a slight misalignment of the cooling laser beam and population redistribution among different hyperfine states caused by the cooling laser.

5.8 Sources of Error

We have already described in section 5.7 that an error can be introduced if the cooling laser beam is misaligned so that it does not interact with all of the molecules that are detected. This effect does appear to be taking place in our experiment,

as the offset on zero in the enhancement signal curve changes as the alignment of the cooling laser is altered. Since the width of the cooling beam is so close to the width of the molecular beam that is detected, it is experimentally challenging to reliably align the cooling laser so well with the molecular beam as to eliminate the zero offset reliably. In our experiments, we repeat the alignment process until the absolute value of the zero offset is smaller than the maximum enhancement signal we expect to measure.

Another systematic error could be introduced if the probe laser beams at the upper and lower detection regions are not parallel with each other where they intersect the molecular beam. If they are not parallel, the molecules at each detection region will experience different Doppler shifts, and will not be resonant with the probe laser at the same time. In order to eliminate this effect, we measure the separation between the two probe beams 1 m and 5 m after the detection region, and ensure that the separation is constant to the nearest cm by adjusting their alignment. Furthermore, we scan the frequency of the probe laser to take a spectrum of the $X(v'' = 0)$ to $A(v' = 0)$ hyperfine transitions at the upper and lower detection regions simultaneously, and ensure that the resonances occur at the same laser frequency. As well as measuring the separation between the two probe beams, we monitored their positions at 5 m after the detection region. These did not show any drift to the nearest mm after a monitoring period of six hours, which is a typical duration of our experiment. Therefore we verified that the pointing direction of the probe beams are stable for the duration of our experiments. We also monitored the probe intensity over a similar timescale and verified that this does not vary by more than $\pm 5\%$.

In a cooling experiment, the enhancement signal value drifts with the probe laser frequency. This is because the lineshapes of the probed transition is different in the upper and lower detection regions due to different contributions of Doppler broadening. To show this, we conduct the cooling experiment with the probe laser scanned slowly over a hyperfine transition, rather than parked on resonance. We see that the resulting spectra do not overlap perfectly, and the enhancement signal varies with probe laser frequency. However, as we have seen in section 3.4.2, the fluctuations in the laser frequency average to zero over time. We can be satisfied that this effect does not affect our enhancement signal measurement as long as the laser does not exhibit long-term drift on the timescale of the duration of the experiment.

Fluctuations in the molecular source intensity could potentially cause an error in the measured value of the enhancement signal. The smallest unit of our data consists four time-of-flight profiles, taken with in the upper- and lower detection regions with the cooling beam blocked and unblocked. Each of these time-of-flight profiles are of different shots, i.e. four molecular pulses yields four time-of-flight profiles, which we then integrate. However, we found that these fluctuations average to zero in our data sets

In the injection lock setup for the $X(v = 1)$ to $A(v = 0)$ repump, the slave laser can become unstable and unlock during the experiments. This can be attributed to a slow drift in the slave laser current. As the slave laser becomes unstable, we can see from its output from the scanning Fabry-Perot cavity that the shape of the mode changes. When this happens, the width of the transmission peak tends to become broader, and the amplitude decreases. This happens intermittently, and we discard data the slave laser has become very unstable or has unlocked. However, the slave laser becoming unstable is a gradual effect, and is not completely eliminated. We circumvent this in our experiment by randomizing order of the cooling laser detuning at which we take data to measure the enhancement signal. We also repeat measurements at certain detunings, to ensure that the experiment is repeatable. This way we can ensure that a systematic error has not been introduced by the effect of the unstable slave laser.

5.9 Limitations

There are two main factors that limit the amount of cooling that we get in our present experimental setup. The first is interaction length and the second is repump laser beam intensity. These two factors lead to the third problem which is the difficulty of aligning the cooling and repump laser beams to interact with all of the molecules that we probe.

The interaction length is limited to the current 48 mm because the physical configuration of the experiment limits the number of times the repump laser beam can be reflected back through the molecular beam. The size of the repump beam is 2 mm in the longitudinal direction of propagation of the molecular beam by 5 mm in the transverse direction. The diameter of the windows that provide optical access for the cooling and repump laser beams pump to reach the molecular beam is 60 mm in diameter. Given this size of window, and the configuration of the rest of the apparatus, the repump laser beam can only be made to intersect the

molecular beam 24 times when it is made to reflect off the mirror that directs it into the chamber at the slightest possible angle. To extend the interaction length, the geometry of the experiment needs to be changed.

The power of the repump laser is just 25 mW as it enters the vacuum chamber. The effective saturation intensity of the cooling and repump transitions is 10 $\mathrm{mW/cm^{-2}}$ per hyperfine transition. However, the 6 mm diameter windows only transmit 98 % of the repump laser beam light per pass, such that after the 24 passes, the power is reduced to just 62 % of its initial value. To ensure that the intensity of the repump laser is at least the saturation intensity on its last pass, the initial intensity must be at least 16 $\mathrm{mW/cm^{-2}}$ per hyperfine transition, so the total initial intensity must be at least 64 $\mathrm{mW/cm^{-2}}$, which in turn means the cross-sectional size of the beam needs to be smaller than 0.39 $\mathrm{cm^2}$. Although we have conservatively chosen the beam size to be 0.1 $\mathrm{cm^2}$ in this experiment, we would ideally like to expand the beam to 15 mm in the transverse direction so that it is easier to align with the molecular beam. However, in order to achieve this, and simultaneously increase the interaction length, we would need more power in the repump laser beam.

5.10 Improvements

We made improvements to the experimental setup in order to increase the interaction time of the molecules with the cooling and repump laser beams, and to increase the intensity of the cooling and repump beams. We achieved this by making two major changes to the apparatus. The first improvement was to add a tapered amplifier to the laser system to amplify the repump beam from 50 mW at the slave diode output to 300 mW at the tapered amplifier output. The second improvement was to exchange the segment of the chamber of the cooling region to a longer chamber, with windows of length 20 cm.

A schematic diagram of the new vacuum chamber is shown in figure 5.16. The total length of the new segment is 402 mm, compared to the old segment, which was 175 mm. The window is rectangular with a length of 200 mm, compared to the old window, which was circular with a diameter of 60 mm. The window starts at 102 mm from the bottom of the chamber, so the detection regions are raised and the new distance from the source to the lower detection region is 802 mm and the new distance from the source to the upper detection region is 1252 mm.

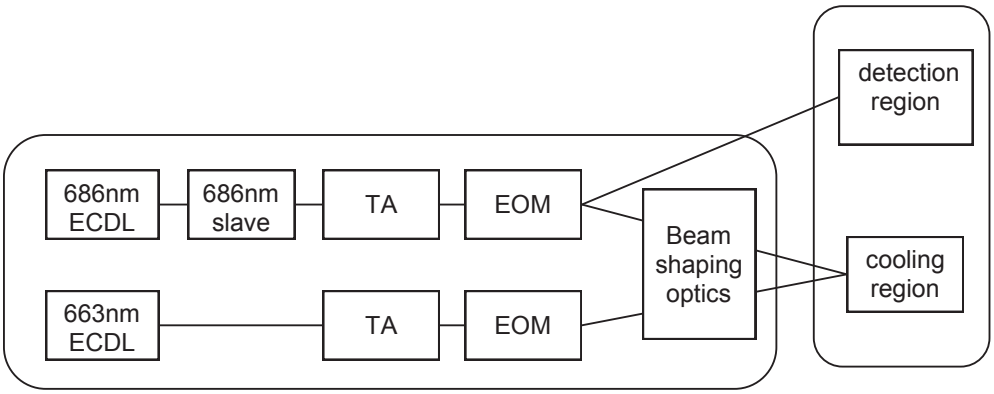

FIGURE 5.15: A flowchart showing the generation of the cooling and repump laser beams that are directed into the cooling region, after improvements were made.

Two mirrors of length 20 cm are used to reflect the cooling and repump beams in a zig-zag path that intersects the molecular beam 25 times. The two mirrors are parallel, with one mirror shifted upwards, so that the laser beam can enter the chamber from below the first mirror through the first window, at a slight angle to the normal of the mirrors. Then the beam emerges from the second window and is reflected by the second mirror, and so on. The cooling and repump beams measure 20 mm (in the transverse direction) by 8 mm (in the longitudinal direction) when they enter the vacuum chamber. Unlike the previous setup, the mirrors are mounted outside the chamber. Therefore the cooling and repump beams pass through two windows, every time they intersect the molecular beam. The transmission through the windows for the cooling and repump beams are 99% and 98.5% per pass respectively.

The tapered amplifier is a Toptica BoosTA with centre wavelength 690 nm. As shown in the flowchart in figure 5.15, this tapered amplifier is placed after the injection-locked slave laser. In addition, we moved the EOM from before the slave laser to after the tapered amplifier. This is because the injection locked slave laser is more stable when the seed laser is not modulated. We had chosen to seed with a modulated laser previously in order to avoid the power from the output of the slave laser being lost in the EOM, which has a transmission of around 90%.

With the tapered amplifier, the repump beam diameter is 0.5 mm after the EOM, which is the same size as the cooling beam, with a similar power to the cooling beam ($\sim$250 mW). Therefore, both the cooling and repump beams can be combined after

they pass through their respective EOMs, then they are shaped together, before they are sent to the new vacuum chamber segment.

5.10.1 Numerical Simulation for the New Setup

In the same way as for the previous experimental setup, we run the numerical model in section 5.5, with the new experimental parameters in order to plot some expected results for the 1D transverse cooling experiment with the new setup.

In this model, in addition to the assumptions we have described in section 5.5, we make an approximation to account for the loss of power in the cooling and repump laser beams as they pass through the windows on the chamber many times. We simply assume that the intensity of the cooling and repump beams is constant throughout the interaction region, and is equal to the intensity of the cooling beam, halfway up the interaction region. This value of intensity that we use is $82\,\mathrm{mW\,cm^{-2}}$. From section 5.10, we know that the effective saturation intensity $I_{\mathrm{sat,eff}}$ is 6 times the saturation intensity of a single transition I_{sat}=$2.97\,\mathrm{mW\,cm^{-2}}$. Recalling that each beam consists of four hyperfine components, $I_{\mathrm{sat,eff}} = 6 \times 4 \times 2.97\,\mathrm{mW\,cm^{-2}} = 70.8\,\mathrm{mW\,cm^{-2}}$. Therefore we run the simulation with the intensity as I=$1.16\,I_{\mathrm{sat,eff}}$. The results are shown in 5.17

Previously, the difference between the maximum and minimum enhancement signal that could be obtained was 0.44 in the numerical modelling results, and was measured to be 0.24. Now, the difference between the maximum and minimum enhancement signal given by the numerical model is 0.7.

Data recording using the new setup is currently underway.

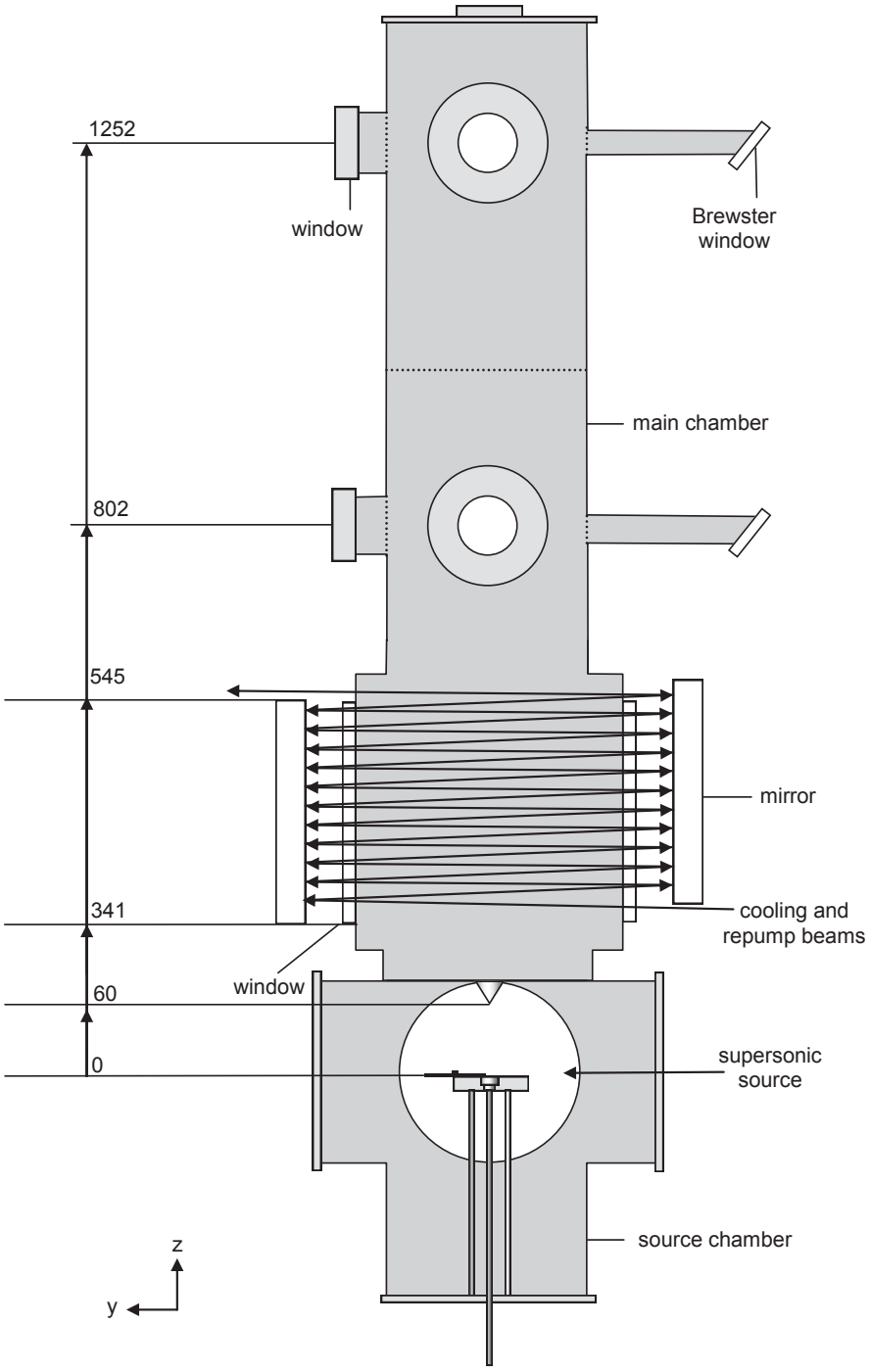

FIGURE 5.16: A schematic diagram of the vacuum chamber after the chamber segment of the interaction region (maximum 6 cm interaction length) has been replaced with a longer segment (maximum 20 cm interaction length).

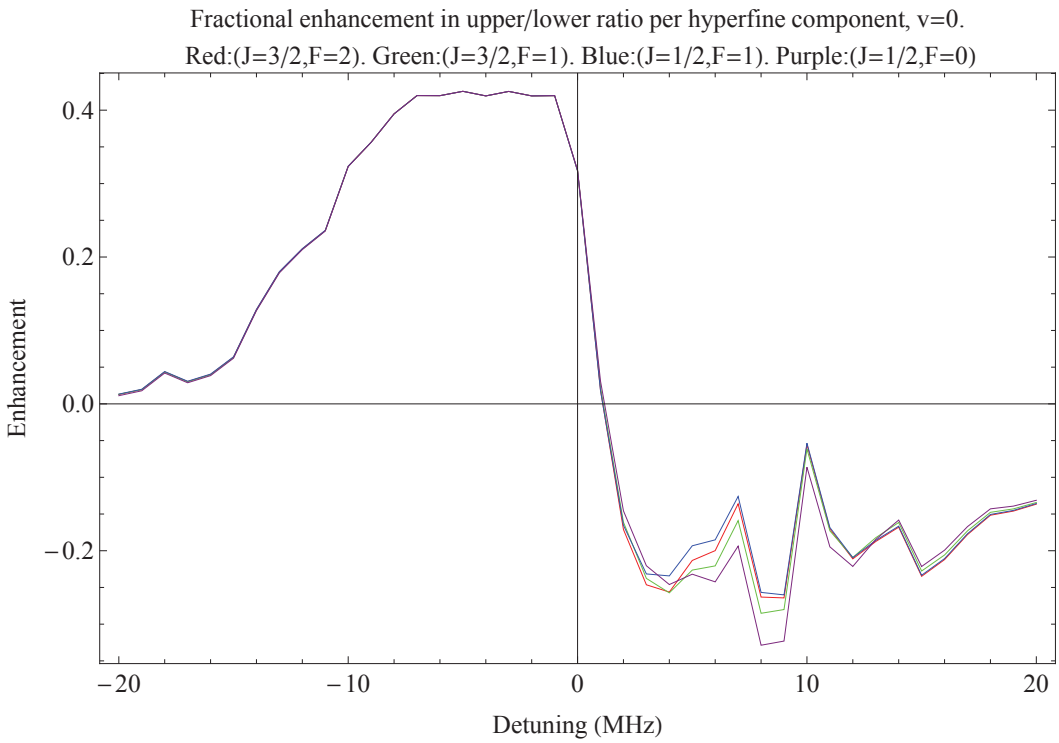

FIGURE 5.17: The enhancement signal for various values of detuning, as calculated by the numerical model for the improved experimental setup.

Chapter 6

Conclusions and Outlook

6.1 The Current Status of Laser Cooled Molecules

Here, I describe the work in the field of laser cooling molecules that has already been done and emphasize what our experiment adds to this body of knowledge.

Cycling fluorescence and radiative pressure on molecules was first reported in 2009 in SrF [51]. This is an experiment consisting of a buffer gas SrF molecular beam source, a pump region, and a probe region. The buffer gas source generates a $\sim$4 K beam of SrF with mean longitudinal velocity 200 m/s and maximum transverse velocity 3 m/s. This experiment uses the same cooling and repump transitions as in our experiment. In the pump region, a $X(v'' = 0)$ to $A(v' = 0)$ pump beam and $X(v'' = 1)$ to $A(v' = 0)$ repump beam intersects the molecular beam in one transverse direction for an interaction time of 44 μs. The intensity of the cooling beam is 1300 mW/cm^2 and the intensity of the repump beam is 1600 mW/cm^2. Both of these beams have sidebands to address all hyperfine levels. There are also a pair of Helmholtz coils around the pump region. These generate a B-field of magnitude 7 G at 30° relative to the laser polarization.

To measure the cycling fluorescence, the pump region was probed using a PMT. Without the B-field or the repump beam, each molecule scatters 3.5 photons per transition before entering a dark state. With the addition of the 7 G B-field, the laser-induced fluorescence from the pumping transition increased by a factor of 3.5. Finally, with the addition of the repump beam, the laser-induced fluorescence was further increased by a factor of 3.5. This corresponds to a total of 170 scattered photons.

The resulting deflection of the molecular beam by radiative pressure was observed by imaging the laser-induced fluorescence from the $X(N'' = 1) \rightarrow A(J' = 1/2)$ using a CCD camera in the probe region. The centre of the beam had shifted by 0.5 mm in the direction of the cooling and repump beams at the probe region, which is 12.5 cm away from the pump region. This corresponds to 140 photons scattered per molecule.

In 2010, the same group reported the transverse laser cooling of SrF [59]. In this experiment, both Sisyphus and Doppler cooling were observed. This experiment was based on the same set-up as the experiment to observe cycling fluorescence and radiative pressure using a buffer gas source. To conduct the laser cooling experiment, a second repump laser addressing the $X(v'' = 2)$ to $A(v' = 1)$ transition was added to pump out the population which leaks into the $X(v = 2)$ level. The cooling beam and two repump beams are combined and reflected back and forth many times at a slight angle such that they intersect the molecular beam ~ 75 times in the cooling region. The cooling region was lengthened to 15 cm since the previous deflection experiment. At the end of the cooling region, the cooling and repump beams are nearly retroreflected to form standing waves. There is still a tunable magnetic field throughout the cooling region. The B-field direction is at angle that is not equal to 0° or 90° relative to the laser polarization direction.

Conducting the experiment at two B-field magnitudes give two distinct sets of results. At a low B-field of 0.6 G cooling is observed when the cooling laser is blue detuned by $1.5\,\Gamma$ and heating is observed when the cooling laser is red detuned by the same amount. At a high B-field of 5 G, the opposite effect takes place; cooling is observed when the cooling laser is red detuned by $1.5\,\Gamma$ and heating is observed when the cooling laser is blue detuned by the same amount. The effects that are seen at the high and the low B-fields are consistent with the expected effects due to Doppler forces and Sisyphus forces respectively.

The unperturbed beam has a transverse temperature of 50 mK and this is reduced to a minimum of 5 mK in the regime where Doppler forces dominate, and a minimum of 300 mK when Sisyphus forces dominate. This is consistent with 500 to 1,000 photons scattered per molecule.

In 2012, the same group demonstrated longitudinal deceleration of an SrF beam [60]. In this experiment, the forward velocity of the beam from is reduced from 175 m/s by 40 to 60 m/s using one cooling laser and two repump lasers (as in the transverse cooling experiment). This corresponds to a mean number of photons scattered per molecule of 10^4. However, this experiment suffers loss of molecules,

which is attributed to transverse heating and divergence of the molecular beam. Since then, longitudinal slowing in CaF [61] has also been demonstrated.

In 2013, the 2D magneto-optical trapping of YO was reported [62]. Like SrF, YO has a level structure that is amenable to laser cooling with high relevant Franck-Condon factors (vibrational branching to $v > 2$ levels is $< 10^{-6}$), a short upper state lifetime (33 ns) and a significant permanent dipole moment (4.52 D [63]). In this experiment, YO molecules are cooled on the $X^2\Sigma^+ \rightarrow A\Pi_{1/2}$ transition. One cooling laser addresses the $X(v'' = 0) \rightarrow A(v' = 0)$ transition and two repump lasers address the $X(v'' = 1) \rightarrow A(v' = 1)$ and $X(v'' = 2) \rightarrow A(v' = 1)$ transitions respectively. Each laser is frequency modulated using acousto-optic modulators to address the rotational and hypefine levels.

A MOT consists of a red-detuned optical molasses with a spatially varying magnetic field. The magnetic field causes a Zeeman shift each molecule, with a shift size that depends on the position of the molecule. The gradient of the magnetic field is such that molecules that move away from the centre of the trap come into resonance with the red-detuned optical molasses beam preferentially receives momentum kicks towards the centre of the beam, and experiences a restoring force. The challenge faced in the realization of a molecular MOT is the presence of dark states as described in section 2.4. In all of the laser cooling experiments described so far, the dark states were destablized using a magnetic field. However, this is not an option in the case of a MOT. An alternative way of destabilizing the dark state is by modulating the optical polarization of the cooling light between σ^+ and σ^- using a voltage-controlled wave plate. This is what is done in the YO experiment. However, switching the polarization of the cooling light also switches the direction of the restoring force. To overcome this, the direction of the B-field is modulated in phase with the cooling light polarization to mainting the restoring force of the MOT. As a result, the temperature of the YO molecules is cooled from 25 mK to 10 mK with just the cooling light, then to a minimum of 2 mK with the addition of the magnetic field to form the MOT.

This experimental project commenced in Summer 2010. Since then, we have built a new experiment consisting of a supersonic SrF source, a cooling and repump system, and a new detection system that has two points of detection. We have performed the spectroscopy of relevant SrF transitions, demonstrated cycling and achieved beam brightening by 1D transverse cooling. The main difference between our experiment and that of [59] is that the cooling force comes just from Doppler forces, and not Sisyphus forces. The cooling beam is not retroreflected, so there are

no standing waves, and there are no Sisyphus cooling effects the compete with the Doppler cooling effects. We model this simpler system in a 28-level model, so that we can understand the cooling behaviour quantitatively, and find good agreement with experimental data. By constructing theoretical models and testing them using experimental data step by step, we hope to gain a better understanding of the laser cooling process in molecules so that they can be used reliably in future applications.

6.2 The Future of Laser Cooling Molecules

The many potential applications of laser cooling are described in section 1.1. The application of particular interest to us here at the Centre for Cold Matter is in a fountain of YbF molecules to measure the electron's electric dipole moment [56]. Laser cooling of molecules is a key technique that should enable the current best measurement of the electron's electric dipole moment to be bettered by up to three orders of magnitude. As described in section 1.1.2, the current YbF electron electric dipole moment experiment in our research group [8] is a molecular beam experiment with a supersonic source. In the new experiment, the molecules will be pre-cooled in a helium buffer gas source, steered away from the buffer gas by magnetic guiding [64], stopped and cooled in an optical molasses, and launched as a fountain between two electric field plates before being detected. The electron spin of the molecules are polarized at the beginning of the fountain, then they precess while moving through the electric field, and are detected to measure the amount of precession, from which the electron edm is deduced.

The most recent electron electric dipole moment measurement gave an upper limit of $|d_e| \leq 1.05 \times 10^{-27} \mathrm{e\,cm}$. The fundamental improvement of replacing the molecular beam with a molecular fountain increases the coherence time of the precessing molecules from the present 1 ms to 1 s. This will enable measurements of the electron electric dipole moment down to $1 \times 10^{-30}\,\mathrm{e\,cm}$. This enables us to explore new areas of elementary particle physics that shed light on the origin of CP-violation in the early universe.

Our experiment is an excellent starting point to understand the technique of molecular laser cooling, which will aid the development of many applications including the YbF fountain. There are many ways in which our experiment can be developed in the shorter term towards realizing more sophisticated laser cooling techniques.

In the short-term, further 1D cooling experiments will be conducted using the new improved setup as described in section 5.10 to yield more pronounced cooling effects. In addition to the investigation of Doppler cooling, we can set up standing waves by retroreflecting the cooling beam to investigate Sisyphus cooling effects. Furthermore, we expect to cool the molecules to the Doppler temperature or lower by replacing the supersonic source with a cryogenic source and adding a repump from the second excited vibrational level in the first excited electronic level. The transverse cooling can easily be extended from 1D to 2D cooling. Slowing and cooling in 3D can be achieved with the addition of a chirped longitudinal cooling beam. We have performed some preliminary tests which show that ECDL frequencies can be chirped easily by chirping the voltage of the piezoelectric transducer that changes the angle of the grating. The molecules can then be captured in a 3D optical molasses, magneto-optical trap (MOT) or microwave trap [65].

Bibliography

[1] Lincoln D Carr, David DeMille, Roman V Krems, and Jun Ye. Cold and ultracold molecules: science, technology and applications. *New Journal of Physics*, 11(5):055049, 2009. URL http://stacks.iop.org/1367-2630/11/i=5/a=055049.

[2] D. DeMille. Quantum computation with trapped polar molecules. *Phys. Rev. Lett.*, 88(6):067901, Jan 2002. doi: 10.1103/PhysRevLett.88.067901.

[3] Michael A. Nielsen and Isaac L. Chuang. *Quantum Computation and Quantum Information*. Cambridge University Press, 2000.

[4] M. V. Romalis and E. N. Fortson. Zeeman frequency shifts in an optical dipole trap used to search for an electric-dipole moment. *Phys. Rev. A*, 59: 4547–4558, Jun 1999. doi: 10.1103/PhysRevA.59.4547. URL http://link.aps.org/doi/10.1103/PhysRevA.59.4547.

[5] J. J. Hudson, B. E. Sauer, M. R. Tarbutt, and E. A. Hinds. Measurement of the electron electric dipole moment using ybf molecules. *Phys. Rev. Lett.*, 89: 023003, Jun 2002. doi: 10.1103/PhysRevLett.89.023003. URL http://link.aps.org/doi/10.1103/PhysRevLett.89.023003.

[6] MR Tarbutt, JJ Hudson, BE Sauer, and EA Hinds. Prospects for measuring the electric dipole moment of the electron using electrically trapped polar molecules. *Faraday discussions*, 142:37–56, 2009.

[7] BC Regan, Eugene D Commins, Christian J Schmidt, and David DeMille. New limit on the electron electric dipole moment. *Physical review letters*, 88 (7):071805, 2002.

[8] JJ Hudson, DM Kara, IJ Smallman, BE Sauer, MR Tarbutt, and EA Hinds. Improved measurement of the shape of the electron. *Nature*, 473(7348):493–496, 2011.

[9] Ian Joseph Smallman. *A New Measurement of the Electron Electric Dipole Moment Using Ytterbium Fluoride*. PhD thesis, Imperial College London, 2013.

[10] A C Vutha, W C Campbell, Y V Gurevich, N R Hutzler, M Parsons, D Patterson, E Petrik, B Spaun, J M Doyle, G Gabrielse, and D DeMille. Search for the electric dipole moment of the electron with thorium monoxide. *Journal of Physics B: Atomic, Molecular and Optical Physics*, 43(7):074007, 2010. URL http://stacks.iop.org/0953-4075/43/i=7/a=074007.

[11] S. Eckel, P. Hamilton, E. Kirilov, H. W. Smith, and D. DeMille. Search for the electron electric dipole moment using ω -doublet levels in pbo. *Phys. Rev. A*, 87:052130, May 2013. doi: 10.1103/PhysRevA.87.052130. URL http://link.aps.org/doi/10.1103/PhysRevA.87.052130.

[12] Huanqian Loh, Kevin Cossel, Kang-Kuen Ni, Matt Grau, Daniel Gresh, Jun Ye, and Eric Cornell. Towards an electron electric dipole moment search with trapped hff+ molecular ions. *Bulletin of the American Physical Society*, 58, 2013.

[13] Jeongwon Lee, ER Meyer, R Paudel, JL Bohn, and AE Leanhardt. An electron electric dipole moment search in the x $3\delta 1$ ground state of tungsten carbide molecules. *Journal of Modern Optics*, 56(18-19):2005–2012, 2009.

[14] Sebastiaan Y. T. van de Meerakker, Nicolas Vanhaecke, Mark P. J. van der Loo, Gerrit C. Groenenboom, and Gerard Meijer. Direct measurement of the radiative lifetime of vibrationally excited oh radicals. *Phys. Rev. Lett.*, 95(1): 013003, Jul 2005. doi: 10.1103/PhysRevLett.95.013003.

[15] Eric R. Hudson, H. J. Lewandowski, Brian C. Sawyer, and Jun Ye. Cold molecule spectroscopy for constraining the evolution of the fine structure constant. *Phys. Rev. Lett.*, 96:143004, Apr 2006. doi: 10.1103/PhysRevLett.96.143004. URL http://link.aps.org/doi/10.1103/PhysRevLett.96.143004.

[16] Roman V Krems. Cold controlled chemistry. *Physical Chemistry Chemical Physics*, 10(28):4079–4092, 2008.

[17] Eugene P. Wigner. On the behavior of cross sections near thresholds. *Phys. Rev.*, 73(9):1002–1009, May 1948. doi: 10.1103/PhysRev.73.1002.

[18] R. V. Krems. Molecules near absolute zero and external field control of atomic and molecular dynamics. *International Reviews in Physical Chemistry*, 24:99–118, 2005. doi: 10.1080/01442350500167161.

[19] R. V. Krems. Breaking van der waals molecules with magnetic fields. *Phys. Rev. Lett.*, 93(1):013201, Jun 2004. doi: 10.1103/PhysRevLett.93.013201.

[20] A Micheli, G K Brennen, and P Zoller. A toolbox for lattice-spin models with polar molecules. *Nature*, 2:341, 2006.

[21] K. Góral, L. Santos, and M. Lewenstein. Quantum phases of dipolar bosons in optical lattices. *Phys. Rev. Lett.*, 88:170406, Apr 2002. doi: 10.1103/PhysRevLett.88.170406. URL http://link.aps.org/doi/10.1103/PhysRevLett.88.170406.

[22] AF Andreev and IM Lifshits. Quantum theory of defects in crystals. *ZHUR EKSPER TEORET FIZIKI*, 56(6):2057–2068, 1969.

[23] L. Santos, G. V. Shlyapnikov, P. Zoller, and M. Lewenstein. Bose-einstein condensation in trapped dipolar gases. *Phys. Rev. Lett.*, 85(9):1791–1794, Aug 2000. doi: 10.1103/PhysRevLett.85.1791.

[24] M.A. Baranov. Theoretical progress in many-body physics with ultracold dipolar gases. *Physics Reports*, 464(3):71 – 111, 2008. ISSN 0370-1573. doi: DOI:10.1016/j.physrep.2008.04.007. URL http://www.sciencedirect.com/science/article/B6TVP-4SF8SX8-1/2/83f9ad48fada18da582ffec7cf12aa41.

[25] Bretislav Friedrich and John M. Doyle. Why are cold molecules so hot? 2009. URL http://edoc.mpg.de/377541.

[26] K.-K. Ni, S. Ospelkaus, M. H. G. de Miranda, A. Pe'er, B. Neyenhuis, J. J. Zirbel, S. Kotochigova, P. S. Julienne, D. S. Jin, and J. Ye. A high phase-space-density gas of polar molecules. *Science*, 322(5899):231–235, 2008. doi: 10.1126/science.1163861. URL http://www.sciencemag.org/content/322/5899/231.abstract.

[27] Johann G Danzl, Manfred J Mark, Elmar Haller, Mattias Gustavsson, Russell Hart, Jesus Aldegunde, Jeremy M Hutson, and Hanns-Christoph Nägerl. An ultracold high-density sample of rovibronic ground-state molecules in an optical lattice. *Nature Physics*, 6(4):265–270, 2010.

[28] Jeremy M. Sage, Sunil Sainis, Thomas Bergeman, and David DeMille. Optical production of ultracold polar molecules. *Phys. Rev. Lett.*, 94:203001, May 2005. doi: 10.1103/PhysRevLett.94.203001. URL http://link.aps.org/doi/10.1103/PhysRevLett.94.203001.

[29] Kevin M. Jones, Eite Tiesinga, Paul D. Lett, and Paul S. Julienne. Ultracold photoassociation spectroscopy: Long-range molecules and atomic scattering. *Rev. Mod. Phys.*, 78(2):483–535, May 2006. doi: 10.1103/RevModPhys.78.483.

[30] R. Wynar, R. S. Freeland, D. J. Han, C. Ryu, and D. J. Heinzen. Molecules in a Bose-Einstein Condensate. *Science*, 287:1016–1019, February 2000. doi: 10.1126/science.287.5455.1016.

[31] Christiane P. Koch, Eliane Luc-Koenig, and Fran çoise Masnou-Seeuws. Making ultracold molecules in a two-color pump-dump photoassociation scheme using chirped pulses. *Phys. Rev. A*, 73(3):033408, Mar 2006. doi: 10.1103/PhysRevA.73.033408.

[32] Matthieu Viteau, Amodsen Chotia, Maria Allegrini, Nadia Bouloufa, Olivier Dulieu, Daniel Comparat, and Pierre Pillet. Optical pumping and vibrational cooling of molecules. *Science*, 321(5886):232–234, 2008.

[33] Jacqueline van Veldhoven, Hendrick L. Bethlem, and Gerard Meijer. ac electric trap for ground-state molecules. *Phys. Rev. Lett.*, 94:083001, Mar 2005. doi: 10.1103/PhysRevLett.94.083001. URL http://link.aps.org/doi/10.1103/PhysRevLett.94.083001.

[34] Edvardas Narevicius, Adam Libson, Christian G. Parthey, Isaac Chavez, Julia Narevicius, Uzi Even, and Mark G. Raizen. Stopping supersonic oxygen with a series of pulsed electromagnetic coils: A molecular coilgun. *Phys. Rev. A*, 77(5):051401, May 2008. doi: 10.1103/PhysRevA.77.051401.

[35] Sebastiaan Y. T. van de Meerakker, Paul H. M. Smeets, Nicolas Vanhaecke, Rienk T. Jongma, and Gerard Meijer. Deceleration and electrostatic trapping of oh radicals. *Phys. Rev. Lett.*, 94(2):023004, Jan 2005. doi: 10.1103/PhysRevLett.94.023004.

[36] Floris M.H. Crompvoets, Hendrick L. Bethlem, and Gerard Meijer. A storage ring for neutral molecules. 52:209 – 287, 2005. ISSN 1049-250X. doi: DOI:10.1016/S1049-250X(05)52005-6. URL http://www.sciencedirect.com/science/article/B8JD4-4PTXWTY-7/2/1a1b31d567bbcff90bb5a7f422c34db7.

[37] Hendrick L. Bethlem, Jacqueline van Veldhoven, Melanie Schnell, and Gerard Meijer. Trapping polar molecules in an ac trap. *Phys. Rev. A*, 74(6):063403, Dec 2006. doi: 10.1103/PhysRevA.74.063403.

[38] Jonathan D Weinstein et al. Magnetic trapping of calcium monohydride molecules at millikelvin temperatures. *Nature*, 395(6698):148–150, 1998.

[39] R. deCarvalho, J.M. Doyle, B. Friedrich, T. Guillet, J. Kim, D. Patterson, and J.D. Weinstein. Buffer-gas loaded magnetic traps for atoms and molecules: A primer. *The European Physical Journal D - Atomic, Molecular, Optical and Plasma Physics*, 7:289–309, 1999. ISSN 1434-6060. URL http://dx.doi.org/10.1007/s100530050572. 10.1007/s100530050572.

[40] S. E. Maxwell, N. Brahms, R. deCarvalho, D. R. Glenn, J. S. Helton, S. V. Nguyen, D. Patterson, J. Petricka, D. DeMille, and J. M. Doyle. High-flux beam source for cold, slow atoms or molecules. *Phys. Rev. Lett.*, 95(17):173201, Oct 2005. doi: 10.1103/PhysRevLett.95.173201.

[41] Benjamin K Stuhl, Matthew T Hummon, Mark Yeo, Goulven Quéméner, John L Bohn, and Jun Ye. Evaporative cooling of the dipolar hydroxyl radical. *Nature*, 492(7429):396–400, 2012.

[42] L. P. Parazzoli, N. J. Fitch, P. S. Żuchowski, J. M. Hutson, and H. J. Lewandowski. Large effects of electric fields on atom-molecule collisions at millikelvin temperatures. *Phys. Rev. Lett.*, 106:193201, May 2011. doi: 10.1103/PhysRevLett.106.193201. URL http://link.aps.org/doi/10.1103/PhysRevLett.106.193201.

[43] SK Tokunaga, Wojciech Skomorowski, Piotr S Żuchowski, Robert Moszynski, Jeremy M Hutson, EA Hinds, and MR Tarbutt. Prospects for sympathetic cooling of molecules in electrostatic, ac and microwave traps. *The European Physical Journal D*, 65(1-2):141–149, 2011.

[44] G. Herzberg. *Spectra of diatomic molecules*. Molecular spectra and molecular structure. Van Nostrand, 1950. ISBN 9780442033859. URL http://books.google.co.uk/books?id=__8uAQAAIAAJ.

[45] Max Born and Robert Oppenheimer. Zur quantentheorie der molekeln. *Annalen der Physik*, 389(20):457–484, 1927.

[46] Howard W. Cruse Paul J. Dagdigian and Richard N. Zare. Radiative lifetimes of the alkaline earth monohalides. *J. Chem. Phys.*, 60(6):2330, 1974.

[47] Timothy C. Steimle, Peter J. Domaille, and David O. Harris. Rotational analysis of the system of SrF using a cw tunable dye laser. *Journal of Molecular Spectroscopy*, 68(1):134–145, October 1977. ISSN 00222852. doi: 10.1016/0022-2852(77)90429-5. URL http://dx.doi.org/10.1016/0022-2852(77)90429-5.

[48] M. D. Di Rosa. Laser-cooling molecules. *The European Physical Journal D - Atomic, Molecular, Optical and Plasma Physics*, 31(2):395–402, November . ISSN 1434-6060. doi: 10.1140/epjd/e2004-00167-2. URL http://dx.doi.org/10.1140/epjd/e2004-00167-2.

[49] Ch. Ryzlewicz, H.-U. Schtze-Pahlmann, J. Hoeft, and T. Trring. Rotational spectrum and hyperfine structure of the 2 radicals baf and bacl. *Chemical Physics*, 71(3):389 – 399, 1982. ISSN 0301-0104. doi: 10.1016/0301-0104(82)85045-3. URL http://www.sciencedirect.com/science/article/pii/0301010482850453.

[50] W.J. Childs, L.S. Goodman, and I. Renhorn. Radio-frequency optical double-resonance spectrum of srf: The x2+ state. *Journal of Molecular Spectroscopy*, 87(2):522 – 533, 1981. ISSN 0022-2852. doi: 10.1016/0022-2852(81)90422-7. URL http://www.sciencedirect.com/science/article/pii/0022285281904227.

[51] ES Shuman, JF Barry, DR Glenn, and D DeMille. Radiative force from optical cycling on a diatomic molecule. *Physical review letters*, 103(22):223001, 2009.

[52] D. J. Berkeland and M. G. Boshier. Destabilization of dark states and optical spectroscopy in zeeman-degenerate atomic systems. *Phys. Rev. A*, 65(3):033413, Feb 2002. doi: 10.1103/PhysRevA.65.033413.

[53] M R Tarbutt, J J Hudson, B E Sauer, E A Hinds, V A Ryzhov, V L Ryabov, and V F Ezhov. A jet beam source of cold ybf radicals. *Journal of Physics B: Atomic, Molecular and Optical Physics*, 35(24):5013, 2002. URL http://stacks.iop.org/0953-4075/35/i=24/a=306.

[54] A. S. Arnold, J. S. Wilson, and M. G. Boshier. A simple extended-cavity diode laser. *Review of Scientific Instruments*, 69:1236–1239, March 1998. doi: 10.1063/1.1148756.

[55] HL Stover and WH Steier. Locking of laser oscillators by light injection. *applied physics letters*, 8(4):91–93, 1966.

[56] MR Tarbutt, BE Sauer, JJ Hudson, and EA Hinds. Design for a fountain of ybf molecules to measure the electron's electric dipole moment. *New Journal of Physics*, 15(5):053034, 2013.

[57] J. F. Barry, E. S. Shuman, E. B. Norrgard, and D. DeMille. Laser radiation pressure slowing of a molecular beam. *Phys. Rev. Lett.*, 108:103002, Mar 2012. doi: 10.1103/PhysRevLett.108.103002. URL http://link.aps.org/doi/10.1103/PhysRevLett.108.103002.

[58] Claude Cohen-Tannoudji, Jacques Dupont-Roc, Gilbert Grynberg, and Pierre Meystre. Atom-photon interactions: Basic processes and applications. *Physics Today*, 45:115, 1992.

[59] ES Shuman, JF Barry, and D DeMille. Laser cooling of a diatomic molecule. *Nature*, 467(7317):820–823, 2010.

[60] JF Barry, ES Shuman, EB Norrgard, and D DeMille. Laser radiation pressure slowing of a molecular beam. *Physical Review Letters*, 108(10):103002, 2012.

[61] V Zhelyazkova, A Cournol, TE Wall, A Matsushima, JJ Hudson, EA Hinds, MR Tarbutt, and BE Sauer. Laser cooling and slowing of caf molecules. *arXiv preprint arXiv:1308.0421*, 2013.

[62] Matthew T Hummon, Mark Yeo, Benjamin K Stuhl, Alejandra L Collopy, Yong Xia, and Jun Ye. 2d magneto-optical trapping of diatomic molecules. *Physical Review Letters*, 110(14):143001, 2013.

[63] RD Suenram, FJ Lovas, GT Fraser, and K Matsumura. Pulsed-nozzle fourier-transform microwave spectroscopy of laser-vaporized metal oxides: Rotational spectra and electric dipole moments of yo, lao, zro, and hfo. *The Journal of Chemical Physics*, 92:4724, 1990.

[64] David Patterson and John M Doyle. Bright, guided molecular beam with hydrodynamic enhancement. *The Journal of chemical physics*, 126:154307, 2007.

[65] D DeMille, DR Glenn, and J Petricka. Microwave traps for cold polar molecules. *The European Physical Journal D-Atomic, Molecular, Optical and Plasma Physics*, 31(2):375–384, 2004.